École polytechnique de Louvain

Evaluation of the Elastic Properties of Thin Films by Finite Element Method

Author: **Martin LACROIX**
Supervisor: **Stéphane LUCAS**
Readers: **Jérôme MÜLLER, Philippe LAMBIN, Thomas PARDOEN**
Academic year 2020–2021
Specialised master in nanotechnologies

Abstract

This work addresses the implementation of a 3D finite element model (FEM) allowing the evaluation of the elastic properties of metallic thin films deposited on a substrate by magnetron sputtering. In particular, the Young's modulus and the stress-strain relation in compression of Cu, Zr, amorphous CuZr and multilayered Cu/Zr films are studied. First, the governing equations of elasticity augmented by surface stress and surface stiffness theories are recalled in their analytical form, then the corresponding finite element formulation is derived. The transport of sputtered particles through the gas phase flux during sputtering is performed with the binary collision Monte Carlo program SIMTRA. The simulation of deposition, diffusion, nucleation and growth of the films is performed by the kinetic Monte Carlo code NASCAM. Finally, the Young's modulus obtained by the FEM simulation is compared to experimental results from the literature.

Notations

w	A scalar or a function.
$\mathbb{H}$	Fourth-order tensor.
$\mathbf{M}$	Second-order tensor or a matrix.
$\mathbf{v}$	First-order tensor or a column vector.
$\underline{v}$	Voigt notation of a second-order tensor.
$\mathbf{M}_1 : \mathbf{M}_2$	Double dot product of two matrices or tensors.
$\mathbb{H} : \mathbf{M}$	Double dot product of a fourth and second-order tensors.
$\mathbf{v}_1 \cdot \mathbf{v}_2$	Standard dot product of two vectors.
$\mathbf{v}_1 \otimes \mathbf{v}_2$	Tensor product of two vectors.
$\mathbf{v}_1 \times \mathbf{v}_2$	Cross product of two vectors.
$\mathbf{M} \cdot \mathbf{v}$	Dot product of a tensor and a vector.
$\mathbf{M}\mathbf{v}$	Standard matrix-vector product.
$\mathbf{v}_1\mathbf{v}_2$	Standard vector-vector product.
$\nabla\mathbf{v}$	Gradient of a vector field.
$\nabla \cdot \mathbf{M}$	Divergence of a tensor field.
$\mathbf{M}^\top$	Transpose of a tensor or a matrix.
$\mathbf{v}^\top$	Transpose of a column vector.
$\mathrm{sym}(\mathbf{M})$	Projection of $\mathbf{M}$ on the symmetric space.
$\mathcal{A}$	Application or differential operator.

Contents

Chapter 1

Introduction

1.1 Objectives and Outline

The objective of this work is to study the implementation of a fast numerical model allowing the evaluation of the elastic properties of thin films deposited by plasma at low pressure. In particular, the equivalent elastic modulus and the influence of the porosity, internal structure, deposited material and number of layers are of interest. The thin film deposition has been simulated by the 3D kinetic Monte Carlo code NASCAM developed at the University of Namur [1]. Atomistic models such as molecular dynamics are suitable for simulating the elementary processes responsible for mechanical properties of thin films, but are typically complex and very demanding in computer resources. In this work, we propose the use of Galerkin methods, which are based on the weak formulation of the partial differential equations governing the physical phenomenon to be represented. In the so-called finite element method (FEM), this is achieved by a particular spatial discretization in the space dimensions, which is implemented by the construction of a finite element mesh of the domain. The thin films of interest are metal structures composed of a potentially large number of atoms in 3D that may be simulated individually in the structure, or partially by the use of macro-atoms. Those macro-atoms represent a cluster of atoms and are considered as a single particle in NASCAM, allowing for coarser meshes and therefore reduce the computation time of the Monte Carlo algorithm. Finally, it is important to note that this work concerns the elastic properties (Figure 1), meaning that plastic deformations, characterized by an irreversible change in the geometry of the film, as well as the movement of dislocations, are not represented in the numerical model. Plastic deformations occur when the material is subjected to stresses exceeding its yield strength, which can be measured experimentally.

The FEM is a powerful numerical tool that is well adapted at the macro or microscale. This method has the advantage of being versatile in the range of problems it can solve. But, since the FEM needs the definition of a constitutive law and assumes the material to be continuous, it is not directly able to simulate effects associated to attractive and repulsive forces related to energetic interatomic potentials or related to thermal fluctuations, that are fundamental for simulating materials at the nanoscale. Accordingly, the classical FEM cannot be directly employed to simulate a nanoscale problem. However, by employing suitable homogenization approaches, it is possible to define constitutive relationships that include the influence of nanoscale phenomena, meaning that the FEM can be suitably formulated in order to account, at its continuum level, for effects deriving from nanoscale processes such as long-range interactions. These FEM formulations are called multiscale models. A summary of the main steps of our work is presented in Figure 2.

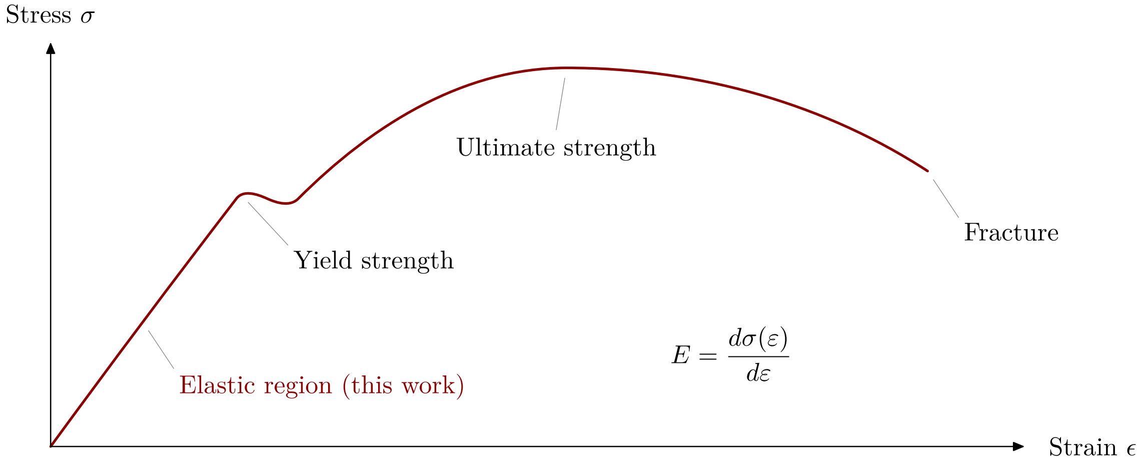

Figure 1: Example of a stress-strain curve $\sigma(\varepsilon)$ for a one dimensional traction test with a ductile material of Young's modulus E. The part of the curve located before the yield strength is the elastic region, where the deformations of the sample are reversible.

- **Outline**

In Chapter 1, a literature review of some FEM formulations and theories accounting for nanoscale phenomenon is presented with their advantage and drawbacks. This summary is not an exhaustive list, but aims at providing a global representation of different approaches that could have been used, in addition to explain our principal motivation for choosing a method in particular.

In Chapter 2, the mathematical description of the linear elasticity (LE) and the SET/SST model based on surface stress and surface tension is obtained by deriving a weak formulation of the constitutive equation (the concept of weak formulation is detailed in Annex 6.1). Important ingredients of the FEM such as the interpolation functions or the boundary conditions are also discussed. Finally, a description of the Saint Venant-Kirchhoff model (SVK) for large deformations is presented.

In Chapter 3, different test cases are simulated in order to validate the FEM algorithm thus implemented. The first test case is the well-known cantilever beam where the ability of the code to represent nonlinear deformations is assessed. The second case consists in the relaxation of a nanoplate under the effect of surface tension. Finally, the third test case is a purely 3D case featuring an axial stress applied to an infinite material containing a spherical cavity, this latter allows highlighting some particularities of isoparametric and voxel-based meshes.

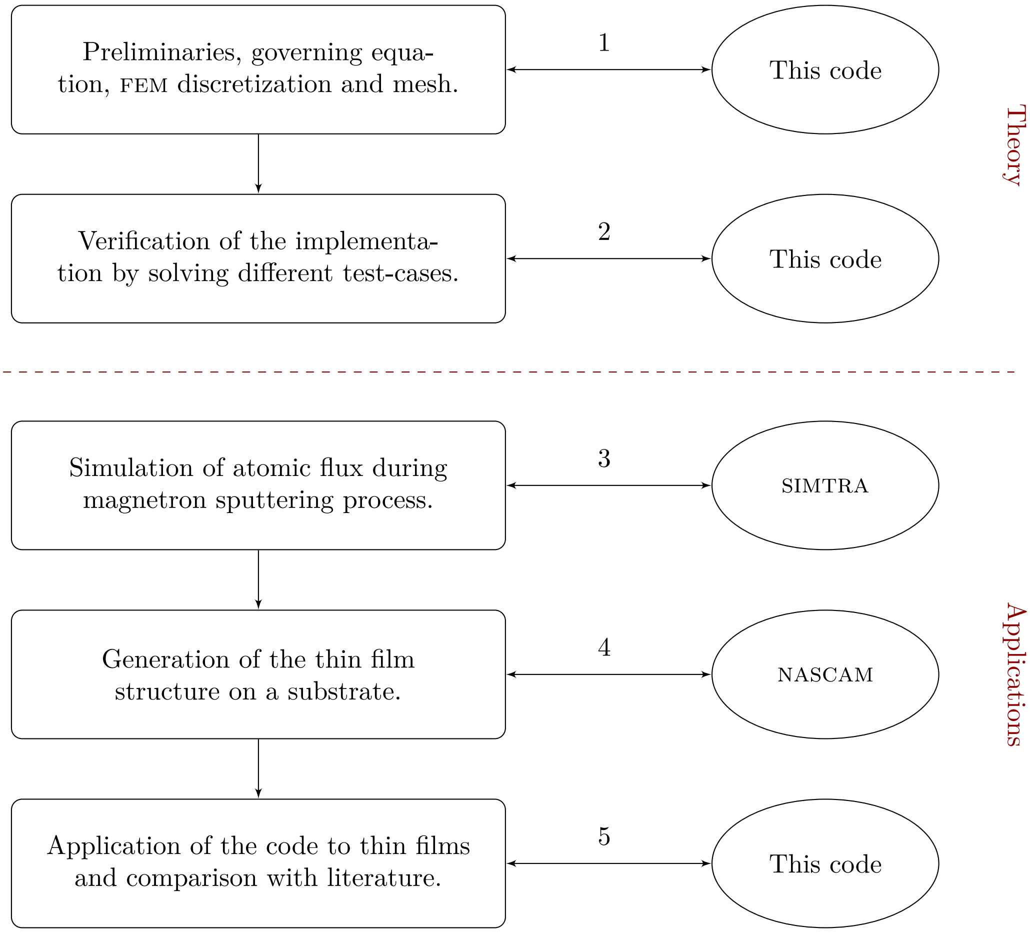

Figure 2: Presentation of the main steps for the realization of this work. The labels on the right feature the numerical tool that has been used at each step. Note that the numbering of those steps is not related to the numbers of the chapters in which they appear.

In Chapter 4, the FEM code is finally applied to thin films. We start with an introduction to the methods employed for generating the sample in NASCAM, in particular, the energy and angular distributions of the deposited particles are of primary interest. The second part of the chapter is dedicated to the comparison of the elastic properties of Cu, Zr and CuZr monolayer thin film. The last part is dedicated to the study of Cu/Zr multilayer thin films deposited either by a single cathode or by a double cathode configuration, by analyzing the influence of the number of layers in their elastic properties.

1.2 Introduction to Thin Films

Thin films are objects whose size are limited at the micro or nanoscale in one direction of space, this dimension is referred as the thickness of the material. Typically, thin films can vary in thickness from a few atomic layers to ten micrometers and modify the properties of the substrate on which they are deposited. The main characteristic of thin films is that their physical and chemical properties can highly differ from those of bulk materials in all their dimensions, and are determined by the thickness, geometry and structure of the sample. Thin films are generally used to improve the surface properties of solids. For instance, they may be used to modify the hardness, transmission, absorption, reflection, abrasion resistance, permeation corrosion and electrical properties of bulk material surfaces. In addition, thin films may be directly used in the fabrication of electrical devices such as batteries [2] or transistors [3]. The manufacture of porous materials in the form of thin films allows having a high surface-to-volume ratio, in order to increase their ability to interact with the medium using small amounts of material, which is of great interest for many applications [4]. For instance, in the development of chemical sensors thanks to surface chemistry, or materials with low dielectric constant to increase signal propagation speed, reduce power consumption, and reduce the crosstalk between adjacent conducting lines [5].

Elastic behavior is a macroscopic evidence of atomic bonding, and a result of atomic bond against extension, compression and distortion. Hence the elastic behavior of the film can be partially explained by its nanostructure. A first intuition about the origin of the difference between macroscale and nanoscale materials can be acquired by considering the surface-to-volume ratio of an object depending on its characteristic size. For instance, a spherical particle depending on its radius:

$$\frac{A}{V} = \frac{3}{4}\frac{4\pi r^2}{\pi r^3} = \frac{3}{r} \tag{1.1}$$

which shows that surface effects such as surface stress increase in importance when the size of the sphere decreases. Physically, the fraction of atoms located at the surface of the object increases as its characteristic dimension of this latter decreases. Moreover, thin film structures are typically made by depositing the material onto a solid substrate and occur at elevated temperatures. As different materials have differing thermal expansion coefficients, potentially large thermal stresses are induced in the film materials and the substrate during manufacture, and remain there while using the devices. Another source of intrinsic stresses is the non-equilibrium growth processes leading to elastic or plastic deformations in the film [6]. During the deposition by magnetron sputtering, the residual stress is associated with the film-substrate lattice misfit, energetic-particle bombardment and deposition conditions such as working pressure and substrate bias. Thereby, the mechanical properties of the film are highly dependent on the substrate and the deposition process, and are of critical importance in the design of electronic systems. For instance, microprocessors must sustain mechanical stresses due to thermal expansion, collision events or friction. In particular, a microstructural feature is to provide resistance to friction and wear [6]. The Stoney equation relates the substrate curvature to film stress, and has been extensively used to estimate the residual stress state in metallic coatings:

$$\sigma = \frac{E}{6(1-\nu)}\left(\frac{t_{\mathrm{S}}}{t_{\mathrm{F}}}\right)^2\left(\frac{1}{R} - \frac{1}{R_0}\right) \tag{1.2}$$

where σ is the residual stress in the film, t_{F} the film thickness, t_{S} the substrate thickness, E the Young's modulus of the substrate and ν is the Poisson's ratio of the substrate. R_0 and R are respectively the radii of curvature of the substrate before and after the film deposition. Due to typically high yield strengths, thin films can support very high residual stresses [7].

1.3 Review of FE Models

In order to represent the elastic properties of thin films, different theories deviating from the classical Euler-Bernoulli theory and Hooke's law have been proposed in the literature to represent the size dependence of the mechanical properties of nanostructures. In this section, we summarize some of those theories that are applicable in the context of the finite element method, and feature their advantages and drawbacks. The considered theories are the surface stress theory, the couple stress theory and the surface elasticity theory. Moreover, the non-local finite element method and the atomistic finite element method are also presented.

- **Atomistic Finite Element**

The atomistic scale finite element method (AFEM) has been proposed in [8][9] in order to study the mechanical properties of nanostructures and is based on the concept of potentials describing the interaction among atoms. The method uses a particular arrangement of overlapping elements to exploit the concept of cutoff radius, typically used in molecular dynamics simulations, to represent the long-range interactions between the atoms. Conversely to the classical FEM, the AFEM is thus a non-local, but also a nonlinear finite-element method. The key idea is to use the atoms as the nodes in the finite element mesh and create overlapping elements which interact with each other by their shared nodes. The governing equation is established by looking for a minimum in the energy of the system. The AFEM has been demonstrated as being a good alternative to molecular dynamics, providing similar results for the test case presented in [8][9]. In the perspective of this work, the thin film material is given as a periodic structure where the exact location of the atoms is not necessarily known. Moreover, the interatomic potential is non-trivial to obtain, or possibly unknown. Finally, the very large number of atoms present in some 3D structures may lead to high computational costs.

- **Non-Local Finite Element**

Similarly to the AFEM, the non-local elasticity theory aims at representing nanostructures by involving the presence of non-local effects as additional body forces acting on material masses and depending on their relative displacements [10]. As shown in Figure 3, the integral model of non-local finite element method (NLFEM) uses the following modified stress tensor

$$\bar{\sigma}(\mathbf{x}) = \int_{\Omega} k\big(\mathbf{x}, \mathbf{y}\big)\sigma(\mathbf{y})\, d\mathbf{y} \tag{1.3}$$

which indicates that the stress component of a body at reference point depends on the strain field on the entire domain. The function k is a positive scalar attenuation function called the kernel and acts as a weight function for the non-local interactions. The NLFEM faces the same problems as AFEM in the sense that it requires an explicit knowledge of the interatomic potential in order to correctly define the kernel function. Moreover, the integral form of the NLFEM induces high computational costs in 3D. Indeed, the local stress must be evaluated for each integration node of a finite element, and at each integration node of the mesh located within a sphere of radius λ around the point on which the nonlocal stress $\bar{\sigma}(\mathbf{x})$ is computed, where λ is the cutoff distance. It is important to note that a Gauss quadrature rule of order p is exact for a polynomial of order $2p - 1$. As the kernel function is not a polynomial, and because its speed of variation in space depends on its characteristic range, the number of quadrature nodes must be adapted to correctly integrate (1.3).

- **Couple Stress Theory**

The couple stress theory (CST) aims at taking into account the local translational motion of a point within a material body in addition to the local rotation of that point by introducing a torque per unit area. The general idea of this micro-elasticity theory is that the points of the continuum associated with a microstructure of finite size can deform both macroscopically and microstructurally, producing the scale effect described by a characteristic size parameter [11][12]. The CST thus introduces three rotational degrees of freedom in the system of equations, which are related to displacement degrees of freedom by Lagrange multipliers.

In a physical context, CST theory can explain that some structures show a stiffening behavior in bending whereas no change is observed in tensile experiments. However, CST is only able to predict a stiffening effect when reducing the characteristic size of the material, and thus cannot be applied to every material. In addition, the length scale parameter cannot be easily computed. Indeed, the only way to estimate this parameter is via fitting to the experimental data [13].

- **Surface Stress and Elasticity**

As presented previously, the surface to volume ratio starts to increase drastically when the characteristic size of the structure decreases, leading to a significant influence of surface effects. This particularity is taken into account by the surface elasticity theory (SET) and the surface stress theory (SST), which are based on the fact that the nature of the chemical bond and the equilibrium interatomic distances on the surface are different from that in the bulk [13][14]. In the SET, the stiffness tensor of a finite element located at the interface is augmented by a surface stiffness tensor taking into account the reduction in the number of bonds. In the SST, residual stresses due to the deposition process or the surface tension of the material are applied to the structure and modify the mechanical response. The advantage of SET is that this latter can explain softening or stiffening behavior, works for all structures irrespectively of length and can sometimes be explained using very simple and intuitive arguments, as for example the oxidation in normal conditions of the surface of the material [13]. The finite element formulation is given under the assumption of quasi-static equilibrium and small strain as follows:

$$\left(\mathbf{K}_{\text{B}} + \mathbf{K}_{\text{S}}\right)\mathbf{u} = \mathbf{F}_{\text{T}} - \mathbf{F}_{\text{S}} \tag{1.4}$$

where $\mathbf{K}_{\text{B}}$ is the conventional stiffness matrix of the bulk and $\mathbf{K}_{\text{S}}$ is the stiffness matrix of the surface, whose intrinsic parameters can be found in the literature. $\mathbf{F}_{\text{T}}$ is the vector of applied stress and $\mathbf{F}_{\text{S}}$ is the residual stress due to surface tension. It is important to note that the gravitational forces are neglected for nanostructures [15]. In the context of porous thin film materials displaying a large surface to volume ratio, and where the porous structure requires a fine mesh, the SET and SST are good candidates for a first finite element analysis. Consequently, the next chapter is dedicated to the mathematical description of the model (1.4) as well as its finite element discretization.

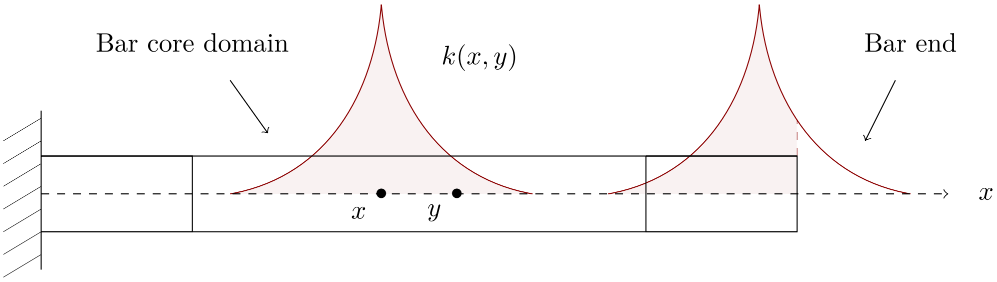

Figure 3: Sketch of the one-dimensional kernel function $k(x,y)$ and of the bar end portions, denoting the average distance beyond which the non-local interaction vanishes. The point x is the point at which the stress is evaluated and y is the variable against which the integral is computed [16].

Chapter 2

Finite Element Models

2.1 Introduction

Continuum mechanics is used to study both the deformation of solids and the flow of fluids. This last point leads to the well-known Navier-Stokes and Stokes equations, which are out of the scope of this work. The case of solids can be expressed from the second Newton's law of motion

$$\begin{cases} \nabla \cdot \sigma + \rho \mathbf{g} = \rho \dfrac{\partial^2 u}{\partial t^2} + \nu \dfrac{\partial u}{\partial t} & \text{in} \;\; \Omega \\ \varepsilon = \dfrac{1}{2}\Big(\nabla u + \nabla u^\top + \nabla u \nabla u^\top\Big) & \text{in} \;\; \Omega \end{cases} \tag{2.1}$$

which is a system of three elliptic partial differential equations for the displacement. The Cauchy stress tensor σ is a function of the strain, $u = [u_1 \; u_2 \; u_3]$ is the three-dimensional displacement field, $\mathbf{g}$ is the gravitational acceleration, ρ is the density of the material, ν is an additional term introducing the viscous damping of mechanical waves and ε is the strain tensor. In this work, the body force $\rho\mathbf{g}$ can be neglected thanks to the small size of the material. It is important to note that in the Eulerian description, the differential operators are defined with respect to the deformed configuration. In the Lagrangian configuration, the differential operators are defined with respect to the initial configuration. Assuming small deformations, one can neglect the nonlinear terms

$$\varepsilon \simeq \frac{1}{2}\Big(\nabla u + \nabla u^\top\Big) \tag{2.2}$$

as the initial and the final configurations of the material are approximately the same. For a structure without damping, the viscous term may be neglected. In the quasi-static approximation, the solution does not depend on the time and the time derivatives may be removed from the equations. As discussed previously, additional terms taking into account the different effects occurring in very small structures due to their discrete nature are required to correctly predict the mechanical response. For instance, the effect of surface elasticity. Finally, it is important to note that purely elastic deformations will be considered, thereby dislocation motion leading to plastic deformations are not taken into account, this assumption must be verified by the use of adequate plastic criteria.

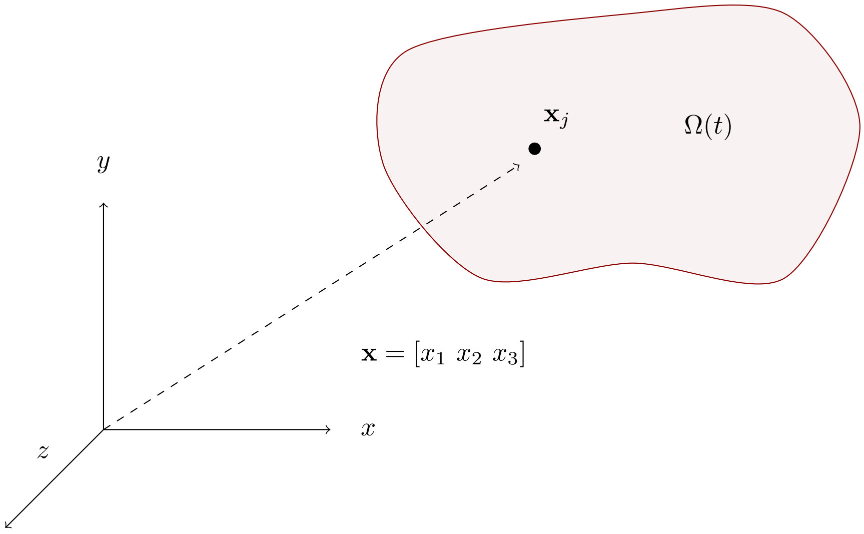

Figure 4: Configuration of a material continuum body of domain $\Omega \in \mathbb{R}^3$ in the Euclidean space at time t. The points within this region are called particles or material points and their position $\mathbf{x}_j$ in Ω is described with the vector of coordinate $\mathbf{x} = [x_1 \; x_2 \; x_3]$ sometime referred as $\mathbf{x} = [x \; y \; z]$ in the report. This continuum body may deform with time.

2.2 Building the Mesh

1

Preliminaries, governing equation, FEM discretization and mesh.

In the finite element method, the domain is first discretized in space by the use of a mesh, hence the quality of the mesh is a critical parameter for the quality of the solution. Practically, the material is discretized into an assembly of finite elements equipped with a number of nodes, two neighbor elements share at least 3 nodes if the elements are tetrahedrons, and 4 if the elements are hexahedrons. In this work, the elementary entities forming the mesh are the so-called 3D Lagrange elements containing $(n+1)^3$ nodes, where n is the order of the element. Each element allows computing elemental matrices that are then assembled into a global matrix $\mathbf{K}$ representing the discretized equation (2.1). If E is the number of elements in the mesh, $\mathbf{K}_e$ and $\mathbf{b}_e$ denote the element matrices and boundary condition vector:

$$\mathbf{K} = \bigoplus_{e=0}^{\mathrm{E}} \mathbf{K}_e \qquad \mathbf{b} = \bigoplus_{e=0}^{\mathrm{E}} \mathbf{b}_e \tag{2.3}$$

Ultimately, the FEM solution is obtained at each node of the mesh by solving a linear system of equations $\mathbf{Ku} = \mathbf{b}$, and interpolated everywhere in the material by shape functions. The Lagrange elements use the Lagrange polynomials [17] for their shape functions. A basis of Lagrange polynomials is defined by its set of data points $\{p_j\}$ and its order n, the j-th polynomial of the set is equal to one at the j-th point of the set and zero on the other points. In three dimensions, the shape function $N_{\mathbf{I}}$ of a node is the product of three Lagrange polynomials in each dimension, where $\mathbf{I}$ is the multi-index. For instance $\mathbf{I} = [I_1\ I_2\ I_3]$ denotes the shape function formed by the product of the I_1-th Lagrange polynomial along the first axis, the I_2-th along the second axis and the I_3-th along the third axis, one has then

$$N_{\mathbf{I}}(\boldsymbol{\xi}) = \prod_{j=1}^{3} L^n_{[I_j]}(\boldsymbol{\xi}_j) \quad \Leftrightarrow \quad L^n_i(\xi) = \prod_{\substack{j=1\\ j\neq i}}^{n+1} \frac{\xi - \xi_j}{\xi_i - \xi_j} \tag{2.4}$$

where L^n_i is the i-th Lagrange polynomial of the set and $\boldsymbol{\xi} = [\xi\ \eta\ \varphi]$ is the local coordinate vector. Indeed, isoparametric finite elements are defined in their own reference frame with $\boldsymbol{\xi} \in [-1, 1]^3$ in three dimensions. Moreover, the derivative of the i-th Lagrange polynomial is given by

$$\frac{dL^n_i}{d\xi}(\xi) = \sum_{\substack{k=1\\ k\neq i}}^{n+1} \left[\frac{1}{\xi_i - \xi_k} \prod_{\substack{j=1\\ j\neq(i,k)}}^{n+1} \frac{\xi - \xi_j}{\xi_i - \xi_j} \right] \tag{2.5}$$

Once the elements of the mesh have been defined, it is necessary to establish the mapping between the global space $[x\ y\ z]$ of Ω and the local space $[\xi\ \eta\ \varphi]$ of each element. For an element of J nodes, the Jacobian matrix of this transformation is computed by

$$\mathbf{J} = \begin{bmatrix} \dfrac{\partial x}{\partial \xi} & \dfrac{\partial y}{\partial \xi} & \dfrac{\partial z}{\partial \xi} \\ \dfrac{\partial x}{\partial \eta} & \dfrac{\partial y}{\partial \eta} & \dfrac{\partial z}{\partial \eta} \\ \dfrac{\partial x}{\partial \varphi} & \dfrac{\partial y}{\partial \varphi} & \dfrac{\partial z}{\partial \varphi} \end{bmatrix} = \sum_{j=1}^{\mathrm{J}} \begin{bmatrix} \dfrac{\partial N_j}{\partial \xi} x_j & \dfrac{\partial N_j}{\partial \xi} y_j & \dfrac{\partial N_j}{\partial \xi} z_j \\ \dfrac{\partial N_j}{\partial \eta} x_j & \dfrac{\partial N_j}{\partial \eta} y_j & \dfrac{\partial N_j}{\partial \eta} z_j \\ \dfrac{\partial N_j}{\partial \varphi} x_j & \dfrac{\partial N_j}{\partial \varphi} y_j & \dfrac{\partial N_j}{\partial \varphi} z_j \end{bmatrix} \tag{2.6}$$

Then, the partial derivatives of the shape functions with respect to the global coordinates in $\mathbf{B}$ are obtained by inverting the previous matrix and applying the chain rule of derivation:

$$\frac{\partial \mathbf{N}}{\partial \mathbf{x}_j} = \frac{\partial \mathbf{N}}{\partial \xi} J^{-1}_{1j} + \frac{\partial \mathbf{N}}{\partial \eta} J^{-1}_{2j} + \frac{\partial \mathbf{N}}{\partial \varphi} J^{-1}_{3j} \tag{2.7}$$

where $\mathbf{x} = [x\ y\ z]$ are the global coordinate variables. Finally, the integrals of the matrices in (2.14) are performed over each element and assembled into the global matrix of the system. A suitable integration method is the Gauss-Legendre quadrature, whose implementation is described in details in [18]. For an integrable function $f : \Omega \to \mathbb{R}^3$ where Ω denotes the domain of an element with respect to the global coordinates, one can perform the integral in the local space $\Sigma = [-1, 1]^3$ as follows:

$$\int_\Omega f(\mathbf{x})\, d\mathbf{x} = \int_\Sigma f\left[\mathbf{x}(\boldsymbol{\xi})\right] \det \mathbf{J}(\boldsymbol{\xi})\, d\boldsymbol{\xi} \tag{2.8}$$

2.3 The SET/SST and LE Models

The SET/SST model is based on the classical linear elastic (LE) model, but where the stress tensor is augmented by a surface stress tensor taking into account surface stiffness and surface tension. Let Ω be the 3D medium composed of different isotropic sub-domains separated by the interfaces Γ_S. The external boundary of the domain is denoted Γ and is decomposed into a first part Γ_U where Dirichlet boundary conditions are imposed and a second part Γ_T where Neumann boundary conditions are imposed. The strong formulation of the SET/SST is obtained by the volume and surface equilibrium equations:

$$\begin{cases} \nabla \cdot \sigma + \rho \mathbf{g} = \rho \dfrac{\partial^2 u}{\partial t^2} & \text{in } \ \Omega \qquad (\textsc{pde}) \\ \nabla_\mathrm{S} \cdot \sigma_\mathrm{S} = \Delta \mathbf{t} & \text{on } \ \Gamma_\mathrm{S} \qquad (\textsc{pde}) \\ \sigma \cdot \mathbf{n} = \mathbf{t} & \text{on } \ \Gamma_\mathrm{T} \qquad (\textsc{bc}) \\ u = \bar{u} & \text{on } \ \Gamma_\mathrm{U} \qquad (\textsc{bc}) \end{cases} \tag{2.9}$$

where $\bar{u}$ is the imposed displacement, ∇_S is the surface gradient, $\mathbf{n}$ is the exterior normal to the boundary, $\mathbf{t}$ are the surface traction and $\Delta\mathbf{t}$ the traction discontinuity at the interface. In the context of linear isotropic elasticity, the stress tensor is a linear function of the strain ε and the surface stress tensor is given by the Shuttleworth equation [19][15] for the surface:

$$\begin{aligned} \sigma &= \frac{\partial U}{\partial \varepsilon} = \mathbb{D} : \varepsilon = \lambda \mathbf{I} \operatorname{tr} \varepsilon + 2\mu\varepsilon \\ \sigma_\mathrm{S} &= \sigma_0 + \frac{\partial \gamma}{\partial \varepsilon_\mathrm{S}} = \tau_0 \mathbf{P} + \mathbb{S} : \varepsilon_\mathrm{S} \end{aligned} \tag{2.10}$$

where $\mathbb{D}$ is the fourth-order bulk stiffness tensor, $\mathbb{S}$ is the fourth-order surface stiffness tensor whose components can be obtained by atomistic simulations [15]. λ is the first Lamé parameter of the bulk, ν is the second Lamé parameters of the bulk, U and γ are the strain energies of the bulk and the surface. The residual surface stress when the material is not strained is σ_0 and τ_0 denotes the surface tension. In infinitesimal strain theory [20], the nonlinear or second-order terms of the finite strain tensor are neglected. Thus we have for the bulk and the surface in small deformation

$$\begin{aligned} \varepsilon &= \frac{1}{2}\left(\nabla u + \nabla u^\top\right) \\ \varepsilon_\mathrm{S} &= \mathbf{P}\varepsilon\mathbf{P}^\top = \mathbf{P}\varepsilon\mathbf{P} \end{aligned} \tag{2.11}$$

where $\mathbf{P}$ is the symmetric surface projection tensor described in Annex 6.1. The components of the bulk and the surface stiffness tensors are given as in [19][21]. Where δ is the Kronecker delta, $(\lambda, \lambda_\mathrm{S})$ and (μ, μ_S) are the first and second Lamé parameters for an isotropic material:

$$
\begin{aligned}
\mathbb{H}_{ijkl} &= \lambda \delta_{ij}\delta_{kl} + \mu\big(\delta_{ik}\delta_{jl} + \delta_{il}\delta_{jk}\big) \\
\mathbb{S}_{ijkl} &= \lambda_{\mathrm{S}} P_{ij}P_{kl} + \mu_{\mathrm{S}}\big(P_{ik}P_{jl} + P_{il}P_{jk}\big)
\end{aligned}
\tag{2.12}
$$

The stress and strain tensors are given in tensorial notation as 3 × 3 matrices. Because the individual subdomains are considered as isotropic materials, those tensors are symmetric, the number of independent components reduces to 6 and can they be re-written under the Voigt notation (Annex 6.2).

$$
\sigma = \begin{bmatrix} \sigma_{11} & \sigma_{12} & \sigma_{31} \\ \sigma_{21} & \sigma_{22} & \sigma_{23} \\ \sigma_{31} & \sigma_{23} & \sigma_{33} \end{bmatrix} \qquad \varepsilon = \begin{bmatrix} \varepsilon_{11} & \varepsilon_{12} & \varepsilon_{31} \\ \varepsilon_{21} & \varepsilon_{22} & \varepsilon_{23} \\ \varepsilon_{31} & \varepsilon_{23} & \varepsilon_{33} \end{bmatrix}
\tag{2.13}
$$

- **Finite-Element Formulation**

The system of equations (2.9) is called the strong formulation because of the derivability requirements on unknown field. In the so-called weak formulation, the problem is re-formulated such that the derivability requirements is weakened. Indeed, the finite element method has been developed with the essential property that whenever a smooth classical solution exists, it is also a solution of the weak form. In order to solve this equation in complex domains, the space is discretized into the so-called finite-elements, and the solution is approximated by a sum of shape functions multiplied by the corresponding nodal value of the solution. The FEM equation for linear elasticity with the SET/SST model is

$$
\big(\mathbf{K}_{\mathrm{B}} + \mathbf{K}_{\mathrm{S}}\big)\mathbf{u} + \mathbf{M}\,\frac{d^2\mathbf{u}}{dt^2} = \mathbf{F}_{\mathrm{B}} + \mathbf{F}_{\mathrm{T}} - \mathbf{F}_{\mathrm{S}}
\tag{2.14}
$$

where $\mathbf{K}_{\mathrm{B}}$ is the bulk stiffness matrix, $\mathbf{K}_{\mathrm{S}}$ is the surface stiffness matrix, $\mathbf{M}$ is the mass matrix, $\mathbf{F}_{\mathrm{T}}$ is the vector of external loads, $\mathbf{F}_{\mathrm{B}}$ is the vector of body forces, $\mathbf{F}_{\mathrm{S}}$ is the vector of residual surface stress and $\mathbf{u}$ is the vector of nodal displacements. The demonstration is detailed in the Annexes 6.1 and 6.2. The different matrices appearing in the formulation are computed as follows:

$$
\begin{array}{l|l}
\mathbf{K}_{\mathrm{B}} = \displaystyle\int_{\Omega} \mathbf{B}\mathbf{D}_{\mathrm{B}}\mathbf{B}^{\top} d\mathbf{x} & \mathbf{F}_{\mathrm{B}} = \displaystyle\int_{\Omega} \mathbf{H}\rho\mathbf{g}\, d\mathbf{x} \\
\mathbf{K}_{\mathrm{S}} = \displaystyle\int_{\Gamma_{\mathrm{S}}} \mathbf{B}\mathbf{T}\mathbf{D}_{\mathrm{S}}\mathbf{T}^{\top}\mathbf{B}^{\top} d\mathbf{x} & \mathbf{F}_{\mathrm{T}} = \displaystyle\int_{\Gamma_{\mathrm{T}}} \mathbf{H}\mathbf{t}\, d\mathbf{x} \\
\mathbf{M} = \displaystyle\int_{\Omega} \mathbf{H}\mathbf{H}^{\top} \rho\, d\mathbf{x} & \mathbf{F}_{\mathrm{S}} = \displaystyle\int_{\Gamma_{\mathrm{S}}} \mathbf{B}\mathbf{T}\underline{\sigma}_0\, d\mathbf{x}
\end{array}
\tag{2.15}
$$

It is important to note that $\mathbf{K}_{\mathrm{S}}$ is symmetric but not positive-definite, meaning that $\mathbf{K}$ may lose its positive definiteness for some value of surface parameters, leading to an unstable system. For an isotropic material, the bulk stiffness tensor $\mathbf{D}_{\mathrm{B}}$ is given by

$$
\mathbf{D}_{\mathrm{B}} = \frac{E}{(1+\nu)(1-2\nu)}
\begin{bmatrix}
1-\nu & \nu & \nu & 0 & 0 & 0 \\
\nu & 1-\nu & \nu & 0 & 0 & 0 \\
\nu & \nu & 1-\nu & 0 & 0 & 0 \\
0 & 0 & 0 & \dfrac{1-2\nu}{2} & 0 & 0 \\
0 & 0 & 0 & 0 & \dfrac{1-2\nu}{2} & 0 \\
0 & 0 & 0 & 0 & 0 & \dfrac{1-2\nu}{2}
\end{bmatrix}
\tag{2.16}
$$

Similarly to the bulk stiffness tensor and if the surface is isotropic, $\mathbf{D}_{\mathrm{S}}$ is the second-order surface stiffness tensor of 36 components obtained by the independent components of the fourth-order tensor (2.12) by exploiting its symmetry. This stiffness tensor is given by

$$\mathbf{D}_{\mathrm{S}} = \begin{bmatrix} \mathbb{S}_{1111} & \mathbb{S}_{1122} & \mathbb{S}_{1133} & \mathbb{S}_{1112} & \mathbb{S}_{1123} & \mathbb{S}_{1113} \\ \mathbb{S}_{2211} & \mathbb{S}_{2222} & \mathbb{S}_{3322} & \mathbb{S}_{2212} & \mathbb{S}_{2223} & \mathbb{S}_{2213} \\ \mathbb{S}_{3311} & \mathbb{S}_{3322} & \mathbb{S}_{3333} & \mathbb{S}_{3312} & \mathbb{S}_{3323} & \mathbb{S}_{3313} \\ \mathbb{S}_{1211} & \mathbb{S}_{1222} & \mathbb{S}_{1233} & \mathbb{S}_{1212} & \mathbb{S}_{1223} & \mathbb{S}_{1213} \\ \mathbb{S}_{2311} & \mathbb{S}_{2322} & \mathbb{S}_{2333} & \mathbb{S}_{2312} & \mathbb{S}_{2323} & \mathbb{S}_{2313} \\ \mathbb{S}_{1311} & \mathbb{S}_{1322} & \mathbb{S}_{1333} & \mathbb{S}_{1312} & \mathbb{S}_{1323} & \mathbb{S}_{1313} \end{bmatrix} \tag{2.17}$$

which depends on $\mathbf{P}$ and the surface Lamé parameters previously defined. Because the projection tensors are symmetric and the norm $|\mathbf{n}|$ is unitary, this tensor can be decomposed into an isotropic surface stiffness tensor $\bar{\mathbf{D}}_{\mathrm{S}}$ and two transition matrices such that $\mathbf{D}_{\mathrm{S}} = \mathbf{T}\bar{\mathbf{D}}_{\mathrm{S}}\mathbf{T}^{\top}$ with the following form:

$$\bar{\mathbf{D}}_{\mathrm{S}} = \begin{bmatrix} 2\mu_{\mathrm{S}} + \lambda_{\mathrm{S}} & \lambda_{\mathrm{S}} & \lambda_{\mathrm{S}} & 0 & 0 & 0 \\ \lambda_{\mathrm{S}} & 2\mu_{\mathrm{S}} + \lambda_{\mathrm{S}} & \lambda_{\mathrm{S}} & 0 & 0 & 0 \\ \lambda_{\mathrm{S}} & \lambda_{\mathrm{S}} & 2\mu_{\mathrm{S}} + \lambda_{\mathrm{S}} & 0 & 0 & 0 \\ 0 & 0 & 0 & \mu_{\mathrm{S}} & 0 & 0 \\ 0 & 0 & 0 & 0 & \mu_{\mathrm{S}} & 0 \\ 0 & 0 & 0 & 0 & 0 & \mu_{\mathrm{S}} \end{bmatrix} \tag{2.18}$$

The matrix $\mathbf{H}$ is the matrix of shape functions, which simply contains a vector of nodal shape functions $\mathbf{N}$ for each dimension of space. Accordingly, the three directions $(u_x, u_y, u_z) = (u_1, u_2, u_3)$ of the displacement $\mathbf{u}$ are stored consecutively in a single vector. One can write

$$\mathbf{H} = \begin{bmatrix} \mathbf{N} & 0 & 0 \\ 0 & \mathbf{N} & 0 \\ 0 & 0 & \mathbf{N} \end{bmatrix} \qquad \mathbf{u} = \begin{bmatrix} \mathbf{u}_1 \\ \mathbf{u}_2 \\ \mathbf{u}_3 \end{bmatrix} \tag{2.19}$$

The matrix $\mathbf{B}$ contains the derivatives of the nodal shape functions $N_j(\mathbf{x})$ used for the discretization of space, with $j = 1 \dots \mathrm{J}$ and J is the number of nodes in an element of the mesh. Accordingly, we define the vector of $\mathbf{N}$ for each element, and its vector of nodal displacements as

$$\mathbf{B} = \begin{bmatrix} \frac{\partial \mathbf{N}}{\partial x} & 0 & 0 & \frac{\partial \mathbf{N}}{\partial y} & 0 & \frac{\partial \mathbf{N}}{\partial z} \\ 0 & \frac{\partial \mathbf{N}}{\partial y} & 0 & \frac{\partial \mathbf{N}}{\partial x} & \frac{\partial \mathbf{N}}{\partial z} & 0 \\ 0 & 0 & \frac{\partial \mathbf{N}}{\partial z} & 0 & \frac{\partial \mathbf{N}}{\partial y} & \frac{\partial \mathbf{N}}{\partial x} \end{bmatrix} \qquad \mathbf{N} = \begin{bmatrix} N_1 \\ N_2 \\ N_3 \\ \vdots \\ N_{\mathrm{J}} \end{bmatrix} \qquad \mathbf{u} = \begin{bmatrix} u_x^1 \\ \vdots \\ u_x^{\mathrm{J}} \\ u_y^1 \\ \vdots \\ u_z^{\mathrm{J}} \end{bmatrix} \tag{2.20}$$

Finally, $\mathbf{T}$ is the non-symmetric transition matrix representing the mapping between the bulk and surface quantities in Voigt notation, this latter can be computed analytically from the property (6.16) and is given as a function of the projection tensor:

$$\mathbf{T} = \begin{bmatrix} P_{11}^2 & P_{12}^2 & P_{31}^2 & 2P_{11}P_{12} & 2P_{31}P_{12} & 2P_{11}P_{31} \\ P_{12}^2 & P_{22}^2 & P_{23}^2 & 2P_{12}P_{22} & 2P_{23}P_{22} & 2P_{12}P_{23} \\ P_{31}^2 & P_{23}^2 & P_{33}^2 & 2P_{23}P_{31} & 2P_{23}P_{33} & 2P_{33}P_{31} \\ P_{11}P_{12} & P_{12}P_{22} & P_{31}P_{23} & P_{11}P_{22} + P_{12}^2 & P_{31}P_{22} + P_{23}P_{12} & P_{31}P_{12} + P_{11}P_{23} \\ P_{12}P_{31} & P_{23}P_{22} & P_{23}P_{33} & P_{22}P_{31} + P_{12}P_{23} & P_{22}P_{33} + P_{23}^2 & P_{23}P_{31} + P_{12}P_{33} \\ P_{11}P_{31} & P_{12}P_{23} & P_{33}P_{31} & P_{12}P_{31} + P_{11}P_{23} & P_{31}P_{23} + P_{33}P_{12} & P_{33}P_{11} + P_{31}^2 \end{bmatrix}$$

The equation (2.14) discretized in space, but not in time as $\mathbf{u}$ is function of the time. There exist different methods for the time discretization, which can be categorized either as explicit or implicit scheme.

In the quasistatic approximation, the time derivative is neglected and the system can be solved in one single step. A summary of the procedure is presented Figure 5. One may notice that the classical linear elasticity model (LE) is retrieved when $\mathbf{K}_{\mathrm{S}}$ and $\mathbf{F}_{\mathrm{S}}$ are zero.

2.4 Saint Venant–Kirchhoff Model

The Saint Venant–Kirchhoff model is an extension of the geometrically linear elastic material model to the geometrically nonlinear regime. This model does not take into account surface effects and is valid for linear elastic materials under large strain (in addition to small strains). Under the quasi-static approximation and neglecting body forces, one can write

$$\begin{cases} \nabla \cdot \sigma = 0 & \text{in } \Omega \quad (\text{PDE}) \\ \sigma \cdot \mathbf{n} = \mathbf{t} & \text{on } \Gamma_{\mathrm{T}} \quad (\text{BC}) \\ u = \bar{u} & \text{on } \Gamma_{\mathrm{U}} \quad (\text{BC}) \end{cases} \tag{2.21}$$

In the finite strain theory, the complete description of the strain tensor is used, meaning that all the quadratic terms in ε presented in (2.1) are taken into account. Moreover, the dependency of the spatial domain $\Omega(u)$ in the displacement field is considered and the integration domain thus depends on the variable on which the integration is performed in the variational formulation:

$$\begin{cases} \nabla_{\mathbf{x}} \cdot \sigma(\mathbf{x}) = 0 & \text{in } \Omega(u) \\ \varepsilon = \frac{1}{2}\left(\nabla_{\mathbf{x}} u + \nabla_{\mathbf{x}} u^{\top} + \nabla_{\mathbf{x}} u \nabla_{\mathbf{x}} u^{\top}\right) & \text{in } \Omega(u) \end{cases} \tag{2.22}$$

The notation $\nabla_{\mathbf{x}}$ indicates that the derivatives are performed with respect to the current configuration, which is now significantly different from the initial configuration. In order to solve this system, the total Lagrangian formulation is proposed. In this formulation, the integration is performed with respect to the initial configuration, then alternative stress and strain measures are used in order to take info account the evolution of Ω with the displacement:

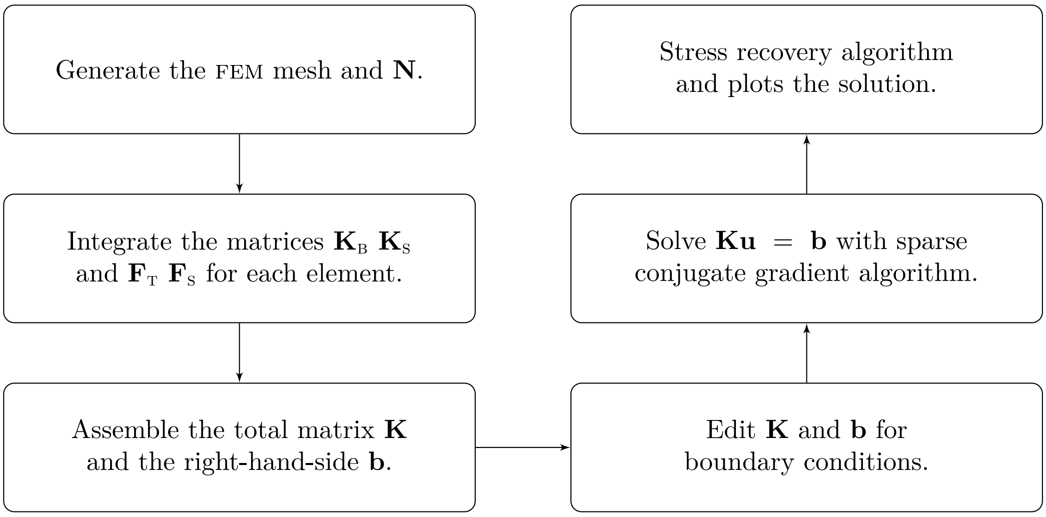

Figure 5: Flowchart of the FEM algorithm for the SET/SST model. In this work, a quasistatic case is assumed and the effect of the body forces such as the weight of the thin film is neglected, leading to the following simplifications: $\partial^2/\partial t^2 = 0$ and $\mathbf{F}_{\mathrm{B}} = 0$. The algorithm for classical linear elasticity (LE) is identical to SET/SST in the particular case $\mathbf{K}_{\mathrm{S}} = 0$ and $\mathbf{F}_{\mathrm{S}} = 0$.

$$\int_{\Omega_0} \mathbf{S} : \mathbf{E}_w \, d\mathbf{x} = \int_{\Gamma_0} w^\top \mathbf{t} \, d\mathbf{x} \tag{2.23}$$

where $\mathbf{S} = \mathbb{D} : \mathbf{E}$ is the second Piola-Kirchhoff stress tensor for a simple Saint Venant-Kirchhoff material and $\mathbf{E}$ is the Green-Lagrange strain tensor and $\mathbf{E}_w$ the equivalent virtual strain. Ω_0 and Γ_0 denote the reference volume and surface Γ_{T} respectively. As the system is nonlinear, the finite element solution is recovered by a Newton-Raphson algorithm and the left-hand side of (2.23) must be linearized. Consequently, the following linear system is solved iteratively until the right-hand side vanishes:

$$\big(\mathbf{K}_{\mathrm{N}} + \mathbf{K}_{\mathrm{L}}\big)\delta\mathbf{u} = \mathbf{F}_{\mathrm{T}} - \mathbf{F}_{\mathrm{X}} \tag{2.24}$$

where $\mathbf{K}_{\mathrm{N}}$ and $\mathbf{K}_{\mathrm{L}}$ are linearized stiffness matrices, also called tangent stiffness matrices, $\delta\mathbf{u}$ is the displacement increment, $\mathbf{F}_{\mathrm{T}}$ is the surface traction vector and $\mathbf{F}_{\mathrm{X}}$ is the vector of internal stresses in the system. Thus the right-hand side represents the out-of-equilibrium forces. The total displacement at the j-th iteration is given by $\mathbf{u}_j = \mathbf{u}_{j-1} + \delta\mathbf{u}_j$. A more detailed description of the result (2.24) is presented in the Annex 6.3. Practically, one can write

$$\begin{array}{l|l}
\mathbf{K}_{\mathrm{N}} = \displaystyle\int_{\Omega_0} \mathbf{B}_{\mathrm{N}}\mathbf{D}_{\mathrm{B}}\mathbf{B}_{\mathrm{N}}^\top \, d\mathbf{x} & \quad \mathbf{F}_{\mathrm{T}} = \displaystyle\int_{\Gamma_0} \mathbf{H}\mathbf{t} \, d\mathbf{x} \\
\mathbf{K}_{\mathrm{L}} = \displaystyle\int_{\Omega_0} \mathbf{B}_{\mathrm{L}}\mathbf{\Sigma}\mathbf{B}_{\mathrm{L}}^\top \, d\mathbf{x} & \quad \mathbf{F}_{\mathrm{X}} = \displaystyle\int_{\Omega_0} \mathbf{B}_{\mathrm{N}}\mathbf{D}_{\mathrm{B}}\underline{E} \, d\mathbf{x}
\end{array} \tag{2.25}$$

These matrices depend on the current state $\mathbf{u}_{j-1}$ of the structure. Consequently, one must update the stiffness matrices and the internal stress at each iteration of the Newton-Raphson algorithm. The matrices $\mathbf{D}_{\mathrm{B}}$ and $\mathbf{H}$ are the same as in the previous section, $\mathbf{B}_{\mathrm{N}}$ is the nonlinear displacement-strain matrix and is clearly different from $\mathbf{B}$. The matrix $\mathbf{B}_{\mathrm{L}}$ provides a linear relation between displacement and strain. Practically, it can be shown that those matrices are given by

$$\mathbf{B}_{\mathrm{N}} = \begin{bmatrix}
F_{11}\frac{\partial \mathbf{N}}{\partial x} & F_{12}\frac{\partial \mathbf{N}}{\partial y} & F_{13}\frac{\partial \mathbf{N}}{\partial z} & F_{11}\frac{\partial \mathbf{N}}{\partial y} + F_{12}\frac{\partial \mathbf{N}}{\partial x} & F_{12}\frac{\partial \mathbf{N}}{\partial z} + F_{13}\frac{\partial \mathbf{N}}{\partial y} & F_{13}\frac{\partial \mathbf{N}}{\partial x} + F_{11}\frac{\partial \mathbf{N}}{\partial z} \\
F_{21}\frac{\partial \mathbf{N}}{\partial x} & F_{22}\frac{\partial \mathbf{N}}{\partial y} & F_{23}\frac{\partial \mathbf{N}}{\partial z} & F_{21}\frac{\partial \mathbf{N}}{\partial y} + F_{22}\frac{\partial \mathbf{N}}{\partial x} & F_{22}\frac{\partial \mathbf{N}}{\partial z} + F_{23}\frac{\partial \mathbf{N}}{\partial y} & F_{23}\frac{\partial \mathbf{N}}{\partial x} + F_{21}\frac{\partial \mathbf{N}}{\partial z} \\
F_{31}\frac{\partial \mathbf{N}}{\partial x} & F_{32}\frac{\partial \mathbf{N}}{\partial y} & F_{33}\frac{\partial \mathbf{N}}{\partial z} & F_{31}\frac{\partial \mathbf{N}}{\partial y} + F_{32}\frac{\partial \mathbf{N}}{\partial x} & F_{32}\frac{\partial \mathbf{N}}{\partial z} + F_{33}\frac{\partial \mathbf{N}}{\partial y} & F_{33}\frac{\partial \mathbf{N}}{\partial x} + F_{31}\frac{\partial \mathbf{N}}{\partial z}
\end{bmatrix}$$

$$\mathbf{B}_{\mathrm{L}} = \begin{bmatrix}
\frac{\partial \mathbf{N}}{\partial x} & 0 & 0 & \frac{\partial \mathbf{N}}{\partial y} & 0 & 0 & 0 & 0 & \frac{\partial \mathbf{N}}{\partial z} \\
0 & \frac{\partial \mathbf{N}}{\partial y} & 0 & 0 & \frac{\partial \mathbf{N}}{\partial x} & \frac{\partial \mathbf{N}}{\partial z} & 0 & 0 & 0 \\
0 & 0 & \frac{\partial \mathbf{N}}{\partial z} & 0 & 0 & 0 & \frac{\partial \mathbf{N}}{\partial y} & \frac{\partial \mathbf{N}}{\partial x} & 0
\end{bmatrix} \tag{2.26}$$

The matrix $\mathbf{\Sigma}$ contains the components of the second Piola-Kirchhoff stress tensor. By exploiting the symmetry, these components can be computed in a 3×3 symmetric matrix $\mathbf{S} = \mathbf{D}_{\mathrm{B}}\mathbf{E}$ with the nodal solution of the element in the previous iteration, one has then

$$\mathbf{\Sigma} = \begin{bmatrix}
S_{11} & 0 & 0 & S_{12} & 0 & 0 & 0 & 0 & S_{31} \\
0 & S_{22} & 0 & 0 & S_{12} & S_{23} & 0 & 0 & 0 \\
0 & 0 & S_{33} & 0 & 0 & 0 & S_{23} & S_{31} & 0 \\
S_{12} & 0 & 0 & S_{22} & 0 & 0 & 0 & 0 & S_{23} \\
0 & S_{12} & 0 & 0 & S_{11} & S_{31} & 0 & 0 & 0 \\
0 & S_{23} & 0 & 0 & S_{31} & S_{33} & 0 & 0 & 0 \\
0 & 0 & S_{23} & 0 & 0 & 0 & S_{22} & S_{12} & 0 \\
0 & 0 & S_{31} & 0 & 0 & 0 & S_{12} & S_{11} & 0 \\
S_{31} & 0 & 0 & S_{23} & 0 & 0 & 0 & 0 & S_{33}
\end{bmatrix} \tag{2.27}$$

Finally, the Green-Lagrange strain is computed with the components of the deformation gradient tensor $\mathbf{F}$, relating the derivative with respect to the current coordinate $\mathbf{x}$ and the derivative with respect to the reference coordinates $\mathbf{X}$. The vector $\underline{E}$ denotes the Voigt notation of $\mathbf{E}$. One can write

$$\begin{aligned} \mathbf{E} &= \frac{1}{2}\left(\mathbf{F}^\top \mathbf{F} - \mathbf{I}\right) \\ \mathbf{F} &= \mathbf{I} + \nabla_{\mathbf{X}} u = \nabla_{\mathbf{X}}(\mathbf{x}) \end{aligned} \tag{2.28}$$

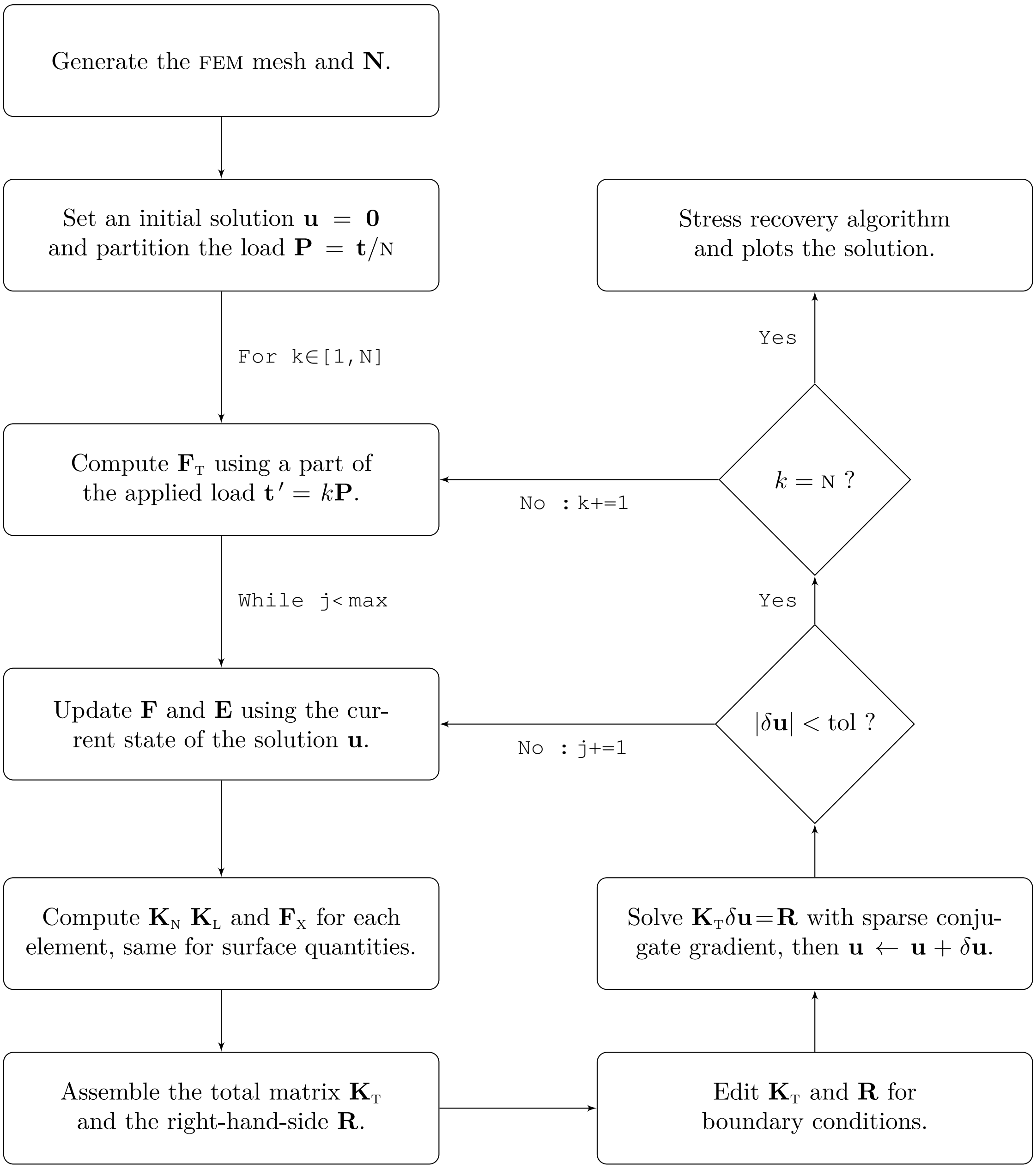

Figure 6: Flowchart of the finite element algorithm for the Saint Venant-Kirchhoff (SVK) model. The variable `tol` is the maximum tolerance of the Newton Raphson method, this latter is generally normalized by a reference value in order to suppress the influence of the units on the convergence criterion. Generally, if the iteration `j=max` is reached, the last load increment is cancelled and a smaller load increment is used for the rest of the solving process.

It is straightforward to show that the components of **F** in any finite element of the mesh can be easily computed in a vector $\underline{F}$ using the matrix (2.26) obtained previously and the current state of the nodal displacement vector by the following relation:

$$\underline{F} = \begin{bmatrix} F_{11} \\ F_{22} \\ F_{33} \\ F_{12} \\ F_{21} \\ F_{23} \\ F_{32} \\ F_{31} \\ F_{13} \end{bmatrix} = \begin{bmatrix} \partial \mathbf{N}/\partial x & 0 & 0 \\ 0 & \partial \mathbf{N}/\partial y & 0 \\ 0 & 0 & \partial \mathbf{N}/\partial z \\ \partial \mathbf{N}/\partial y & 0 & 0 \\ 0 & \partial \mathbf{N}/\partial x & 0 \\ 0 & \partial \mathbf{N}/\partial z & 0 \\ 0 & 0 & \partial \mathbf{N}/\partial y \\ 0 & 0 & \partial \mathbf{N}/\partial x \\ \partial \mathbf{N}/\partial z & 0 & 0 \end{bmatrix} \begin{bmatrix} u_1 \\ u_2 \\ u_3 \end{bmatrix} + \begin{bmatrix} 1 \\ 1 \\ 1 \\ 0 \\ 0 \\ 0 \\ 0 \\ 0 \\ 0 \end{bmatrix} = \mathbf{B}_{\mathrm{L}}^{\top} \mathbf{u} + \mathbb{1} \tag{2.29}$$

2.5 Boundary Conditions

The last step of the finite element algorithm is the resolution of a linear system of equations $\mathbf{Ku} = \mathbf{b}$ to be solved at each step of the SVK model. In the SET/SST model, one has simply $\mathbf{K} = \mathbf{K}_{\mathrm{B}} + \mathbf{K}_{\mathrm{S}}$ and $\mathbf{b} = \mathbf{F}_{\mathrm{T}} - \mathbf{F}_{\mathrm{S}}$. This system is solved by using the conjugate gradient method because this latter has modest memory requirement in addition to be less computationally expensive for large sparse matrices. The conjugate gradient method is an iterative solver for positive definite and symmetric matrices, which means that **K** must remain symmetric after the application of the boundary conditions in order to use this algorithm [22]. Moreover, 3D meshes tend to generate very large matrices where the number of elements is significantly high, even when only non-zero entries are stored in the sparse matrix. Thereby, in addition to the symmetry requirement for the conjugate gradient solver, the symmetry of **K** will be exploited in order to reduce the memory required for its storage as only the upper-triangle and the diagonal elements will be effectively stored in the matrix. That is, the following section is concerned about maintaining the matrix symmetric during the process of applying the boundary conditions.

- **Neumann and Dirichlet**

Neumann boundary conditions concern the derivative of the unknown and are naturally taken into account in the finite element formulation. Indeed, the vector **F** at the right-hand-side contains the external applied loads $\sigma \cdot \mathbf{n}$ denoting the derivative of the solution at the boundary of the domain. However, the fourth equation of (2.9) is the Dirichlet boundary condition and concerns the value of the unknown field, which must be enforced thereafter. For simplicity, consider the system

$$\begin{bmatrix} k_{11} & k_{12} & k_{13} & k_{14} \\ k_{21} & k_{22} & k_{23} & k_{24} \\ k_{31} & k_{32} & k_{33} & k_{34} \\ k_{41} & k_{42} & k_{43} & k_{44} \end{bmatrix} \begin{bmatrix} u_1 \\ u_2 \\ u_3 \\ u_4 \end{bmatrix} = \begin{bmatrix} b_1 \\ b_2 \\ b_3 \\ b_4 \end{bmatrix} \tag{2.30}$$

Imposing the Dirichlet condition $u_3 = h$ on the third variable of this system can be achieved first by setting the third row of **K** to zero, the diagonal element to one and the corresponding row of **b** to h. In order to maintain the symmetry of **K**, one may modify the matrix by replacing the variable u_3 by its imposed value in each of the equations and move this constant on the right-hand-side:

$$\begin{bmatrix} k_{11} & k_{12} & 0 & k_{14} \\ k_{21} & k_{22} & 0 & k_{24} \\ 0 & 0 & 1 & 0 \\ k_{41} & k_{42} & 0 & k_{44} \end{bmatrix} \begin{bmatrix} u_1 \\ u_2 \\ u_3 \\ u_4 \end{bmatrix} = \begin{bmatrix} b_1 - k_{13}h \\ b_2 - k_{23}h \\ h \\ b_4 - k_{43}h \end{bmatrix} \tag{2.31}$$

- **Periodic Conditions**

Periodic boundary conditions are typically implemented for simulations involving a representative volume element of an infinite system. Those conditions appear in two different cases. First, when one wants to impose that two or more variables have equal values, for instance, one may impose $u_i = u_j$ by performing a change of variable in the linear system

$$u_i \longrightarrow \Delta u_{ij} = u_i - u_j \tag{2.32}$$

then set this new variable to zero, as for the Dirichlet condition previously presented. This method has the advantage of maintaining the symmetry of $\mathbf{K}$. It is clear that the reverse case leads to the same system with $\Delta u_{ij} = -\Delta u_{ji}$. The procedure and the result for $(i,j) = (2,3)$ are

$$\begin{bmatrix} k_{11} & 0 & k_{13}+k_{12} & k_{14} \\ 0 & 1 & 0 & 0 \\ k_{31}+k_{21} & 0 & (k_{33}+k_{23})+(k_{32}+k_{22}) & k_{34}+k_{24} \\ k_{41} & 0 & k_{43}+k_{42} & k_{44} \end{bmatrix} \begin{bmatrix} u_1 \\ \Delta u_{23} \\ u_3 \\ u_4 \end{bmatrix} = \begin{bmatrix} b_1 \\ 0 \\ b_3+b_2 \\ b_4 \end{bmatrix} \tag{2.33}$$

The second case is when one must impose that a set of linear combinations two variables must be equal. This particular case is presented in Figure 7 when the strain field in the periodic structure is decomposed into a global strain Δu which must be constant along the transverse dimensions of the strained axis, and a local fluctuation δu which must be equal for each paired nodes, one has

$$\begin{cases} u_4 = \delta u_{14} \\ u_1 = \Delta u_{14} + \delta u_{14} \end{cases} \qquad \begin{cases} u_3 = \delta u_{23} \\ u_2 = \Delta u_{23} + \delta u_{23} \end{cases} \tag{2.34}$$

with $\Delta u_{23} = \Delta u_{14}$ in order to simulate an infinite periodic system along the corresponding dimension. The procedure is similar to the one presented above, but limited to the change of variable without cancellation of the new variable, first for $(i,j) = (2,3)$, then repeat the operation for the second pair of coupled nodes $(i,j) = (1,4)$, leading to the following system:

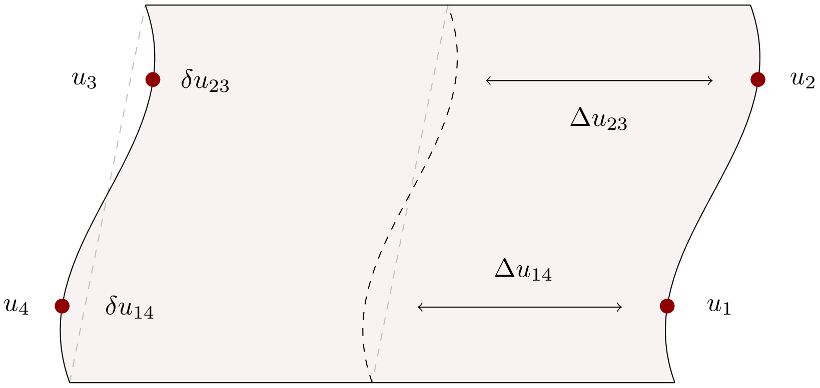

Figure 7: Example of periodic boundary conditions for the deformation of a representative elementary volume of an infinite system. The shape of the deformed configuration must be compatible with a periodic assembly of the same configuration in the considered dimensions. Meaning that the final width of the structure must remain constant for any pair of nodes. This imposes that the change in width Δu_{ij} is equal for any pair (i,j) of coupled nodes.

$$\begin{bmatrix} k_{11} & k_{12} & k_{13}+k_{12} & k_{14} \\ k_{21} & k_{22} & k_{23}+k_{22} & k_{24} \\ k_{31}+k_{21} & k_{32}+k_{22} & (k_{33}+k_{23})+(k_{32}+k_{22}) & k_{34}+k_{24} \\ k_{41} & k_{42} & k_{43}+k_{42} & k_{44} \end{bmatrix} \begin{bmatrix} u_1 \\ \Delta u_{23} \\ u_3 \\ u_4 \end{bmatrix} = \begin{bmatrix} b_1 \\ b_2 \\ b_3+b_2 \\ b_4 \end{bmatrix} \tag{2.35}$$

$$\begin{bmatrix} k_{11} & k_{12} & k_{13}+k_{12} & k_{14}+k_{11} \\ k_{21} & k_{22} & k_{23}+k_{22} & k_{24}+k_{21} \\ k_{31}+k_{21} & k_{32}+k_{22} & (k_{33}+k_{23})+(k_{32}+k_{22}) & (k_{34}+k_{24})+(k_{31}+k_{21}) \\ k_{41}+k_{11} & k_{42}+k_{12} & (k_{43}+k_{42})+(k_{13}+k_{12}) & (k_{44}+k_{14})+(k_{41}+k_{11}) \end{bmatrix} \begin{bmatrix} \Delta u_{14} \\ \Delta u_{23} \\ u_3 \\ u_4 \end{bmatrix} = \begin{bmatrix} b_1 \\ b_2 \\ b_3+b_2 \\ b_4+b_1 \end{bmatrix}$$

Now that two unknowns of the system are expressed in terms of the new variables Δu, the last step is to enforce $\Delta u_{23} = \Delta u_{14}$ using the algorithm (2.33) previously presented for the first and second equations of the system, so with $(i, j) = (2, 1)$ leading to the system (2.36). It is important to note that if $\mathbf{K}$ is symmetric, positive definite and singular, the new matrix $\mathbf{K}'$ is still symmetric and semi-positive but not singular if the boundary conditions are sufficient for suppressing the rigid body motions

$$\mathbf{K}' = \begin{bmatrix} (k_{11}+k_{21})+(k_{12}+k_{22}) & 0 & (k_{13}+k_{12})+(k_{23}+k_{22}) & (k_{14}+k_{11})+(k_{24}+k_{21}) \\ 0 & 1 & 0 & 0 \\ (k_{31}+k_{21})+(k_{32}+k_{22}) & 0 & (k_{33}+k_{23})+(k_{32}+k_{22}) & (k_{34}+k_{24})+(k_{31}+k_{21}) \\ (k_{41}+k_{11})+(k_{42}+k_{12}) & 0 & (k_{43}+k_{42})+(k_{13}+k_{12}) & (k_{44}+k_{14})+(k_{41}+k_{11}) \end{bmatrix}$$

$$\mathbf{u}' = \begin{bmatrix} \Delta u_{14} \\ \Delta u_{23} - \Delta u_{14} \\ u_3 \\ u_4 \end{bmatrix} \qquad \mathbf{b}' = \begin{bmatrix} b_1+b_2 \\ 0 \\ b_3+b_2 \\ b_4+b_1 \end{bmatrix} \tag{2.36}$$

Chapter 3

Model Validation

3.1 Cantilever Beam

2

Verification of the implementation
by solving different test-cases.

The cantilever beam is a very common verification test in finite element methods because it leads to a nonlinear displacement field and can be easily approximated by an analytical solution in 2D under the assumption of small deformations. This model is for instance used in convergence analysis. The analytical solution is directly derived from the fundamental equation of elasticity:

$$\frac{d^2u}{dx^2} = \frac{-M(x)}{EI} = \frac{Px^2}{2EI} \tag{3.1}$$

where $u(x)$ is the vertical displacement of the cantilever beam at a distance x from the free side, $M(x)$ is the momentum generated by the equally distributed linear load P and I is the momentum of inertia of the cross-section of the beam. Integrating this expression twice gives

$$\begin{aligned} \frac{du}{dx} &= \frac{Px^3}{6EI} + C_1 \\ u &= \frac{Px^4}{24EI} + C_1 x + C_2 \end{aligned} \tag{3.2}$$

One can finally use the boundary conditions to obtain the integration constants. The left-side of the beam is clamped such that $u = 0$ at $x = L$ and the slope of the beam must be zero at this same position. This solution is presented in Figure 10 with the numerical solution described further.

$$\begin{cases} \dfrac{du}{dx}\big(x = L\big) = 0 \\ u\big(x = L\big) = 0 \end{cases} \Leftrightarrow \begin{cases} C_1 = \dfrac{-PL^3}{6EI} \\ C_2 = \dfrac{PL^4}{8EI} \end{cases} \tag{3.3}$$

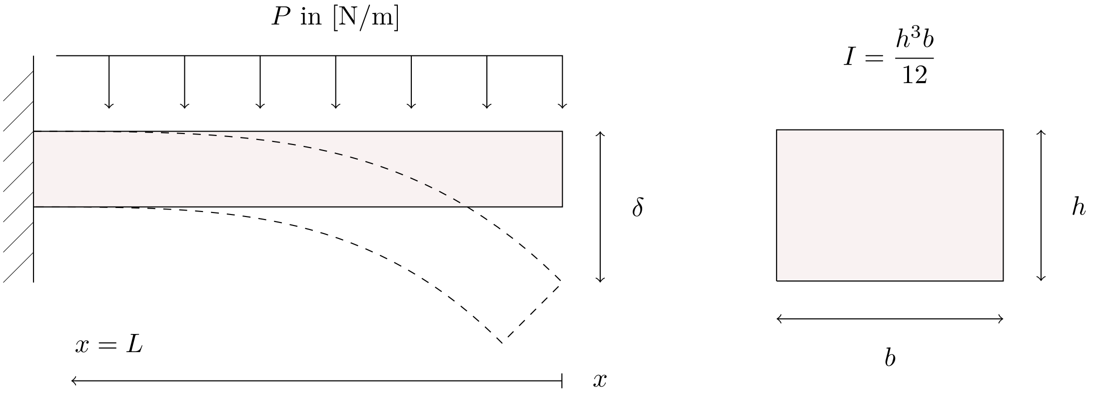

Figure 8: Representation of the cantilever beam for the flexion test case. The boundary conditions at the clamped surface are $u_x = 0$ on the whole surface, $u_y = 0$ on the bottom side of the surface and $u_z = 0$ on the bottom corner such that the beam can change its volume and transverse stresses are not generated due to the Poisson's ratio.

The vertical deflection δ at the end of the beam is simply obtained by $u(x=0)$. It is important to note that this solution is correct under some approximations, for instance shear deformation that depend on the depth and length of the beam are not taken into account. The horizontal displacement of the beam is also neglected in small deformations. For an applied force of $P = -10$ kN/m on a beam of dimensions $L = 50$ cm, $b = 5$ cm and $h = 2$ cm with $\nu = 0.28$ and $E = 210$ GPa, one has

$$\delta = \frac{PL^4}{8EI} = -1.116 \text{ cm} \tag{3.4}$$

- **Numerical Solution**

The simulation is performed with the configuration presented in Figure 8. The elements composing the mesh are second-order hexahedron because those elements provide a faster convergence to the exact solution when this latter is not linear. The results of the finite element simulation are presented in Figure 9. As expected, the numerical solution converges to the analytical solution when the number of elements in the mesh increases (Figure 10). If a quasi-static case in small strain is considered and $\mathbf{F}_{\mathrm{B}} = 0$ in addition to $\mathbb{S} = 0$ and $\tau_0 = 0$, the FEM equation is (2.14) and reduces to the LE model:

$$\mathbf{K}_{\mathrm{B}}\mathbf{u} = \mathbf{F}_{\mathrm{T}} \quad \text{with} \quad \mathbf{t} = \begin{bmatrix} 0 & 0 & P/b \end{bmatrix} \tag{3.5}$$

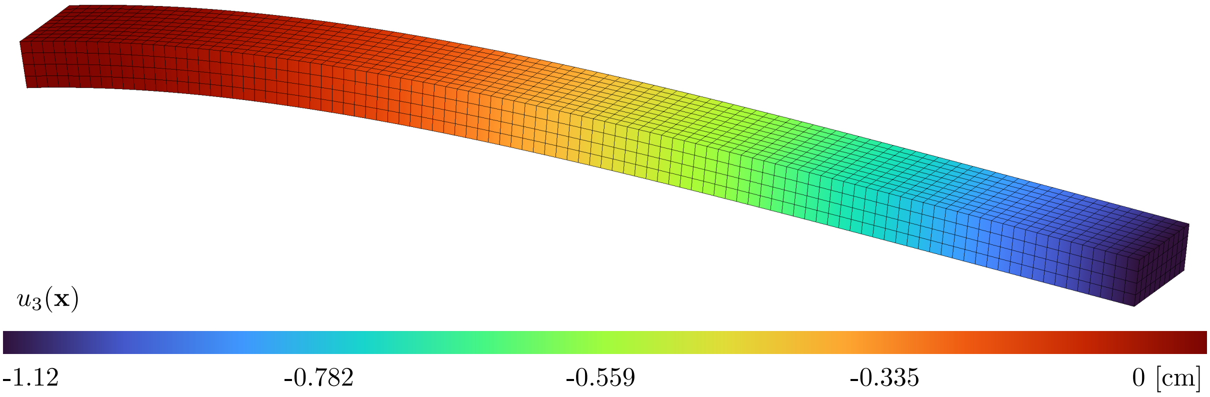

Figure 9: FEM solution δ for the bending of the cantilever beam. The mesh in the picture is composed of 4×10^3 Lagrange hexahedron of order two. The parameters of the simulation are $L = 50$ cm, $b = 5$ cm and $h = 2$ cm with $\nu = 0.28$, $E = 210$ GPa and $\mathbf{t} = [0\ 0\ -2] \times 10^{-4}$ GPa.

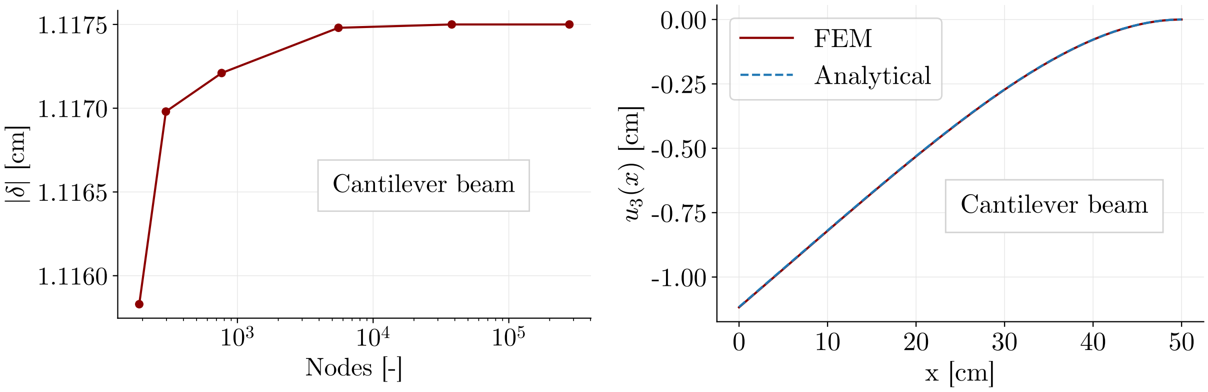

Figure 10: Displacement of the cantilever beam. The solution converges to the analytical solution (3.4) when the number of nodes increases. The graph on the right shows that the analytical and FEM solutions are identical at any points along the length of the beam.

3.2 Nanoplate Relaxation

A second test case in order to validate proposed FEM code is similar to the one proposed in [23] with the relaxation of a solid nanoplate under the effect of surface tension, similarly to liquid films. The mechanical equilibrium of the system presented in Figure 11 can be analyzed by applying the principle of virtual work. Because of the natural tendency for the film is to reduce its area as much as possible, the force F is necessary to prevent the area from decreasing. If one move the wire to the right by a small distance dx, the resulting mechanical work and the change in energy are

$$\begin{aligned} \delta W &= F\,dx \\ \delta U &= 2\tau_0 L\,dx \end{aligned} \tag{3.6}$$

where $L\,dx$ is the variation of the area enclosed by the wire, τ_0 is the energy per unit area of the free surface also called surface tension. The factor 2 accounts for the fact that the film has two free surfaces, one on the top and the other on the bottom. Equaling δW with δU leads to

$$F = 2\tau_0 L \tag{3.7}$$

- **Analytical Solution**

In the context of the relaxation of a nanoplate with two free surfaces due to the effect of surface tension, an analytical solution for the displacement field can be obtained by solving the quasi-static equation of motion, with the equivalent surface stress $\sigma \cdot \mathbf{n} = -F/A$ along the x-axis, and Dirichlet boundary conditions of zero displacement of the fixed surfaces. As the body forces are neglected and the shear stress is prevented by the boundary conditions, the stress field is constant:

$$\begin{cases} \dfrac{\partial \sigma_{11}}{\partial x} + \dfrac{\partial \sigma_{12}}{\partial y} + \dfrac{\partial \sigma_{13}}{\partial z} + \rho b_x = \dfrac{\partial^2 u_x}{\partial x} \\ \dfrac{\partial \sigma_{21}}{\partial x} + \dfrac{\partial \sigma_{22}}{\partial y} + \dfrac{\partial \sigma_{23}}{\partial z} + \rho b_y = \dfrac{\partial^2 u_y}{\partial y} \\ \dfrac{\partial \sigma_{31}}{\partial x} + \dfrac{\partial \sigma_{32}}{\partial y} + \dfrac{\partial \sigma_{33}}{\partial z} + \rho b_z = \dfrac{\partial^2 u_z}{\partial z} \end{cases} \Leftrightarrow \begin{cases} \dfrac{\partial \sigma_{11}}{\partial x} = 0 \\ \dfrac{\partial \sigma_{22}}{\partial y} = 0 \\ \dfrac{\partial \sigma_{33}}{\partial z} = 0 \end{cases} \tag{3.8}$$

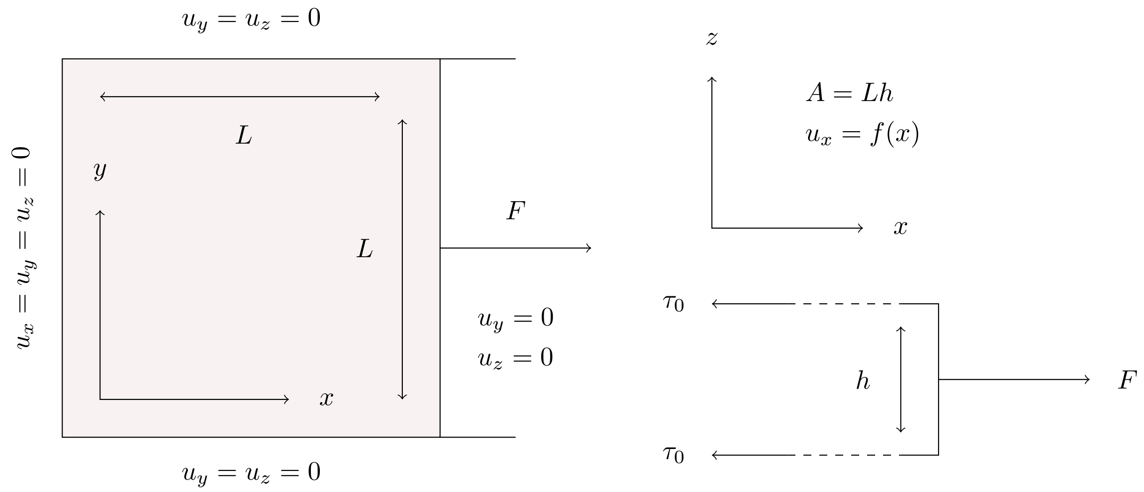

Figure 11: Mechanical equilibrium of a liquid film on a wire. The height of the film is neglected and only the right side of the film is able to move in the axial dimension. A is the surface area of the film, τ_0 is the surface tension and F is an applied force in the opposite direction.

Table 1: Values of the surface tension as well as the first and second Lamé surface parameters for an isotropic surface in different crystal orientations. Those results have been obtained using the embedded atom method and reported in [24]. The surface bulk modulus is computed from (3.14).

Aluminum	λ_S [J/m^2]	μ_S [J/m^2]	τ_0 [J/m^2]	K_S [J/m^2]
Face [100]	3.494	-5.425	0.569	-7.356
Face [111]	6.851	-0.376	0.91	6.099

It is important to note that the effect of surface stiffness tensor $\mathbb{S}$ is neglected in the analytical solution. As the applied stress on the right side of the plate is enforced, the axial stress along the x-axis is deduced from the boundary condition at $x = L$. Using the relation (3.7) for expressing the stress field as a function of the surface tension, one can write

$$\sigma_{11} = \frac{-F}{A} = \frac{-2\tau_0}{h} \tag{3.9}$$

As presented in a previous chapter, the constitutive model for the elastic deformation of an isotropic material is given by the generalized Hook's law and leads to the following stress-strain relation, where the strain field along the y-axis and the z-axis are zero due the Dirichlet conditions:

$$\begin{aligned} \varepsilon_{11} &= \frac{1}{E}\Big[\sigma_{11} - \nu\big(\sigma_{22} + \sigma_{33}\big)\Big] \\ \varepsilon_{22} &= \frac{1}{E}\Big[\sigma_{22} - \nu\big(\sigma_{11} + \sigma_{33}\big)\Big] = 0 \\ \varepsilon_{33} &= \frac{1}{E}\Big[\sigma_{33} - \nu\big(\sigma_{11} + \sigma_{22}\big)\Big] = 0 \end{aligned} \tag{3.10}$$

The two last equations form a system of two equations and two unknowns as σ_{11} is known, and can thus be solved independently. The strain field ε_{11} is then obtained by injecting the stress σ_{22} and σ_{33} into the equation of the system, leading to

$$\begin{aligned} \sigma_{22} = \sigma_{33} &= \frac{\nu(1+\nu)}{1-\nu^2}\sigma_{11} \\ \varepsilon_{11} &= \frac{\sigma_{11}}{E}\left[1 - 2\frac{\nu^2(1+\nu)}{1-\nu^2}\right] \\ u_x(x) &= \varepsilon_{11}x \end{aligned} \tag{3.11}$$

The test case is presented with Al as the bulk material with $E = 70$ GPa, $\nu = 0.33$ and the surface tension $\tau_0 = 0.91$ J/m^2 referenced in [25][26]. For a nanoplate of dimensions $L = 10$ μm and thickness $h = 10$ nm, the strain field and the maximum displacement on the right side of the nanoplate are

$$\begin{aligned} \varepsilon_{11} &= -1.755 \times 10^{-3} \\ u_x(L) &= -17.55 \text{ nm} \end{aligned} \tag{3.12}$$

- **Numerical Solution**

For the FEM simulation, the situation previously presented is reproduced. That is, the Dirichlet boundary conditions and the nanoplate dimensions are the same as in Figure 11. In the FEM formulation of the problem (2.14), the time derivatives are set to zero as we want to compute the steady-state solution, the body forces $\mathbf{F}_\text{B}$ are also neglected due to the length scale of the plate.

Finally, the applied forces $\mathbf{F}_\text{T}$ are set to zero such that only the surface tension $\mathbf{F}_\text{S}$ participates to the deformation of the nanoplate through its two free surfaces at the top and at the bottom. As a reminder, the equation to be solved in this situation is given by the SET/SST (2.14) and reduces to

$$\big(\mathbf{K}_\text{B} + \mathbf{K}_\text{S}\big)\mathbf{u} = -\mathbf{F}_\text{S} \tag{3.13}$$

The Lamé parameters for the free surfaces as well as the surface tensions are given in Table 1 for two different crystal orientations [100] and [111]. The effect of the surface stiffness matrix $\mathbf{K}_\text{S}$ is compared to the solution where this latter is neglected is either to strengthen or weaken the overall material stiffness depending on the value of the surface bulk modulus [27] defined by

$$K_\text{S} = \lambda_\text{S} + 2\mu_\text{S} \tag{3.14}$$

The results for the different configurations are presented in Figure 12 and Figure 13. It can be seen that the analytical solution derived in (3.12) is correctly represented by the FEM code. In addition, the effect of the surface stiffness tends to make the overall structure stiffer when K_S is positive, or weaken the structure when K_S is negative as expected from the literature.

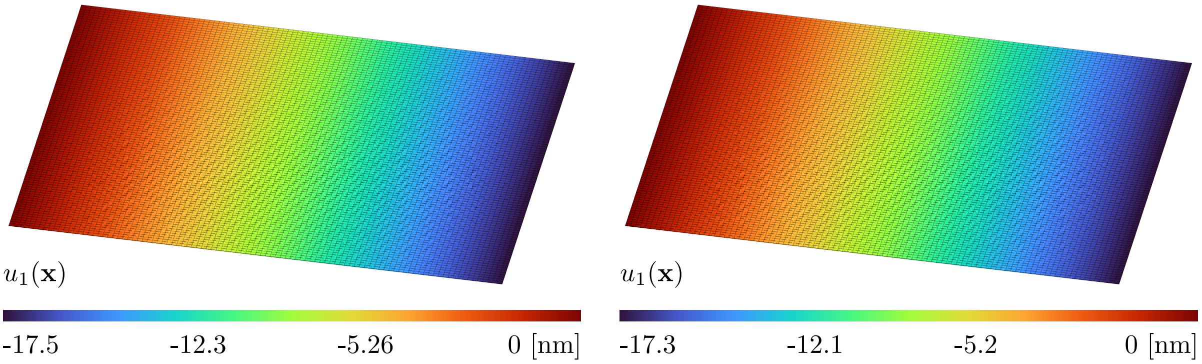

Figure 12: FEM solution for the nanoplate of $L = 10$ μm and $h = 10$ nm with surface tensions, using $\nu = 0.33$ and $E = 70$ GPa. The image on the left has been obtained with the parameters relative to Al [111] while setting the surface stiffness tensor to zero, leading to the analytical result (3.12). The image on the right has been obtained using Al [111] and taking into account the surface stiffness.

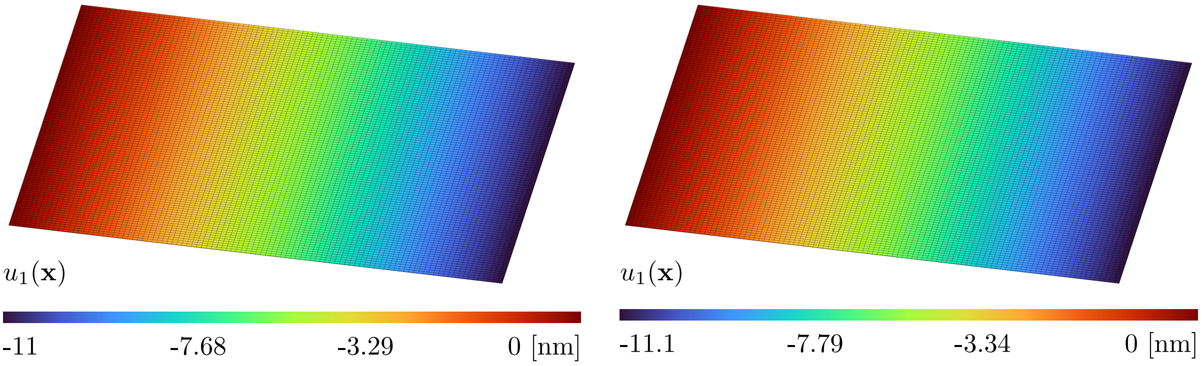

Figure 13: FEM solution u_x for the nanoplate of $L = 10$ μm and $h = 10$ nm with surface tensions, using $\nu = 0.33$ and $E = 70$ GPa. The image on the left has been obtained with the parameters relative to Al [100] while setting the surface stiffness tensor to zero, leading to the analytical result when taking the value of $\tau_0 = 0.569$ J/m^2 instead of the one relative to Al [111]. The image on the right has been obtained using Al [100] and taking into account the surface stiffness.

Furthermore, these results show the minor importance of surface tension and surface stiffness for our idealized nanoplate. Some insights on the importance of surface effects can be obtained by comparing the solution computed for different scales, and relate them to the surface-to-volume ratio (Figure 14). Clearly, the axial strain generated in a solid by surface tension seems to be negligible when $A/V < 1$ nm as the strain in the plate will be roughly less than 1 %. The change in the material overall stiffness due to the surface stress tensor is small when $A/V < 1$ nm and accounts for less than 7 % of the strain reduction for the Al [111]. It is important to note that high surface-to-volume ratio may be reached by materials displaying a high porosity and surface roughness, thereby the characteristic dimension of the material alone is not sufficient for characterizing the importance of surface effects.

3.3 Spherical Cavity

Analyzing 3D problems in an analytical way is much more difficult than 2D problems, thus the number of problems for which exact solutions can be obtained is very limited. For instance, the stress distribution of a two-dimensional plate with a circular cavity is determined only by its size and its boundary conditions, but in the case of a three-dimensional space, the stress field also depends on the Poisson's ratio of the object. For a spherical cavity existing in an infinite object under a uniform tensile stress, the non-zero components of the stress tensor on the surface of the cavity, including the maximum stress, has been computed in [28] and are given by the following equations:

$$\begin{aligned}\sigma_{\varphi\varphi} &= t_3\left[\frac{27-15\nu}{2(7-5\nu)} - \frac{15}{7-5\nu}\cos^2\theta\right]\\ \sigma_{\theta\theta} &= t_3\left[\frac{-3(1-5\nu)}{2(7-5\nu)} - \frac{15}{7-5\nu}\cos^2\theta\right]\end{aligned} \tag{3.15}$$

where t_3 is the non-zero component of the surface traction applied to the top and bottom faces of the domain. The resulting stress field is presented in Figure 15 for a cross section in the plane (y, z) as the solution is independent on φ. The stress tensor at the surface of the cavity in Cartesian coordinate is then obtained by applying the transformation tensor $\mathbf{R}$ to σ in spherical coordinates:

$$\mathbf{R} = \begin{bmatrix}\sin\theta\cos\theta & \cos\theta\cos\varphi & -\sin\varphi\\ \sin\theta\sin\varphi & \cos\theta\sin\varphi & \cos\varphi\\ \cos\theta & -\sin\theta & 0\end{bmatrix} \quad\Leftrightarrow\quad \sigma' = \mathbf{R}\sigma\mathbf{R}^\top \tag{3.16}$$

The finite element solution is presented in Figure 16, this latter is in good agreement with the analytical model. However, the analytical solution assumes an infinite domain while the finite element solution has been conducted on a finite domain twice larger than the cavity radius.

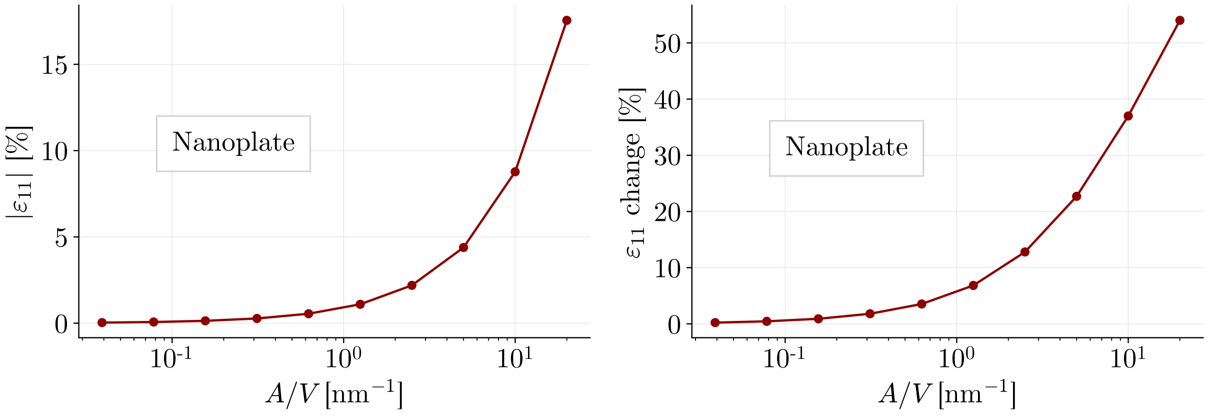

Figure 14: FEM solution for the Al [111] nanoplate as a function of the surface-to-volume ratio. The image on the left gives the strain due to surface tension when $\mathbf{K}_\mathrm{S} = 0$. The image on the right shows the relative change in strain between the case $\mathbf{K}_\mathrm{S} = 0$ and the case $\mathbf{K}_\mathrm{S} \neq 0$.

Secondly, it is important to note that the voxel-based shape of the mesh is not optimal, leading to geometrical singularities at the corner between two elements of the free surface. Thereby, the maximum stress in the domain, located at the geometrical singularities, does not converge to a finite value as the stress concentration at those points is theoretically infinite.

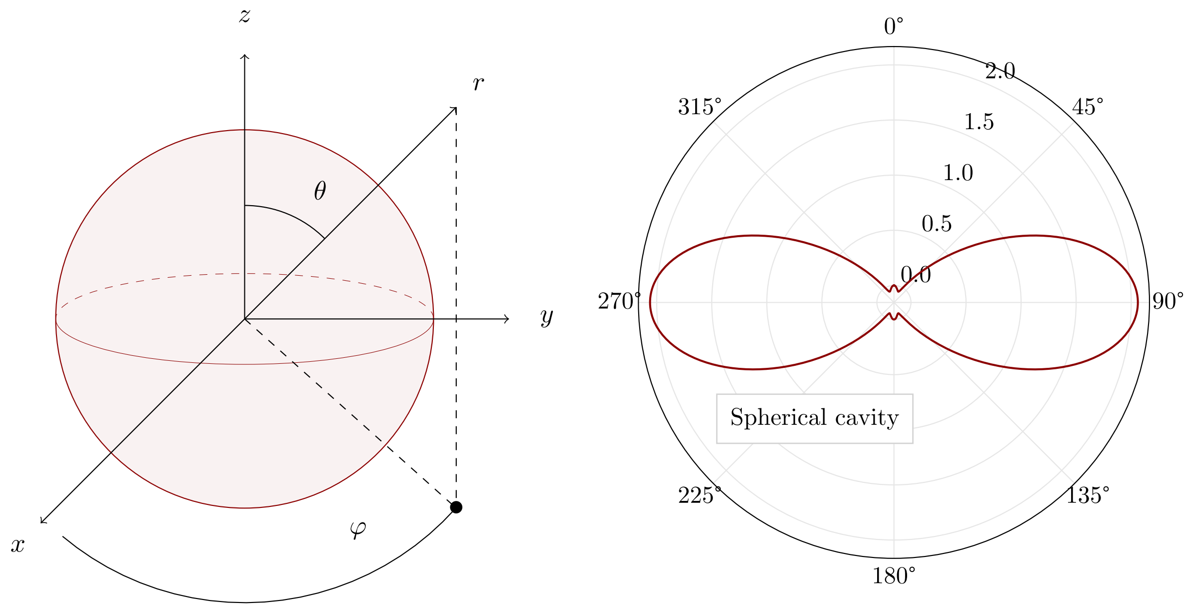

Figure 15: Axial stress field σ_{33} as a function of the angle θ at the surface of a spherical cavity of radius $r = 56$ nm in the (y, z) plane. The bulk domain of $E = 70$ GPa and $\nu = 0.33$ is submitted to an external stress $\mathbf{t} = [0\ 0\ 1]$ GPa applied at the top surface while the bottom surface is fixed along the z-axis.

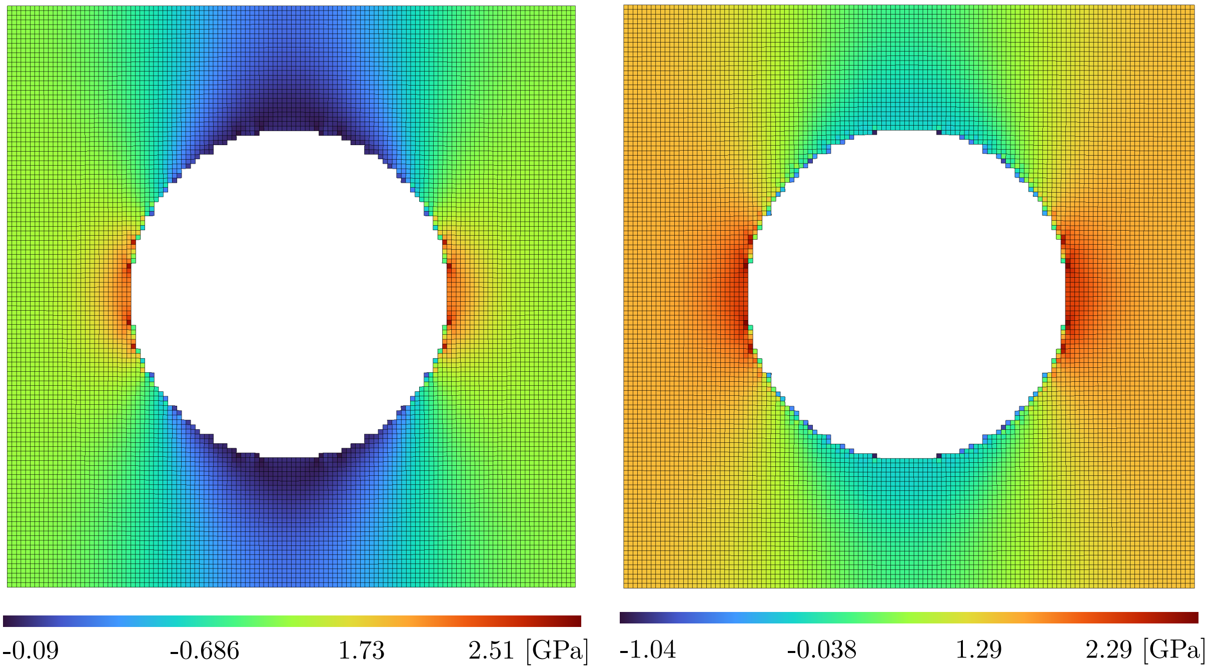

Figure 16: Middle cut along the (y, z) plane in the finite element solution σ_{33} for a spherical cavity of radius 56 nm in a 8×10^6 nm^3 block of aluminum under an external stress $\mathbf{t} = [0\ 0\ 1]$ GPa. The image on the left is the solution using LE and the image on the right is obtained with SET/SST using the surface stiffness and surface tension of Al [111] presented in Table 1 around the cavity.

This nonphysical behaviour deteriorates the quality of the approximation close to the singularities. Finally, as the surface tension tends to reduce the size of the free surface, and thus the size of the cavity, this latter acts against the applied external stress **t** and reduce the maximum stress in the structure. In this example, the surface stiffness increases the overall stiffness as the surface bulk modulus K_{S} of the Aluminum oriented at [111] is positive.

3.4 Conclusion

In this chapter, we presented different analytical solutions against which the numerical solutions obtained by our FEM code have been compared. We have shown that the numerical simulations correctly represent the relaxation of the nanostructure due to surface tensions as well as the stiffening or weakening of the overall material due to the surface elasticity. Moreover, we have shown that those effects are only relevant for some nanosized structures as surface effects becomes negligible compared to the bulk properties when the surface-to-volume ratio decreases. For instance, the nanoplate displays the following surface-to-volume ratio, which shows that the fraction of atoms located at the surface of the object increases as its characteristic size decreases:

$$\frac{A}{V} = \frac{2(L^2 + 2hL)}{L^2 h} = \frac{2(L+h)}{Lh} \tag{3.17}$$

Furthermore, we have shown that the FEM code is able to represent the nonlinear displacement of a cantilever beam using second-order Lagrange elements. In addition, the convergence of the numerical solution to the analytical solution has been verified by an iterative refinement of the mesh. In the last test case, a nanosized 3D structure under an externally applied stress field has been simulated with a spherical cavity and compared to the analytical predictions for the stress field around the cavity. Despite of the global agreement between the finite elements and the analytical solutions, we have shown that the use of a voxel-based mesh produces staircase artefacts which lead to an infinite stress concentration at the geometrical singularities. Thereby, the convergence of the stress at those points is not assessed. This information brings its importance in the next chapter where voxel-based meshes are used to compute the mechanical properties of thin films with a high level of porosity. Indeed, the use of isoparametric meshes is advised, but non-trivial to automatize when the structure displays 3D and complex random patters.

- **Limitations of the Code**

Before using the FEM algorithm for simulating thin films, it is important to summarise the assumptions considered and the limitations of the code. The SET/SST model presented in (2.14) and in the literature is based on the infinitesimal strain linear elasticity. This theory assumes that the reference configuration is similar to the deformed configuration, meaning that the strain generated by the applied load must be small. This assumption allows neglecting the quadratic terms in the strain tensor ε and the variation of the integration domain Ω with the displacement. The mechanical properties obtained with the FEM formulation (2.14) are thus the ones of the reference configuration and are independent of the strain. This behavior is not correct when the material is significantly deformed.

The SVK model does not suffer from this hypothesis. Indeed, the nonlinear terms of the strain tensor as well as the change of geometry are accounted. However, individual finite elements may enter in contact during the deformation due to the complex shape of highly porous films. This situation cannot yet be represented by the code as the algorithm is not able to manage friction and contacts between the mesh and itself. In order to prevent the different elements from interpenetrating, additional algorithms such as the penalty method or Lagrange multipliers must be implemented. A second limitation is the dependence of the boundary condition to the strain state. Indeed, the applied stress on the material must adapt to the deformation and internal rotations occurring at the surface of the film. For instance, when a finite element moves from the top surface to the interior under the action of the surface traction at the top of the structure, leading to additional nonlinear terms in the right-hand-side $\mathbf{F}_{\mathrm{T}}$ of the equation (6.30).

Finally, the SET/SST theory has been presented in the literature for small strain and has not yet been extended to large strain. Thereby, we will consider the SVK for the case of large strain, and use this algorithm to get an insight on the validity domain of SET/SST. Newton-Raphson iterative technique is a two-phases method used to find the root of a function or a linear system of equations. This method has the advantage of being simple to implement in multiple dimensions and large systems such as nonlinear FEM. However, its convergence to the actual solution is not guaranteed as the Newton-Raphson method converges to the closest local minimum, which may not be the global minimum. Thereby the starting point must be close enough to the solution in order to ensure convergence. Moreover, the method fails to represent inflexion points in the stress-strain relation. To overcome those issues, more elaborated methods such as the spherical arc-length or the normal plane arc-length may be implemented. With arc-length methods, the load-level parameter is no longer incremented by the user, but becomes a new unknown in the algorithm. Since a new unknown is introduced in the system, a new equation is required. The two latter methods allow the correct representation of inflexion points thanks to their adaptive increments (Figure 17).

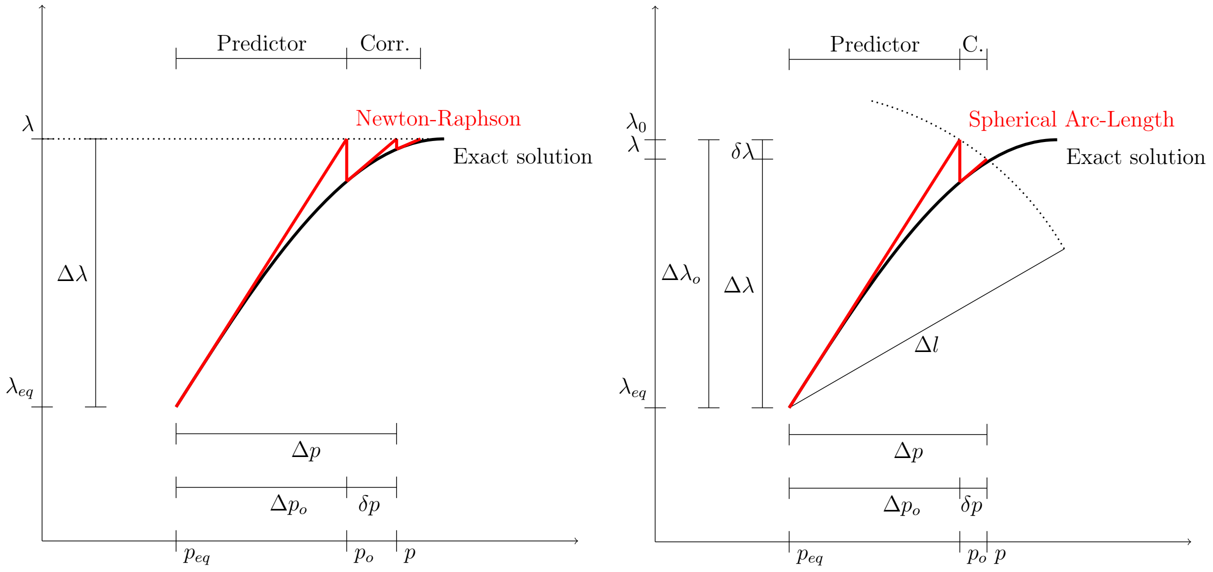

Figure 17: Example of Newton-Raphson and spherical arc-length iterative refinement of the solution in one dimension. λ is the load, $\Delta\lambda$ represents the load increment, $\delta\lambda$ is the corrected load increment by spherical arc-length, p is the displacement, Δp is the displacement increment and δp is the correction of the displacement during one step of Newton-Raphson or spherical arc-length algorithm.

Chapter 4

Applications on Thin Films

4.1 Introduction

This chapter is dedicated to the application of the FEM code developed in this work on different thin film structures: pure copper, zirconium and binary CuZr or Cu/Zr films. First, a review of the literature about the elastic properties of such thin films fabricated by physical vapor deposition is presented. Moreover, experimental measurements obtained at the Nuclear Reaction Analysis Research Unit (LARN) within the framework of Nanolaminates FNRS-PDR project are presented. The second step is the generation of the films with the use of SIMTRA and NASCAM. Replicas of the films obtained by the LARN are studied in addition to pure Cu, Zr and very porous Cu films. Once the thin film layer has been generated, the structure is converted into a FEM mesh and submitted to vertical compression tests. Finally, the last step is the comparison of our numerical results with experimental measurements.

4.2 Literature Review

An important step for the validation of numerical models is the comparison with results from the literature. This section provides a brief review of different papers concerning the mechanical properties of copper, zirconium and amorphous CuZr films obtained by experimental measurements. Like all materials, the structure of thin films is divided into amorphous and polycrystalline structure depending on the preparation conditions as well as the material nature. Deposition techniques may also be divided in two categories: physical and chemical depositions [29]. In the first category, one finds the magnetron sputtering (MS) and other physical vapor deposition techniques. Direct current magnetron sputtering (DCMS) uses a gaseous plasma, which is generated and confined into a vacuum chamber containing the material to be deposited, called the target (Figure 18). The electrons present in the gas are accelerated away from the cathode by causing collisions with nearby atoms of the gas, causing an ionization of this latter. The ions are then accelerated towards the negatively charged cathode. The collision of these energetic ions with the target ejects the metal atoms that are ultimately deposited on the substrate material, forming a metallic film. Similarly, the high-power impulse magnetron sputtering (HPIMS) uses an extremely high power density in short impulses, leading to a high degree of ionization of the sputtered metal, which result in a higher density of deposited films compared to conventional DCMS films [30].

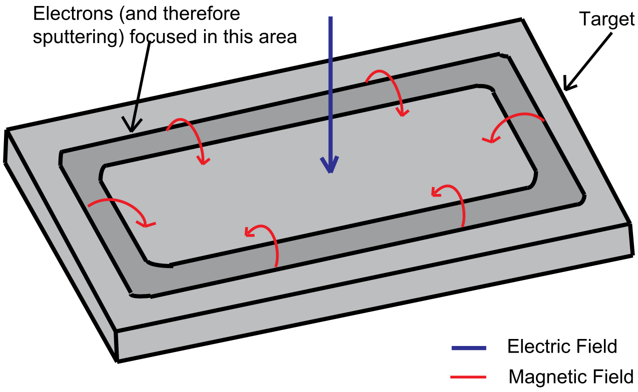

Figure 18: Illustrative example of magnetron target with a common rectangular geometry. Due to the magnetic field, the electrons are only trapped within a specific region of the target where most of the sputtering process occurs, leading to a distinctive racetrack region where the target is worn down. The target image is taken from here © University of Cambridge.

- **Copper Films**

Elastic properties of copper thin films fabricated by different deposition methods have been reported in [31] and summarized in Table 2. Clearly, these results demonstrated that films deposited using HPIMS assisted by an additional magnetic field exhibit significantly smoother surface, denser microstructure, higher hardness and Young's modulus than for the classical DCMS and HPIDMS due to the high energetic bombardment during the growing process and intense surface diffusion [31]. The reduced Young's modulus of the samples was estimated by nanoindentation (Figure 19). A nanoindentation test allows to measure the stiffness S of the contact between the indenter and the film, which can be used to calculate the reduced Young's modulus, this latter can be related to the Young's modulus by

Table 2: Values of reduced Young's modulus E_r measured by nanoindentation and absolute Young's modulus E obtained by different equations, for a copper thin films of thickness 800 nm with a silicon substrate. HPIMS* denotes the HPIMS with an additional magnetic field [31].

Deposition	E_r [GPa]	E (4.1) [GPa]	E (4.2) [GPa]	E (4.3) [GPa]
DCMS	117.9 ± 6.4	119.6	102.2	78.9
HPIMS	126.6 ± 7.4	129.5	109.7	85.2
HPIMS*	142.6 ± 8.6	148.2	128.4	98.5

$$\begin{aligned} \frac{1}{E_r} &= \frac{1}{E'} + \frac{1-\nu^2}{E_i} \\ E' &= \frac{E}{1-\nu^2} + \left(\frac{E_s}{1-\nu^2} - \frac{E}{1-\nu^2} \right) \frac{h}{t} \end{aligned} \tag{4.1}$$

where E_r is the reduced Young's modulus, E_s and ν_s are the Young's modulus and Poisson's ratio of the substrate, E and ν are the Young's modulus and Poisson's ratio of the specimen and E_i is the Young's modulus of the indenter, h is the indentation depth and t is the total thickness of the film [32]. Additional studies investigated the mechanical and structural properties of Cu thin films of 800 nm in thickness, deposited by DCMS and HPIMS operated with single ultra-short pulses, with and without additional magnetic field on a silicon substrate [31]. A second way to estimate the Young's modulus of the sample is by using the maximum load divided by the contact stiffness:

$$\begin{aligned} \frac{4}{\pi} \frac{P_{\mathrm{max}}}{S^2} &= \frac{H}{E^2} \\ H &= \frac{\kappa P_{\mathrm{max}}^3}{9 W_{\mathrm{p}} 2} \end{aligned} \tag{4.2}$$

where $\kappa = 0.0408$ for a three-sided diamond Berkovich indenter, P_{max} is the maximum applied load W_{p} is the plastic work given by the area encompassed between the loading and unloading curves [32]. Finally, a third method for estimating E is the use of the work of indentation method

$$\frac{W_{\mathrm{tot}} - W_{\mathrm{e}}}{W_{\mathrm{tot}}} = 1 - \frac{5H}{E} \tag{4.3}$$

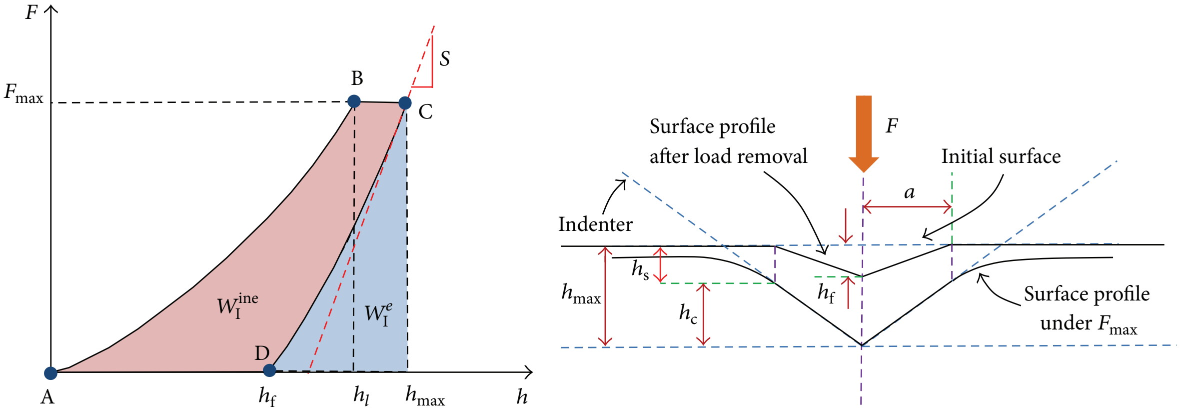

Figure 19: Schematic representation of load-displacement curve (where F is the applied force and h the indentation depth) in nanoindentation testing on the left. Schematic representation of cross-section through the indentation of a material sample on the right. Image taken from [33].

where W_{tot} is the total work of indentation given by the area under the loading curve, and W_{e} is the elastic work given by the area under the unloading curve [32]. The increase of Young's modulus for HPIMS methods can be partially explained by a reduction of the surface roughness which influences the measurement by nanoindentation process.

- **Zirconium Films**

Amorphous CuZr metallic glass thin films have been studied in [34] for various concentrations of copper. In particular, we are interested in the elastic properties of the film in the case of a pure Zr sample, as the influence of the Cu concentration will be discussed in a further paragraph. The films have been deposited by a magnetron dual cathode (DC) physical vapor deposition process at 0.5 Pa, this technique allows an easy control of the composition of the sample by varying the relative intensities applied to both pure Cu and Zr targets. The Young's modulus of the pure Zr sample was measured at 102 ± 8 GPa by nanoindentation experiments. A similar study has been conducted in [35] on CuZr samples with a thickness of about 5 μm in dual cathodes at a deposition pressure of 0.355 Pa, the results are presented in Figure 20. It can be observed that the Young's modulus changes between amorphous and partially or totally crystalline structures, a hypothesis given in [35] concerning the cause of this behaviour is the combined effect of solid solution and grain size refinement. However, the increase of E with the Cu content in the amorphous region may be explained by the global reduction of the interatomic distance as well as an increase of the strength of the chemical bonds. Indeed, if one assumes that

$$E = kr\frac{\partial}{\partial r}\left(\frac{1}{r^2}\frac{\partial U}{\partial r}\right) \tag{4.4}$$

where U is the interatomic potential, r the interatomic distance and k is a constant parameter [36], it is evident that small interatomic distances lead to a higher Young's modulus. In the particular case of an almost-pure Zirconium thin film, the Young's modulus is estimated at 107 ± 10 GPa. As a comparison with macroscopic materials, the Young's modulus of bulk zirconium is referred as 94.5 GPa in [37] and 98 GPa in [38], which means that a reduction in size may improve the stiffness of the Zr material. Additional results reported in [39] are presented in Table 3, where the mechanical properties of Cu, Zr, CuZr and multilayer CuZr/Zr glass coatings have been measured by nanoindentation technique.

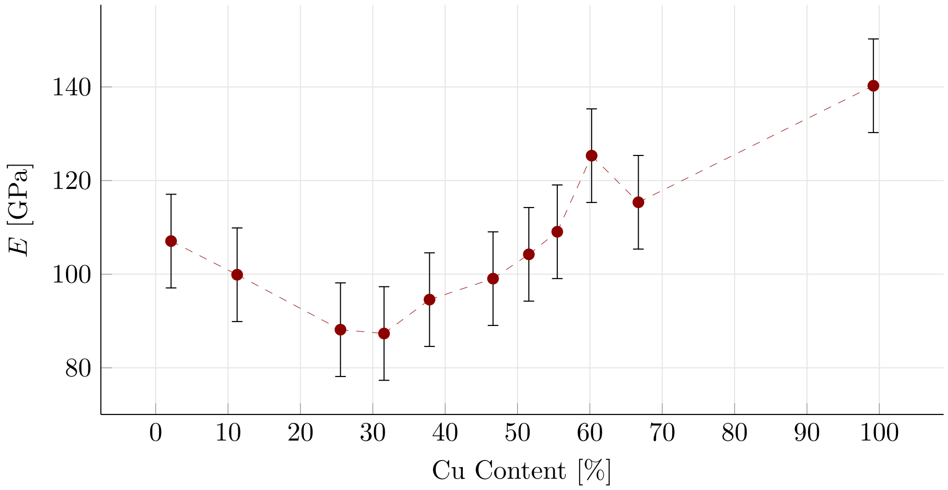

Figure 20: Young's modulus in compression of binary CuZr thin films as a function of the concentration of copper in the material. The amorphous configurations are roughly obtained between 25 and 75 % of copper. The graph is reproduced from [35] with permission from Elsevier.

Table 3: Experimental Young's modulus in compression of Cu, Zr, $Cu_{45}Zr_{55}$ monolayer thin films and $Cu_{45}Zr_{55}/Zr$ multilayer thin films deposited by DCMS. The parameter h gives the average thickness of each individual layer in nm. The results reported here are obtained from [39].

Paper	Material	h [nm]	Thickness [μm]	E [GPa]	Error [GPa]
[39]	Cu	–	1	111.6	5.8
	Zr	–	1	120.6	2.9
	CuZr	–	1	104.3	1.2
	CuZr/Zr	95	1	109.4	1.9
	CuZr/Zr	40	1	102.6	1.2
	CuZr/Zr	9	1	100.1	1

- **Binary CuZr Films**

It can be seen that most of the Zr-based binary films have a Young's modulus between 95 and 118 GPa. As stated in [35], this value tends to increase with the Cu content in the case of an amorphous film. A study in [40] produced thin film and ribbon of two compositions of CuZr metallic glass. The values of elastic modulus for $Cu_{50}Zr_{50}$ are 88.5 and 109.5 GPa, while for $Cu_{64}Zr_{36}$ samples, the values are measured at 106.7 and 114.3 GPa for ribbon and thin films respectively. The result is contradictory with the expectations as thin film metal glasses should contain more free volume than ribbons and thus, should display a lower elastic modulus. This may be explained by a different arrangement of atoms and molecules in the solid. A second study conducted on metallic glass coating from the binary ZrCu system using a physical vapor deposition process [34] also reported an increase of the Young's modulus with the content of Cu (Figure 21). This latter has been measured by nanoindentation, however, the variation of E is globally less significant than the one reported in [35]. A summary of different results from the literature is presented in Table 4. Multilayered ZrCu/Cu thin films were fabricated and tested in [41] for different layer thickness, the results are presented in Table 5. It is important to note that the mechanical properties have been evaluated by a tensile test.

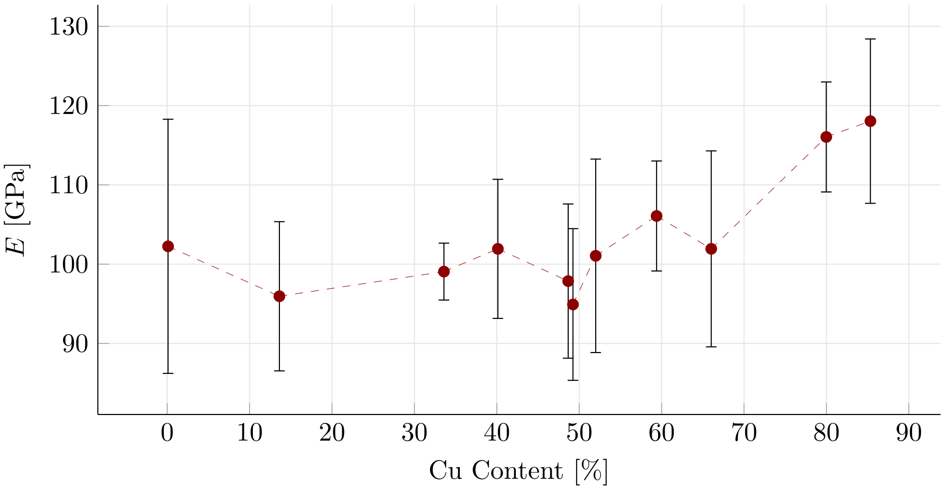

Figure 21: Young's modulus in compression of binary CuZr thin films of 5 μm thickness deposited by DCMS at 0.5 Pa for different concentration of copper. An amorphous material is obtained in the region between 30 and 90 % of Cu content. Adapted from [34] with permission from Elsevier

Table 4: Summary of atomic density of copper, Young's modulus in compression of the film with an estimation of the measurement errors, thickness of the film, deposition process and pressure conditions for different amorphous CuZr composites obtained in the literature.

Paper	Process	P [Pa]	Thickness [μm]	Cu [%]	E [GPa]	Error [GPa]
[34]	DCMS	0.5	6.2	33.3	99	3.6
	DCMS	0.5	5.8	40.1	102	8.8
	DCMS	0.5	4.3	48.9	95	9.7
	DCMS	0.5	4.4	51.7	101	12.2
	DCMS	0.5	4	59.1	106	6.9
	DCMS	0.5	4.4	65.9	102	12.4
[40]	DCMS	$0.3 \sim 0.8$	$3 \sim 4$	50	109	1.6
	DCMS	$0.3 \sim 0.8$	$3 \sim 4$	64	114	2.2
[35]	DCMS	0.355	5	25.6	88	10
	DCMS	0.355	5	31.6	87	10
	DCMS	0.355	5	37.9	94	10
	DCMS	0.355	5	46.6	99	10
	DCMS	0.355	5	51.5	104	10
	DCMS	0.355	5	55.5	109	10
	DCMS	0.355	5	60	125	10
	DCMS	0.355	5	66.6	115	10
[42]	DCMS	0.533	2	31	100	–
	DCMS	0.533	2	40	105	–
	DCMS	0.533	2	46	107	–
	DCMS	0.533	2	51	110	–
	DCMS	0.533	2	55	114	–
	DCMS	0.533	2	62	118	–

Table 5: Experimental Young's modulus in compression of $Zr_{50}Cu_{50}$/Cu multilayer films (MLTF) and monolithic CuZr film (TFMG) as a function of the thickness h of the layers composing the film. The films were deposited on a 10 μm thick Cu foils using DCMS [41].

Paper	Type	h [nm]	Thickness [μm]	E [GPa]	Error [GPa]
[41]	TFMG	–	1	99	–
	MLTF	10	1	96	19
	MLTF	25	1	91	17
	MLTF	50	1	84	17
	MLTF	100	1	111	7
	MLTF	150	1	96	1

Table 6: Young's modulus in compression of Cu/Zr multilayer and monolithic films for different compositions deposited by DC magnetron sputtering. The parameter h denotes the thickness of each layer composing the film. Cu_xZr_y is an amorphous material containing x % copper and y % zirconium.

Source	Material	Name	h [nm]	Thickness [nm]	E [GPa]	Error [GPa]
LARN	Cu	`20112403`	–	–	148.2	13
	$Cu_{60}Zr_{40}$	`19052802`	–	594	111.6	6.2
	$Cu_{40}Zr_{60}$	`19052803`	–	425	88.1	5.1
	Cu/Zr	`20112501`	11.6	465	135.15	15.5
	$Cu_{60}Zr_{40}$ / $Cu_{40}Zr_{60}$	`20112602`	223	446	148	25
			154	616	151	23
			63	630	128	20
			38	760	144	23
			20	800	140	11.1
			19	950	148	19
			10	800	136	9.5

- **LARN Measurements**

Zirconium and copper sputtering targets with 99.9 % purity have been used for thin film deposition by the LARN. The thin films were fabricated by magnetron sputtering at 0.67 Pa either in single-cathode (SC) and dual-cathode (DC) mode using a semi-industrial chamber of about one cubic meter of D&M vacuum system (Figure 23). The film is deposited on a silicon or stainless steel substrate. Finally, the target-substrate distance was kept between 13 and 42 cm and each target was pre-sputtered for removing any surface impurities. It has been reported that $Cu_{60}Zr_{40}$ and $Cu_{40}Zr_{60}$ are fully amorphous thin films due to absence of crystalline pattern, while Cu/Zr films display fully crystalline Zr layers with an amorphous line where the CuZr composition is growth. The resulting measurements of Young's modulus by nanoindentation are presented in Table 6. E measured by the LARN is the instrumental elastic modulus estimated from the reduced Young's modulus by

$$\frac{1}{E_r} = \frac{1-\nu^2}{E} + \frac{1-\nu_i^2}{E_i} \tag{4.5}$$

4.3 Simulation of the Film

3

Simulation of atomic flux during magnetron sputtering process.

The software used to simulate the metal flux during the magnetron sputtering is the Monte-Carlo code SIMTRA. The particles are generated with initial position, energy and direction from a target surface, then their movement is tracked until they cross a physical surface. A flow chart describing the main steps of the code is presented in Figure 22. The initial energy probability density function $\bar{\rho}_{\mathrm{E}}$ of the sputtered atoms can be simulated using SRIM or a Thompson distribution [43]. In this work, the latter was used to simulate the Cu and Zr depositions on the substrate:

$$\bar{\rho}_{\mathrm{E}}(E)\,dE = E\big(E + U_{\mathrm{S}}\big)^{2m-3}\,dE \tag{4.6}$$

where U_{S} is the surface binding energy. For magnetron sputtering, the ion energy is low and the value of m is set equal to zero [43]. Finally, the initial angular probability density function $\bar{\rho}_{\mathrm{A}}$ is described by the built-in function with its default parameters ($c_1 = 1$ and $c_j = 0$ for $j \neq 1$).

$$\bar{\rho}_{\mathrm{A}}(\cos\theta) = \sum_{j=0}^{5} c_j(\cos\theta)^j \tag{4.7}$$

The sputtering process takes place in the D&M coater presented in Figure 23, the vacuum chamber contains an argon gas at 0.67 Pa. Once the simulation of the particle flux is completed, the output data from SIMTRA are post-processed to estimate analytical expressions for the energy and angular distributions of the incident particles on the substrate. This may be achieved by a simple polynomial regression if E and θ are the unique variables of the problem. If other parameters are considered, more advanced techniques such as the polynomial chaos expansion (PCE) allow obtaining an accurate surrogate model. The energy distribution is the function ρ_{E} defining the probability density function of a sputtered particle having particular energy E while reaching the substrate in an argon gas of pressure P. The angular distribution ρ_{A} defines the probability density function of a sputtered particle reaching the substrate with an angle θ in an argon gas of pressure P. The number of particles N in the given direction (θ, φ) obtained by SIMTRA is proportional to

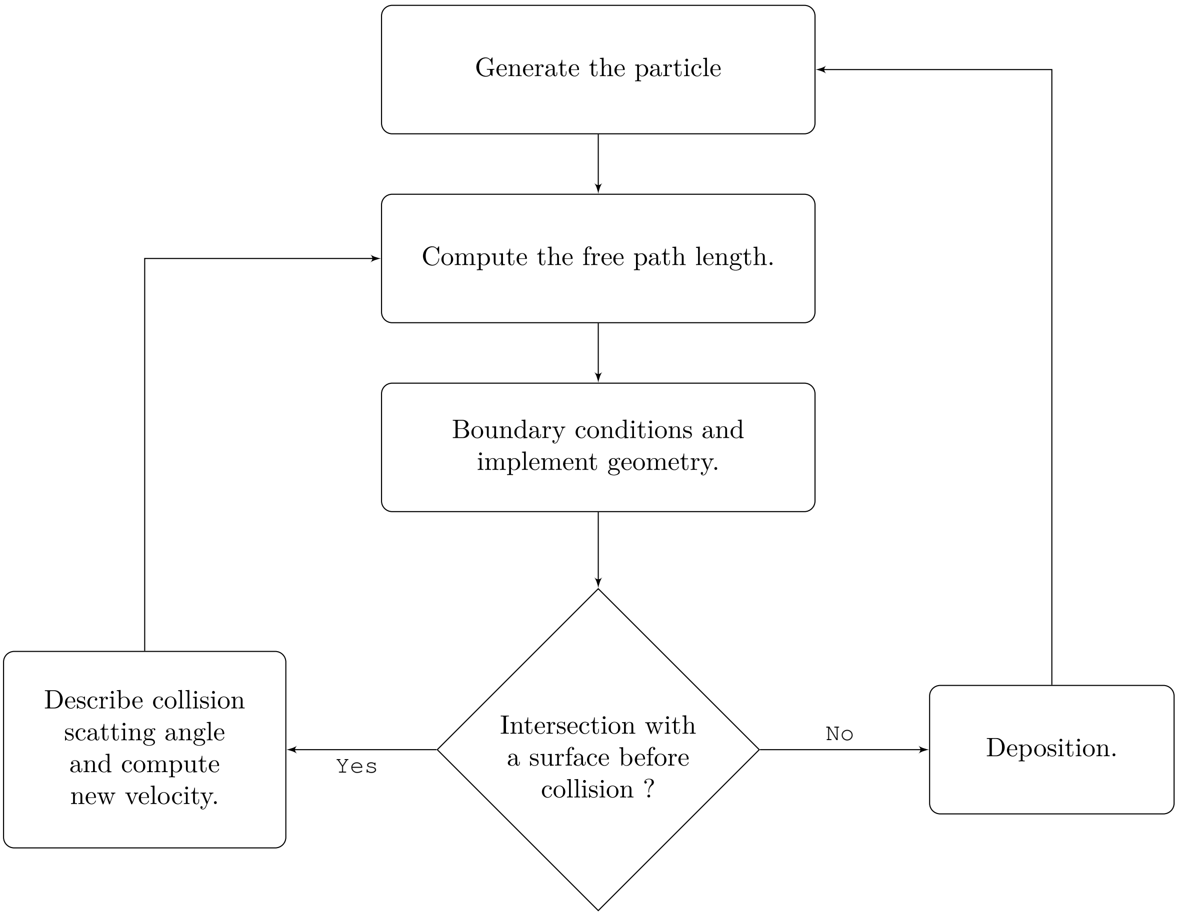

Figure 22: Flow chart showing the important step in the calculation of a deposition profile, energy and angular distributions on a substrate by magnetron sputtering, with the Monte Carlo model used in SIMTRA. The flow chart is reproduced from [43].

$$dN(\theta, \varphi) = \rho(\theta, \varphi) \sin(\theta)\, d\theta\, d\varphi \tag{4.8}$$

and the density of particles is given by $dN/\sin\theta$. In order to improve the analytical approximation, it is important to note that the pressure and energy dependencies of the distributions are exponential, which are not easily represented by a series of polynomials. Performing the change of variables

$$\begin{cases} P \rightarrow q \text{ with } q = \ln P \\ E \rightarrow \varepsilon \text{ with } \varepsilon = \ln E \end{cases} \Leftrightarrow \begin{cases} \rho_{\mathrm{E}}(P, E) \rightarrow \rho_{\mathrm{E}}(q, \varepsilon) \\ \rho_{\mathrm{A}}(P, \theta) \rightarrow \rho_{\mathrm{A}}(q, \theta) \end{cases} \tag{4.9}$$

allows the work with new functions whose behaviors are close to a polynomial, thus allowing to provide an accurate surrogate model while keeping the order of the polynomials at an acceptable level. An example of results is presented for a particular pressure in the Annex 6.5.

- **NASCAM Simulation**

4

Generation of the thin films structure on a substrate.

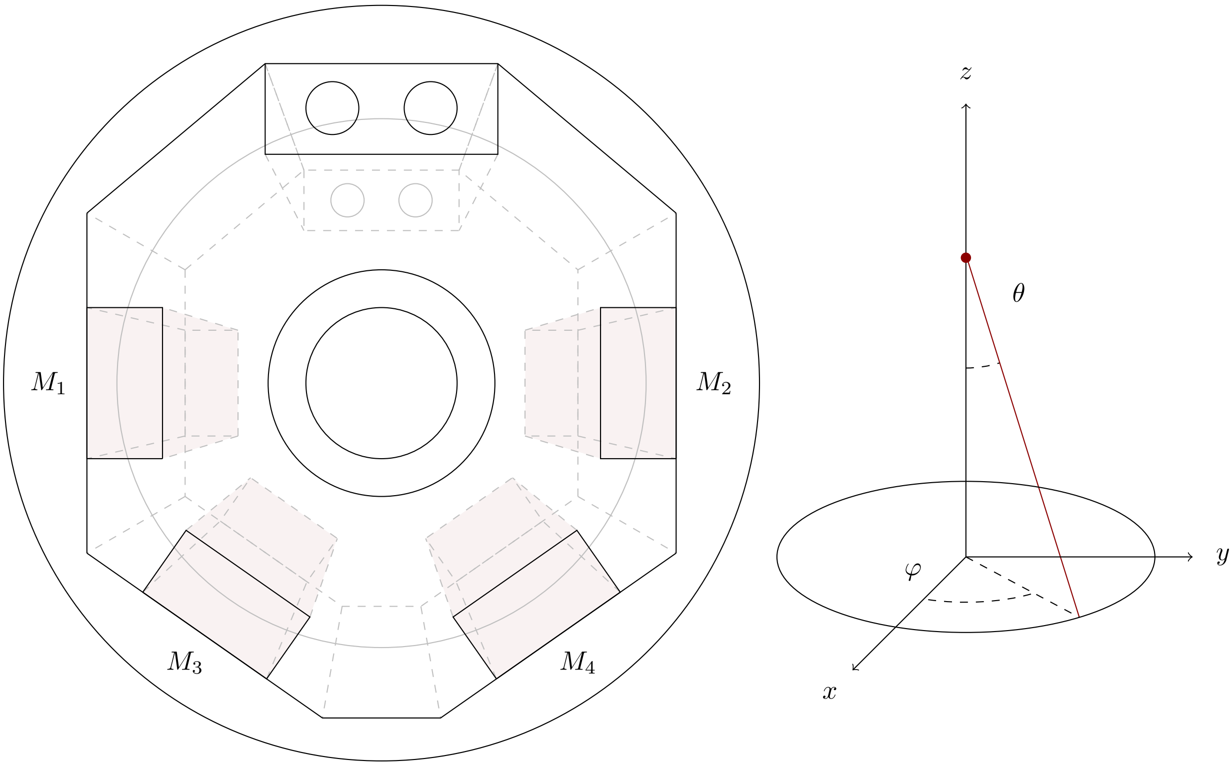

Figure 23: Schematic of the D&M coater used for the deposition, the magnetrons are noted M. In the SC mode, the substrate of 2×2 cm^2 is placed perpendicular to M_2 at 8 cm from the target, with the other magnetrons deactivated. In the DC mode, the substrate is placed horizontally between M_3 and M_4 at the same distance from the middle plane joining the center of the two targets, with the other magnetrons deactivated. The image on the right represents the angle of a particle with respect to the place of the substrate, the angular distribution is the distribution of the particle angle θ while reaching the substrate for all value of the φ.

Table 7: Characteristics and name of the different thin film samples generated by NASCAM using the energy and angular distributions obtained from SIMTRA in Annex 6.5. The composite sample is $Cu_{50}Zr_{50}$ and ADC means that the film has been generated in dual cathode mode, but by alternating between the left and right cathodes for sputtering the Cu and Zr layers, one at a time.

Sample	Method	Composition	Porosity [%]	h [nm]	Thickness [nm]
$\mathbf{A}_1$	–	Cu	~ 0	–	64
$\mathbf{A}_2$	–	Cu	50	–	44
$\mathbf{A}_3$	DC	Cu	14	–	25
B	DC	Zr	12	–	32
C	DC	CuZr	14	–	49
$\mathbf{D}_1$	SC	Cu/Zr	20	11	430
$\mathbf{D}_2$	ADC	Cu/Zr	30	12	489

To simulate the time evolution of atoms deposited on the substrate, the software NASCAM, developed by the LARN is used. This software uses the so-called specific kinetic Monte Carlo event approach, where only a predefined set of events is allowed to occur during the growth of the film, and the rates of these events are used as an input. NASCAM is equipped of different plugins allowing to perform multiple pre- or post-processing of the thin film. In particular, the mechanical FEM plugging was implemented in this work. In NASCAM, the angular and energy distributions obtained by SIMTRA are given as input data to the code. The incident energy is taken from the energy distribution of the incident atoms and the impact parameter is calculated taking into account the trajectory of the projectile and the initial position of the target. The energy of an incident atom is then selected stochastically in accordance with its energy distribution. If X is a continuous uniform random variable in the sample space $\Omega \in [0, 1]$ and $\bar{x}$ is a realization of this random variable, the energy E of an incident atom is computed by

$$\bar{x} = \int_0^E \rho_{\mathrm{E}}(x)\,dx \left(\int_0^\infty \rho_{\mathrm{E}}(x)\,dx\right)^{-1} \tag{4.10}$$

Similarly to the literature review, copper, zirconium, CuZr and multilayered Cu/Zr films have been generated by NASCAM and their elastic properties are studied. These samples are named by a letter and their topological characteristics are presented in Table 7.

- **Generation of the Mesh**

A layer is defined as the structure obtained by a single sputtering process, and composed of a single chemical species (Cu or Zr) or molecule (CuZr). The output file from NASCAM contains a list of atoms with their coordinates, the index of the layer and the filling fraction. This last parameter gives the volume fraction of the atom in their corresponding finite element. The mesh is a parallelepiped domain subdivided into equally sized Lagrange hexahedrons. When the total filling fraction of the j-th element f_j is such that $f_j > f_{\mathrm{M}}$, this latter is considered as composed of the most prominent component. Conversely, the element is considered as a pore if $f_j < f_{\mathrm{M}}$.

5

Application of the code to thin films and comparison with literature.

Table 8: Table of bulk parameters for the FEM code. The elastic properties of pure bulk copper and zirconium are retrieved from [37], the lattice constant and elastic properties of the binary CuZr alloy have been obtained by molecular dynamics simulations in [44].

Material	E [GPa]	ν [-]	λ [GPa]	μ [GPa]	a [nm]
Cu	130	0.34	103	48.5	0.36
Zr	94.5	0.34	74.9	35.2	0.51
CuZr	127.4	0.3	73.5	49	0.319
Cu/Zr	130/94.5	0.34	103/74.9	48.5/35.2	0.34

Table 9: Values of the surface tension as well as the first and second Lamé surface parameters for an isotropic surface [111] of copper. Those results have been obtained with the embedded atom method and reported for relaxed and unrelaxed surfaces in [45][46]. It is important to note that the additional relaxations of atoms at the crystal surface due to strain has a profound effect on the results.

Cu [111]	λ_s [J/m^2]	μ_s [J/m^2]	τ_0 [J/m^2]	K_s [J/m^2]
[45] Relaxed	-2.243	0.144	1.241	-1.955
[45] Unrelaxed	-4.646	-1.265	1.241	-7.158
[46] Relaxed	1.49	-1.06	1.12	-0.63
[46] Unrelaxed	1.2	-1.21	1.13	-1.22

4.4 Numerical Results

In this section, the elastic properties of the different representative elementary volumes of thin films presented in Table 7 are evaluated in compression. In the following simulations, the finite elements composed of copper and zirconium have the mechanical properties of bulk Cu and Zr with Young's modulus and Poisson's ratio retrieved from [37] and presented in Table 8. For the monolithic CuZr film, copper and zirconium atoms are assigned to the same layer in NASCAM and must share the mechanical properties of the CuZr alloy, these properties have been estimated by molecular dynamics in [44]. Finally, the lattice constant of the CuZr structure is given by $a = 0.319$ nm. The multilayered Cu/Zr films being composed of pure Cu and Zr layers, each layer displays the properties of its respective chemical component. However, the lattice constant of the whole structure is fixed to $a = 0.34$ nm. The surface Lamé parameters for an isotropic copper surface are given in Table 9. An important remark is that different papers report different values for the surface parameters of copper. Consequently, these results may lead to qualitative conclusions rather than precise numerical results [46]. For all samples, the material is assumed to be at equilibrium so that the residual stresses due to surface tension are zero. The external stress is applied at the top surface of the sample along the z-axis, the top surface as well as the substrate are forced to remain flat during the deformation, the overall Young's modulus E along the z-axis is simply obtained by

$$\begin{aligned} \varepsilon_{33} &= (L - \Delta L)/L \\ E &= \sigma_{33}/\varepsilon_{33} \end{aligned} \tag{4.11}$$

where σ_{33} is the applied stress at the top surface, L is the initial thickness of the sample, ΔL is the vertical displacement of the top surface and ε_{33} is the global strain of the material along the z-direction. Two cases of Dirichlet conditions are studied:

The first case where an overall transverse strain of the film is prevented, and the second case where an overall transverse a strain is allowed. Indeed, an important consideration is the influence of the substrate on the film properties. In our samples, only some atoms of the substrate in contact with the film are represented, meaning that the substrate has q very weak influence on the measured quantities by the FEM code. It is thus interesting to study a second case where the substrate is much stiffer than the film and prevents transverse strain.

- **Samples $\mathbf{A_1}$ and $\mathbf{A_2}$**

Those two first samples have not been generated by the distributions in Annex 6.5 but aim at studying the influence of the pore structure on the mechanical response of the film as well as the influence of surface stiffness. An overview of the porosity of the sample $\mathbf{A}_2$ is presented in Figure 24. This particular configuration has a significant influence on the mechanical response of the structure, as it will be demonstrated later. In order to complete the description of the material porosity, the normalized density of $\mathbf{A}_1$ and $\mathbf{A}_2$ is presented in Figures 25 as a function of the deposition time. The film porosity is thus obtained by $p = 1 - \rho/\rho_0$ at the end of the simulation. Clearly, the sample $\mathbf{A}_1$ is expected to display a Young's modulus close to the bulk material if the substrate is not taken into account, as its surface-to-volume ratio is close to $A/V = 1.5 \times 10^{-2}$ nm^{-1}, which lies in the region of negligible surface effects according to Figure 14. The sample $\mathbf{A}_2$ is expected to display a Young's modulus significantly smaller than its bulk counterpart due to its high porosity, but also due to its internal structure. Indeed, the rule of mixtures [47] states that

$$f = \frac{V_1}{V_1 + V_2} \quad \Leftrightarrow \quad \begin{cases} E_{\mathrm{U}} = fE_1 + (1-f)E_2 \\ E_{\mathrm{L}} = f\left(\dfrac{f}{E_1} + \dfrac{1-f}{E_2}\right)^{-1} \end{cases} \tag{4.12}$$

where E_1 and V_1 are the Young's modulus and volume of the first material and E_2 and V_2 are the Young's modulus and volume of the second material in the composite. E_{U} is the upper bound of the Young's modulus in the direction parallel to the fibers and E_{L} is the lower bound of the Young's modulus in the direction perpendicular to the fibers, which tends to zero when the Young's modulus of one material (namely, the pores) tends to zero.

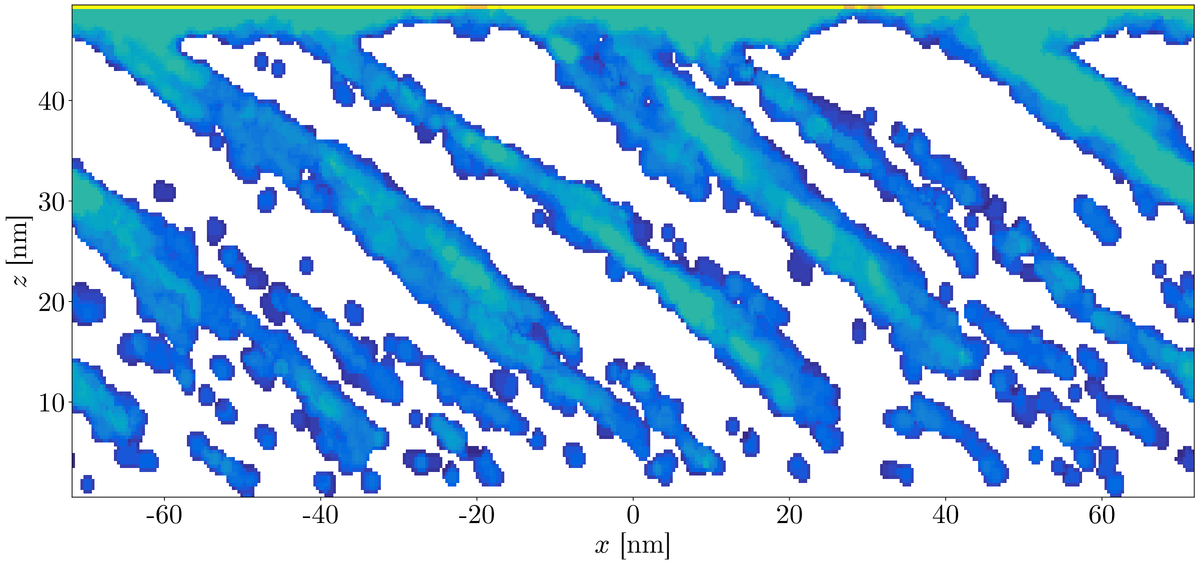

Figure 24: Structural porosity of the copper thin film $\mathbf{A}_2$. The colored dots feature the presence of an empty space in the film while the colour tone represents the pore concentration in the y-dimension. Deep blue indicates that the pore has a small extent in the y-dimension and yellow indicates that the pore has an extent over the total depth of the film.

For a same porosity, the orientation of the slats in Figure 24 will influence the overall Young's modulus. The von Mises stress (4.13) in the sample $\mathbf{A}_2$ with the SET/SST is presented in Figure 26. This measure may be used to assess the validity of the elastic behaviour of the material using the von Mises criteria, where σ_{VM} is compared to the yield stress. As expected, σ_{VM} reaches a very high value at some precise location in the structure, where a few finite elements are connecting different pores. It is clear that plasticity, caused by a breaking and a reforming of bonds between chemical elements, will occur at those locations first. The Young's moduli of both samples are presented in Table 10. As expected, the sample $\mathbf{A}_1$ displays the modulus of the bulk material. Moreover, it can be observed that the influence of surface effect is negligible for $\mathbf{A}_1$. The sample $\mathbf{A}_2$ displays an increased dependency in the surface stiffness compared to $\mathbf{A}_1$ due to the increased surface-to-volume ratio generated by the porosity.

$$\sigma_{\text{VM}} = \sqrt{\frac{1}{2}\left[\left(\sigma_{11}-\sigma_{22}\right)^2 + \left(\sigma_{22}-\sigma_{33}\right)^2 + \left(\sigma_{33}-\sigma_{11}\right)^2\right] + 3\left(\sigma_{12}^2+\sigma_{23}^2+\sigma_{31}^2\right)} \tag{4.13}$$

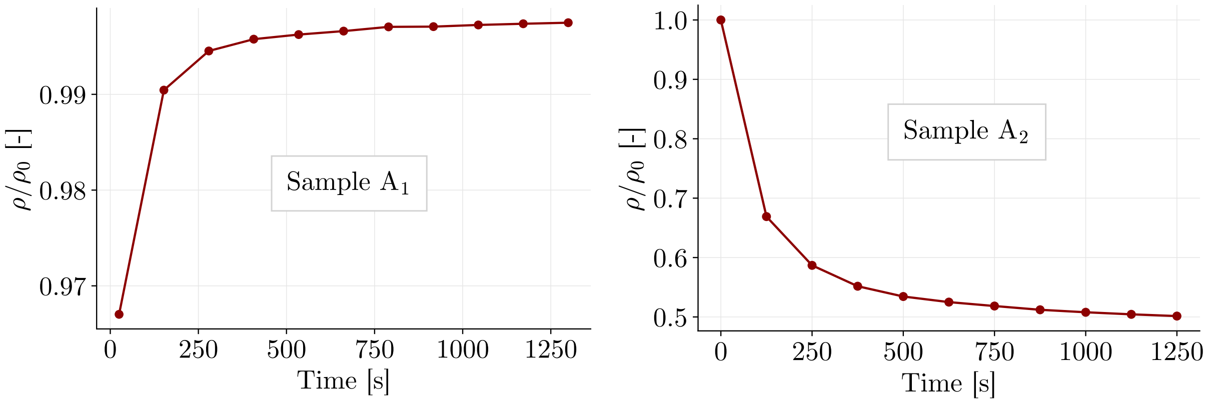

Figure 25: Normalized density of the films as a function of the simulation time of the deposition process. The graph on the left features the sample $\mathbf{A}_1$ displaying a low porosity, the image on the right features the sample $\mathbf{A}_2$ displaying a high porosity as shown in Figure 24.

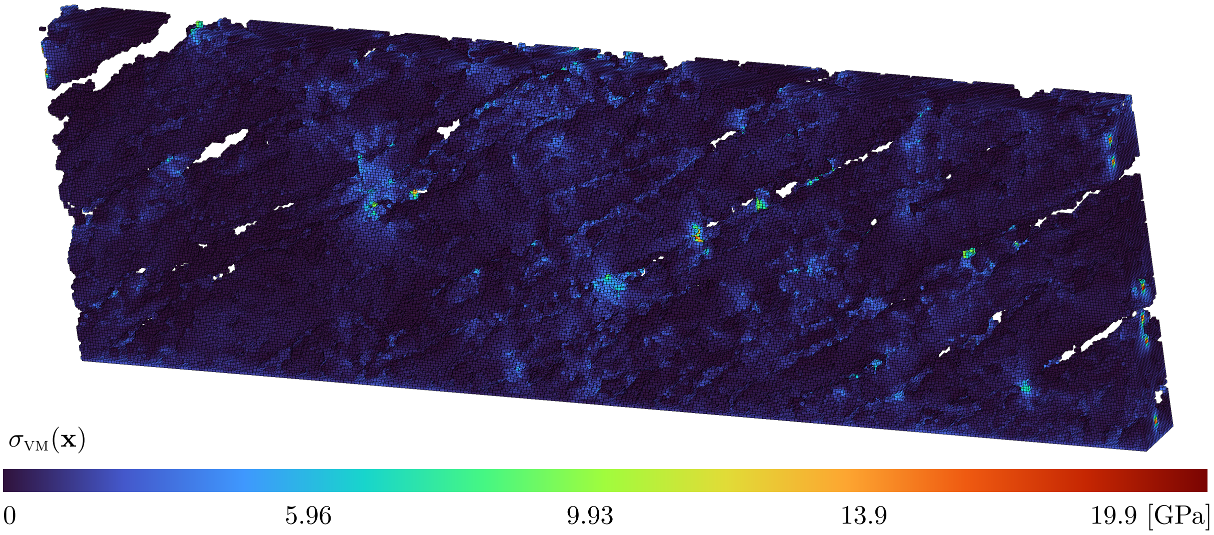

Figure 26: Von Mises stresses averaged over each finite element for the sample $\mathbf{A}_2$ under a compressive load of 0.1 GPa at the top surface. The sample is assumed to be at equilibrium such that there is no residual stress $\mathbf{F}_{\text{S}} = 0$. The SET/SST Algorithm 5 with relaxed surface elasticity (first line in Table 9) have been used. Finally, the overall transverse strain of the material is prevented.

The dependence of the Young's modulus in vertical compression on the angle of the slats in the sample $\mathbf{A}_2$ can be understood by the torque generated at the base of the slat due to the applied vertical stress, leading to high stress concentration. For instance, one may simulate different nanostructures of 50 % porosity, displaying copper slats of different angles with respect to the horizontal plane as shown in Figure 27, and compare their overall Young's modulus. Clearly, it can be observed that decreasing the angle of the slats decreases the overall Young's modulus of the structure.

Once the elastic properties in vertical compression of the films has been computed under the small strain assumptions, it is important to get insights on the validity domain of the solution. Indeed, the obtained values of E are instantaneous values of the undeformed geometry, and are likely to change with the deformation of the film. Meaning that the Young's modulus is a function of the strain, even in the elastic domain. The SVK Algorithm 6 is now used to compute the solution under the finite strain theory, and compared to the infinitesimal strain theory in Figure 28 while neglecting surface stiffness effects. It can first be observed that the elastic behavior of the sample $\mathbf{A}_1$ remains close to its linear approximation for an overall strain that is much larger that for the sample $\mathbf{A}_2$. This is due to the bending and torques generated in the structure due to the porosity.

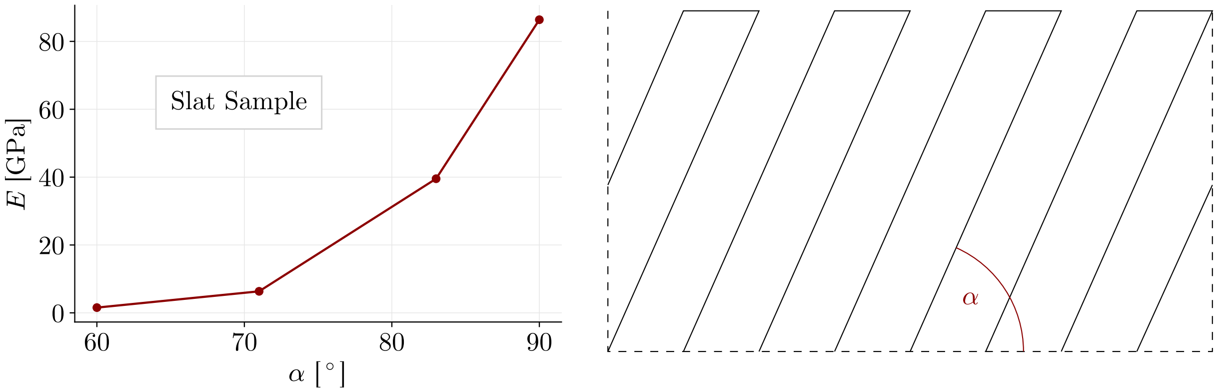

Figure 27: Young's modulus in compression along the z-axis of a slat sample with 50 % porosity. The material is periodic and its structure is composed of several columns of copper oriented at different angles with respect to the z-axis. It can be observed that the nanostructure of the film has a serious influence on its elastic properties while the porosity remains unchanged.

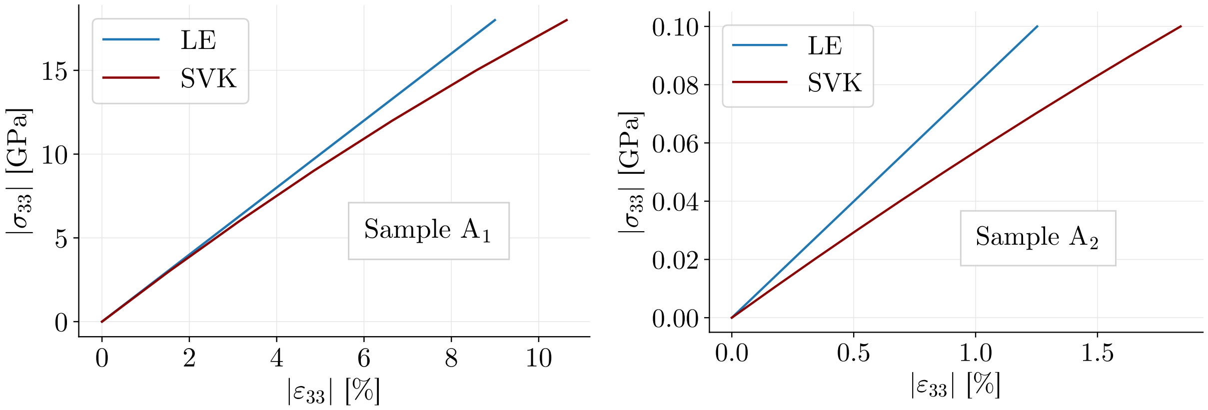

Figure 28: Comparison of the stress-strain relations in compression along the z-axis when transverse strain is prevented. In the LE model, the material is linear and E is constant. The SVK model takes into account the nonlinear terms of the strain tensor and the geometry changes in the structure, thus leading to a nonlinear stress-strain relation.

A second important parameter is the limitation of the algorithm due to collisions between the mesh and itself, or high mesh distortion. As explained in a previous chapter, the deformations of some porous structure may lead to contact between the different elements, which should be taken into account in the algorithm in order to further deform the films. Otherwise, at some critical strain, the elements start to interpenetrate, and the finite strain algorithm fails at converging to the correct solution.

- **Samples B, C and $\mathbf{A_3}$**

Those three samples represent thin films of Zr, CuZr and Cu generated by DCMS. Due to the lack of literature about the surface stiffness of Zirconium or CuZr, those samples are simulated with the bulk elastic parameters only (Figure 10), so by a vertical compression test with the LE Algorithm 5. A comparison between LE and SVK algorithms is presented in Figure 29. It can be observed that the LE approximation remains close to the nonlinear solution until 4 % of vertical strain. The relatively high Young's moduli of $\mathbf{A}_3$ compared to $\mathbf{A}_2$ is explained by the lower porosity of $\mathbf{A}_3$. Indeed, the distribution of the pores in **B**, **C** and $\mathbf{A}_3$ is relatively uniform and the effect of internal torques is reduced. Due to the difference in the bulk properties of Cu, Zr and CuZr materials, the three films display a different mechanical response.

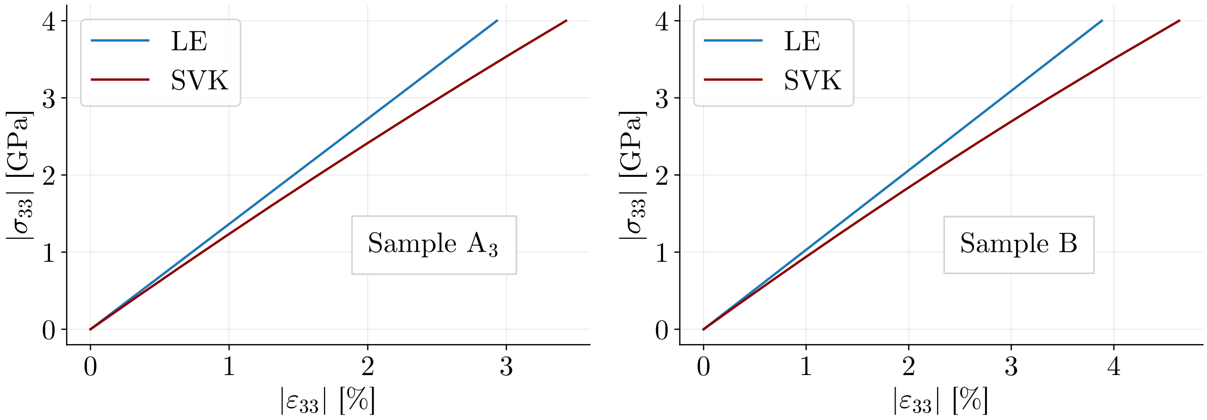

Figure 29: Comparison of the stress-strain relations in compression along the z-axis when transverse strain is prevented. In the LE model, the material is linear and E is constant. The SVK model takes into account the nonlinear terms of the strain tensor and the geometry changes in the structure, thus leading to a nonlinear stress-strain relation.

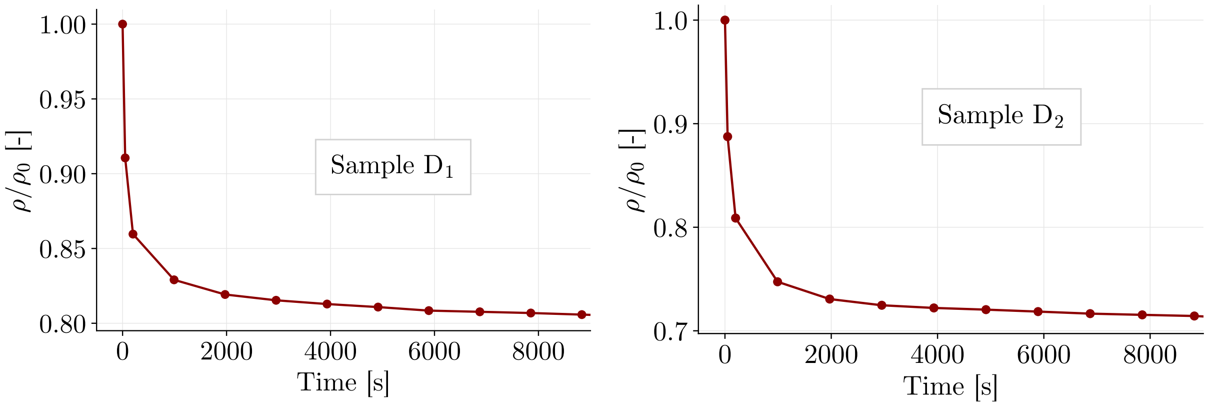

Figure 30: Normalized density of the films as a function of the simulation time of the deposition process. The graph on the left features the sample $\mathbf{D}_1$ and the image on the right features the sample $\mathbf{D}_2$.

- **Samples $\mathbf{D_1}$ and $\mathbf{D_2}$**

The two last samples feature multilayered Cu/Zr thin films or 40 layers, $\mathbf{D}_1$ has been generated in SC mode while $\mathbf{D}_2$ has been generated in DC mode by alternating between the left and right cathodes respectively for deposition of the Cu and Zr layers. The evolution of the porosity of the films is presented in Figure 30. Clearly, the porosity increases with the thickness of the film and the DC mode generates a higher porosity than the SC mode. The Young's modulus of the films is expected to decrease when the porosity increases. An overview of the layer structure is presented in Figures 31 and 32. In SC mode, the original composition of the film is preserved during the sputtering process. For the DC case, a significant change in the structure of the film occurs between 200 and 489 nm, leading to increased surface roughness at the top of the film and a progressive loss of the layered structure. Finally, a measure of the overall Young's modulus of $\mathbf{D}_1$ and $\mathbf{D}_2$ is presented in Table 10.

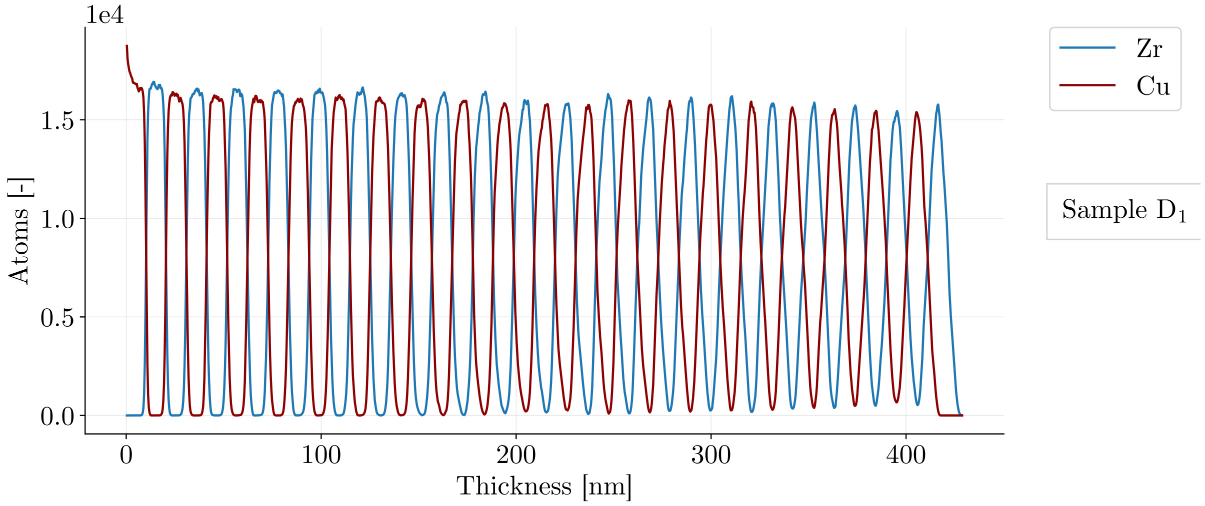

Figure 31: Number of atoms of copper and zirconium with respect to the thickness of the thin film deposited by a single cathode. The layered-structure is maintained during the deposition process and the number of atoms slowly decreases when the number of layers increases.

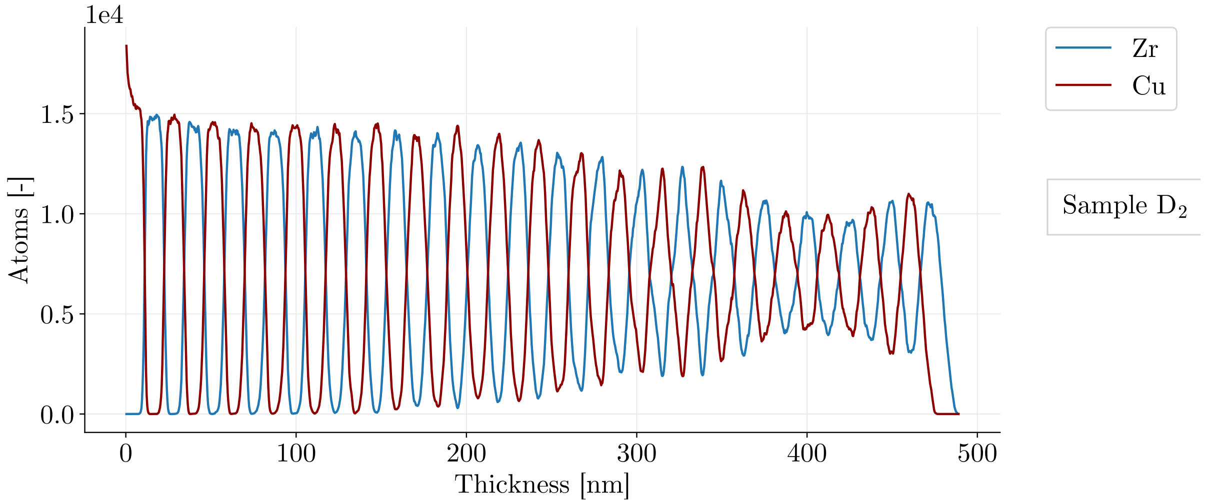

Figure 32: Number of atoms of copper and zirconium with respect to the thickness of the thin film deposited by dual cathodes. The layered-structure is maintained during the first part of the deposition process, but the clear distinction between the layers gradually disappears after 200 nm.

The Young's moduli of $\mathbf{D}_1$ and $\mathbf{D}_2$ as a function of the number of layers are presented in Figure 33. The multilayered thin films contain a large number of atoms and lead to very high computational costs. Consequently, the resolution of the FEM mesh is decreased in order to save memory. For this simulation, a finite element may contain up to 8 chemical species and the value of the maximum filling fraction f_{M} may play an important role in the FEM results. An analysis of the influence of f_{M} is presented in Figure 34. Increasing f_{M} will increase the number of empty elements and thus decrease the density of the FEM representation of the film, leading to a decrease in stiffness. Conversely, decreasing f_{M} will increase the density of the model.

4.5 Comparison with Literature

Experimental calculation of the Young's modulus may suffer from several errors inherent to the measurement tools and measurement conditions. Moreover, the surface roughness plays an important role in the measured properties of the film. Additional uncertainties are generated on the estimated property by the influence of the substrate. Indeed, it has been shown in Table 2 that different formulas lead to different results when trying to estimate the Young's modulus of the film on a substrate. Numerical calculation of the Young's modulus inevitably suffers from approximations of the mathematical model and continuum idealization of the matter, but also of the numerical tools used to solve the equations. For instance, the quality of the mesh is a crucial parameter for the quality of the solution.

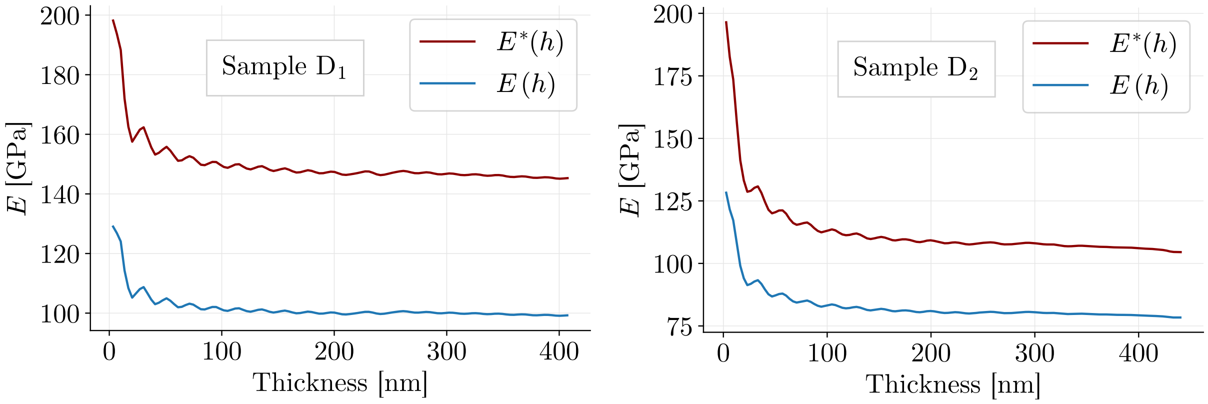

Figure 33: Young's modulus in compression of the multilayered thin films as a function of the number of layers. The quantity $E^*(h)$ denotes the Young's modulus of the sample measured when a transverse strain of the film is prevented by the substrate, as a function of the thickness h of the film.

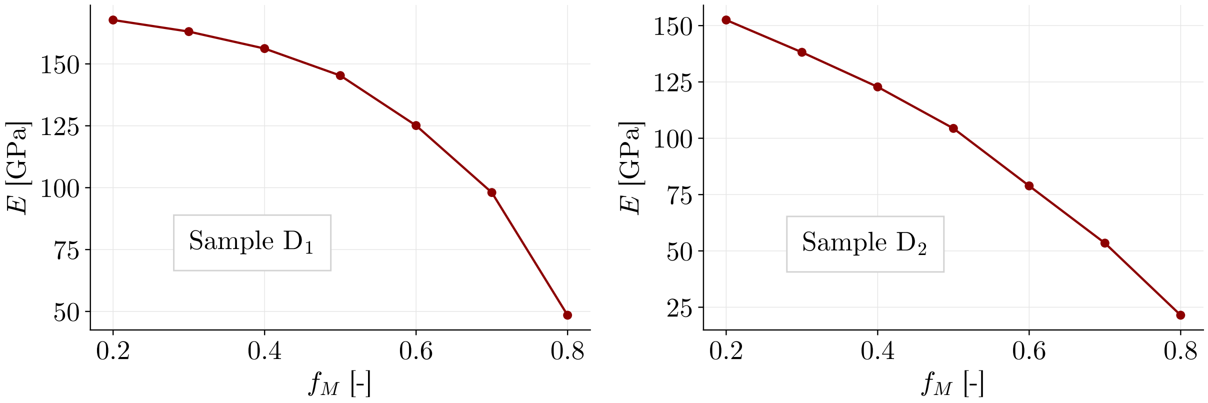

Figure 34: Young's modulus in vertical compression as a function of the filling fraction for the multilayered Cu/Zr films. The overall transverse strain of the film is prevented in this simulation.

Table 10: Overall Young's modulus in compression of the different films presented in Table 7 obtained by FEM simulation. The quantity E^* denotes the Young's modulus of the sample measured when a transverse strain of the film is prevented by the substrate.

Model	LE		SET/SST	
Modulus	E [GPa]	E^* [GPa]	E [GPa]	E^* [GPa]
$\mathbf{A}_1$	130	200	129.8	200
$\mathbf{A}_2$	7.9	8	7	7.8
$\mathbf{A}_3$	99.2	136.5	99	134.6
B	74.2	103	–	–
C	95.1	118	–	–
$\mathbf{D}_1$	99.2	145	–	–
$\mathbf{D}_2$	78.4	104.5	–	–

When the size of the sample increases, further approximations must be considered, such as the use of a representative elementary volume. All those errors lead to differences in the measured properties between experimental and numerical tests, but also between two experimental or numerical tests. Hence the importance of performing a comparative study between different sources of data. The compression Young's modulus of the film $\mathbf{A}_3$ measured by FEM is $E = 99.2$ GPa when the substrate is not considered and may reach the upper bound of $E = 136.5$ GPa when the substrate prevents an overall strain of the film in the transverse direction. This value lies in the range obtained from the literature in Tables 2 and 3 as well as in Figures 20 and 21. However, it is important to note that the thickness of $\mathbf{A}_3$ is only 25 nm while experimental values have been measured on films with a thickness of the order of 1 μm. The Young's modulus of **B** is estimated at $E \in [74.2, 103]$, this value is lower than the one obtained in the literature from Table 3 as well as Figures 21 and 20.

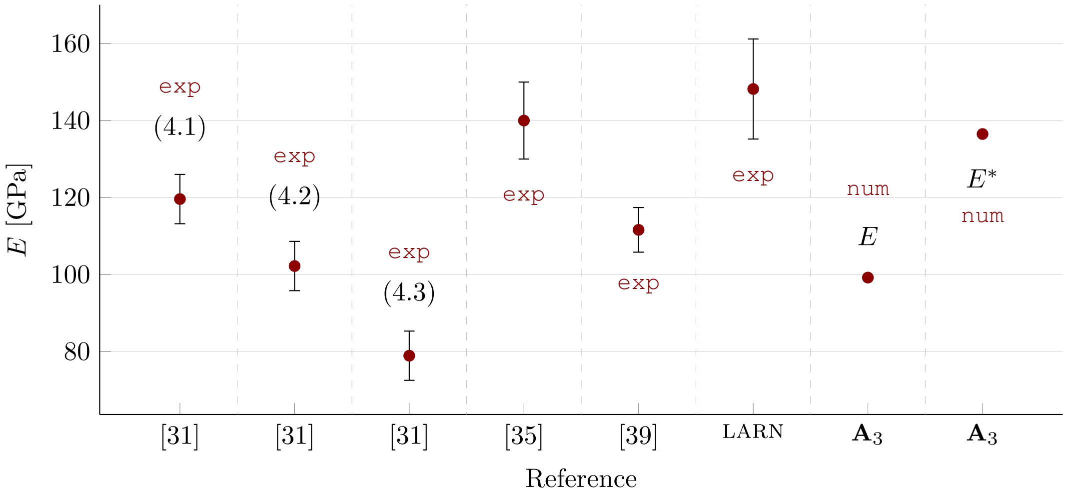

Figure 35: Comparison between experimental results (`exp`) obtained in the literature for pure Cu thin films, and numerical results (`num`) obtained in this work by NASCAM. The horizontal axis denotes the source of the measurement, so the reference of the article or the name of the sample. The vertical axis denotes the Young's modulus evaluated in compression.

This may be explained by different elastic properties of Zr at the nanoscale or a different porosity of the films. Indeed, our numerical results are highly dependent on the input parameters used for the finite elements of the mesh. Moreover, additional effects related to interatomic potential may lead to non-negligible strengthening of the Zr films, which are not taken into account in our FEM equations. The monolithic $Cu_{50}Zr_{50}$ film **C** has a compression Young's modulus estimated between 95.1 and 118 GPa. This value lies in the range obtained in the literature for amorphous films of thickness between 2 and 5 μm from Tables 3, 4, 5 and Figures 20, 21. Those elastic properties are also in agreement with the experimental results from the LARN in Table 6 measured for $Cu_{60}Zr_{40}$ and $Cu_{40}Zr_{60}$ thin films.

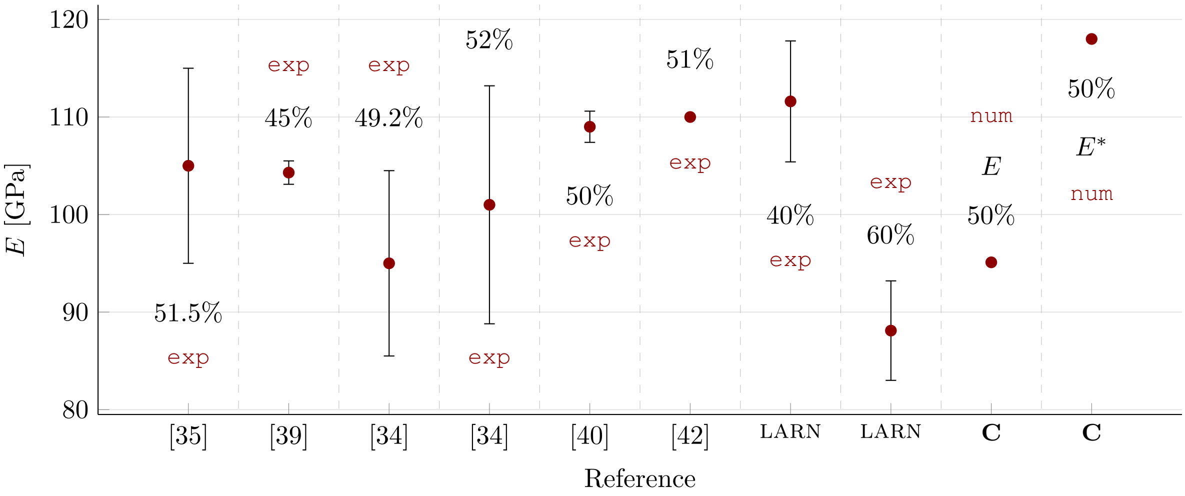

Figure 36: Comparison between experimental results (`exp`) obtained in the literature for amorphous CuZr thin films, and numerical results (`num`) obtained in this work by NASCAM. The horizontal axis denotes the source of the measurement, so the reference of the article or the name of the sample. The vertical axis denotes the Young's modulus evaluated in compression. The number in % indicates the Cu content of the composite thin film.

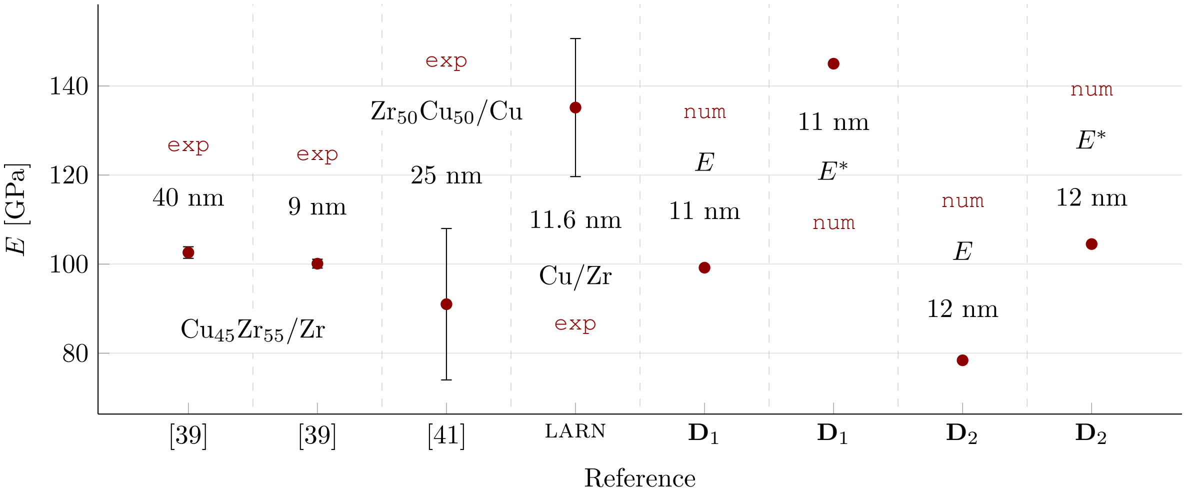

Figure 37: Comparison between experimental results obtained in the literature (`exp`) for multilayered Cu/Zr thin films, and numerical results (`num`) obtained in this work by NASCAM. The horizontal axis denotes the source of the measurement, so the reference of the article or the name of the sample. The vertical axis denotes the Young's modulus evaluated in compression. The length given in nm indicates the average thickness of each layer.

It is important to note that the thickness of **C** used for the FEM simulation is significantly lower than the films measured experimentally. The Young's modulus obtained for the multilayered films $\mathbf{D}_1$ and $\mathbf{D}_2$ lies in the range $E \in [99.2, 145]$ GPa in SC mode and $E \in [78.4, 104.5]$ GPa in DC mode. The Young's modulus measured in SC mode is close to the one obtained experimentally in the literature for $Zr_{50}Cu_{50}/Cu$ multilayers. However, the measurements from the LARN on a Cu/Zr thin film with similar thickness of (135.5 ± 15.5 GPa with 465 nm thickness) suggest that the FEM results underestimate the actual stiffness of the film. This may be due to the approximated geometry of the mesh or different phenomena occurring at the nanoscale that are not represented in our FEM model. Finally, the NASCAM representation of the thin film uses the same lattice constant for the whole structure, this hypothesis may not be satisfied in real thin films composed of different layers of pure metals. A summary of this comparison is given in Figures 35, 36 and 37.

Chapter 5

Conclusion and Perspectives

5.1 Conclusion

In this work, three FEM models have been used to evaluate the elastic properties of Cu, Zr, CuZr and multilayered Cu/Zr thin films in compression. In particular, the stress-strain relation and the Young's modulus of the overall structure were measured. Those thin films have been generated with the help of SIMTRA and NASCAM for simulating the growth of the film by magnetron sputtering on a solid substrate. The FEM algorithm and the generation of the mesh are implemented in the form of a plugin for NASCAM. Specifically, the different FEM models are the followings:

- Classical linear elasticity (LE).
- Surface elasticity and surface stress theory (SET/SST).
- Saint Venant-Kirchhoff material (SVK).

Our numerical results were compared to experimental data presented in the literature, and compared to experimental measurements from the LARN. From this study, it can be concluded that our FEM model allows to retrieve elastic properties which are in accordance with experimental results, in addition to allows a study of the impact of the substrate on the behavior of the film. Furthermore, the numerical analysis allows a study of the effects of different hypothetical porous microstructures (such as the sample $\mathbf{A}_2$) on the properties of the film. It should be noted that our numerical results tend to suggest a lower value of the Young's modulus than the one measured by nanoindentation on thicker zirconium films. Indeed, the thin films studied in the literature present structural differences with the films fabricated in the LARN or those simulated by NASCAM. In addition, the measurement errors inherent from experimental tests and the approximations of mathematical models are also responsible for the differences observed between the results.

The numerical simulation of thin films with a thickness superior to 25 nm and a porosity of approximately 15 % shows that the effect of surface stiffness by the SET/SST model does not significantly impact the elastic properties of the film. The contribution from surface stiffness become important for structures displaying a higher surface-to-volume ratio, for instance, on highly porous films or very small nanostructures. Moreover, the effect of the nonlinearity generated by the deformation of the structure (represented in the SVK model) becomes significant for axial deformations of the order of 10 % for bulk materials, 4 % for weakly porous films and 1 % for highly porous films with a structure similar to $\mathbf{A}_2$. In multilayered Cu/Zr films, the cases of SC and DC magnetron sputtering were represented by the samples $\mathbf{D}_1$ and $\mathbf{D}_2$ respectively. We have shown that the films generated in DC mode displays a higher porosity than in SC mode in addition to gradually losing the clear distinction between the different layers of Cu and Zr. The thin film thus obtained shows a lower Young's modulus than in SC mode due to the high stress concentration close to the pores. Finally, it has been observed that the Young's modulus tends to decrease with the number of layers, but may reach a relatively stable value for a large number of layers as this latter only decreases by a value of approximately 3 % between the 20-th and the 40-th layers.

5.2 Perspectives

In this section, we propose some perspectives for the improvement of the numerical model. In finite element methods, the quality of the mesh is an essential parameter for the quality of the solution and the stability of the algorithm. It has been shown that voxel-based meshes may display mathematical singularities where the elements are forming sharp angles with their neighbors. A possible perspective is thus the improvement of the mesh representing the film in order to accurately model the pores by the exploiting the isoparametric Lagrange elements implemented in this work. However, such meshes are non-trivial to generate for complex materials and thus require additional efforts.

An important part of the limitations of numerical algorithms is the computational cost. For instance, the number of finite elements used in the mesh, the format used to store the FEM matrices or the method used for solving the linear systems highly impact the performances of the code. As porous materials require a sufficiently fine mesh whose characteristic size is driven by the characteristic size of the pores, some films may become difficult to simulate accurately. Thereby, further optimisation of the code such as the use of multithreaded algorithms or GPU based libraries may be considered as a perspective.

Finally, it may be interesting to compare the results obtained with different numerical models. For instance, the couple stress theory or the AFEM may be investigated and compared to the SET/SST or the SVK models for identical thin films of very small thickness. Moreover, minor modifications of the algorithm may be proposed for taking into account the local composition of larger composite materials when the characteristic size of the finite elements is much larger than the lattice constant. For instance, when each finite element composing the mesh contain different chemical components in different proportions. Another possible extension of the algorithm is the consideration of internal contact between the elements, such feature may allow a better simulation of the deformation in highly porous films where relative displacements and rotations lead to physical contacts between the mesh and itself. However, depending on the yield strength of the material, self-contact phenomena may actually occur beyond the elastic domain, which was out of the scope of this work.

Chapter 6

Appendix

6.1 Weak Formulation

When they exist, the solutions to partial differential equations belong to a Sobolev space, which are vector spaces containing the set of functions with weak derivative up to some order. In the finite element method, one wants to work with the so-called weak formulation of the problem using the concept of weak derivative. Let f be a locally integrable function in a domain Ω, if the following definition

$$f, F \in L^1_{\text{loc}}(\Omega) : \int_\Omega f \frac{\partial^k g}{\partial x^k}\, dx = \int_\Omega F g \, dx \tag{6.1}$$

holds for all infinitely differentiable function $g \in C^\infty_c(\Omega)$, we say that F is the weak derivative of order k of the function f in this domain [17][48]. It is clear that if a function is differentiable in the classical sense, so if $g \in C^k$ for $k \in \mathbb{N} \cup \{\infty\}$, the weak derivative is the same as the classical one. Now let $\mathcal{A}$ be a partial differential operator, if the function u is sufficiently differentiable in the classical sense, then it is called a classical solution only if this latter satisfies the following relation:

$$\mathcal{A}u = f \tag{6.2}$$

for some functions $f \in \mathbb{R}^k$. On the contrary, a weak solution to this partial differential equation is a function for which the derivatives may not all exist but still satisfy the equation in some precisely definite way. In that case, u does not need to be sufficiently differentiable to make $\mathcal{A}u$ meaningful in the classical sense, but instead is meaningful in the weak sense [48].

- **Surface Gradient**

Before deriving the weak formulation of the problem (2.9), it is important to remind some properties of the surface gradient [49]. A second-order tensor $\mathbf{A}$ and a vector $\mathbf{v}$ can be decomposed into a tangential part and a normal part with respect to a surface:

$$\begin{cases} \mathbf{v} = \mathbf{v}_\text{N} + \mathbf{v}_\text{T} \\ \mathbf{A} = \mathbf{A}_\text{N} + \mathbf{A}_\text{T} \end{cases} \quad \Leftrightarrow \quad \begin{cases} \mathbf{v}_\text{T} = \mathbf{P}\mathbf{v} \\ \mathbf{A}_\text{T} = \mathbf{P}\mathbf{A}\mathbf{P} \end{cases} \tag{6.3}$$

where the surface projection tensor $\mathbf{P}$ is represented by a symmetric matrix. Those relations are used in order to derive the weak form of the initial problem with respect to the strain related to the bulk only. Furthermore, when $\mathbf{v}$ is differentiable, the surface gradient ∇_S is given with $\mathbf{P}$ as follows, where $\mathbf{n}$ is the outward normal to the surface on which the gradient is computed:

$$\begin{aligned} &\mathbf{P} = \mathbf{I} - \mathbf{n} \otimes \mathbf{n} \\ &\nabla_\text{S}\mathbf{v} = \nabla\mathbf{v} - \big(\mathbf{n} \cdot \nabla\mathbf{v}\big)\mathbf{n} = \mathbf{P} \cdot \nabla\mathbf{v} \end{aligned} \tag{6.4}$$

- **The SET and SST Models**

The weak form of the system (2.9) can be derived first by summing the partial differential equation and the Neumann boundary condition, multiplying both sides by a smooth vector field $w = [w_1 \; w_2 \; w_3]$ also called test function, which is part of the finite-dimensional subspace, then integrate over the domain:

$$\int_\Omega w^\top \big(\nabla \cdot \sigma\big)\, d\mathbf{x} = \int_\Omega w^\top \rho \frac{\partial^2 u}{\partial t^2}\, d\mathbf{x} - \int_\Omega w^\top \rho \mathbf{g}\, d\mathbf{x} - \int_{\Gamma_\text{T}} w^\top \mathbf{t}\, d\mathbf{x} \tag{6.5}$$

The divergence theorem states that the density within Ω change only by having it flow through its boundary Γ. Exploiting the property that the stress tensor is symmetric, and performing an integration by parts of the left-hand side along with applying the divergence theorem gives

$$\int_{\Omega} \sigma : \nabla w \, d\mathbf{x} - \int_{\Gamma} w^{\top} \big(\sigma \cdot \mathbf{n}\big) \, d\mathbf{x} = \int_{\Omega} w^{\top} \rho \frac{\partial^2 u}{\partial t^2} \, d\mathbf{x} - \int_{\Omega} w^{\top} \rho \mathbf{g} \, d\mathbf{x} - \int_{\Gamma_{\mathrm{T}}} w^{\top} \mathbf{t} \, d\mathbf{x} \tag{6.6}$$

We can now project the second term on both sides of the interface [19] and invoking the Laplace-Young model for the surface stress tensor (2.9), then performing an integration by part. The surface integral term in (6.6) thus becomes

$$\int_{\Gamma} w^{\top} \big(\sigma \cdot \mathbf{n}\big) \, d\mathbf{x} = \int_{\Gamma} w^{\top} \big(\nabla \cdot \sigma_{\mathrm{S}}\big) \, d\mathbf{x} = \int_{\Gamma_{\mathrm{S}}} \nabla_{\mathrm{S}} \cdot \big(w^{\top} \sigma_{\mathrm{S}}\big) \, d\mathbf{x} - \int_{\Gamma_{\mathrm{S}}} \sigma_{\mathrm{S}} : \nabla_{\mathrm{S}} w \, d\mathbf{x} \tag{6.7}$$

Since $\mathbf{P}$ acts as the identity for quantities already projected on the surface [49], the first integrand of the right-hand side can be rewritten in terms of the projection w_{S} of w on the surface using the symmetry of $\mathbf{P}$ and the identity $\mathbf{P}^2 = \mathbf{P}$. Moreover, using the divergence theorem, one can write

$$\begin{aligned} &\nabla_{\mathrm{S}} \cdot \big(w^{\top} \sigma_{\mathrm{S}}\big) = \nabla_{\mathrm{S}} \cdot \big(w^{\top} \mathbf{P} \sigma_{\mathrm{S}} \mathbf{P}\big) = \nabla_{\mathrm{S}} \cdot \big(w_{\mathrm{S}}^{\top} \sigma_{\mathrm{S}} \mathbf{P}\big) = \nabla_{\mathrm{S}} \cdot \big(w_{\mathrm{S}}^{\top} \sigma_{\mathrm{S}}\big) \\ \Leftrightarrow \; &\int_{\Gamma_{\mathrm{S}}} \nabla_{\mathrm{S}} \cdot \big(w^{\top} \sigma_{\mathrm{S}}\big) \, d\mathbf{x} = \int_{\Gamma_{\mathrm{S}}} \nabla_{\mathrm{S}} \cdot \big(w_{\mathrm{S}}^{\top} \sigma_{\mathrm{S}}\big) \, d\mathbf{x} = \int_{\varphi} w_{\mathrm{S}}^{\top} \big(\sigma_{\mathrm{S}} \cdot \mathbf{m}\big) \, d\mathbf{x} \end{aligned} \tag{6.8}$$

where φ denotes the contact line of the free surface between two subdomains, $\mathbf{n}$ is the unit outward normal to the boundary Γ. When the interface of the solid body is closed, the contact line does not exist and its integral over φ is zero. For an open interface, $\mathbf{m}$ is the outward normal to φ and tangent to Γ. Replacing (6.8) into (6.7) and (6.6) finally gives

$$\begin{aligned} &\int_{\Omega} \sigma : \nabla w \, d\mathbf{x} + \int_{\Gamma_{\mathrm{S}}} \sigma_{\mathrm{S}} : \nabla_{\mathrm{S}} w \, d\mathbf{x} - \int_{\varphi} w_{\mathrm{S}}^{\top} \big(\sigma_{\mathrm{S}} \cdot \mathbf{m}\big) \, d\mathbf{x} \\ &= \int_{\Omega} w^{\top} \rho \frac{\partial^2 u}{\partial t^2} \, d\mathbf{x} - \int_{\Omega} w^{\top} \rho \mathbf{g} \, d\mathbf{x} - \int_{\Gamma_{\mathrm{T}}} w^{\top} \mathbf{t} \, d\mathbf{x} \end{aligned} \tag{6.9}$$

The two terms featuring a double dot product with the gradient of the test function can be rewritten with by defining a virtual bulk and a surface strain tensor, thanks to their symmetry property:

$$\begin{aligned} \sigma : \nabla w &= \sigma : \frac{1}{2} \big(\nabla w + \nabla w^{\top}\big) = \sigma : \varepsilon_w \\ \sigma_{\mathrm{S}} : \nabla_{\mathrm{S}} w &= \sigma_{\mathrm{S}} : (\mathbf{P} \nabla w \mathbf{P}) = \sigma_{\mathrm{S}} : \varepsilon_w^{\mathrm{S}} \end{aligned} \tag{6.10}$$

where $\varepsilon_w = (\nabla w + \nabla w^{\top})/2$ is an analogy to the strain tensor, but with the test function instead of the displacement field. One may then rewrite (6.9) in a different way by noting $\sigma_{\mathrm{S}} \cdot \mathbf{m} = \mathbf{f}$ and injecting the relations (6.10) into (6.9), then rearranging the terms:

$$\begin{aligned} &\int_{\Omega} \sigma : \varepsilon_w \, d\mathbf{x} + \int_{\Gamma_{\mathrm{S}}} \sigma_{\mathrm{S}} : \varepsilon_w^{\mathrm{S}} \, d\mathbf{x} + \int_{\Omega} w^{\top} \rho \frac{\partial^2 u}{\partial t^2} \, d\mathbf{x} \\ &= \int_{\Omega} w^{\top} \rho \mathbf{g} \, d\mathbf{x} + \int_{\Gamma_{\mathrm{T}}} w^{\top} \mathbf{t} \, d\mathbf{x} + \int_{\varphi} w_{\mathrm{S}}^{\top} \mathbf{f} \, d\mathbf{x} \end{aligned} \tag{6.11}$$

One now needs a constitutive relation relating the stress tensors with their conjugate strain. As we are working in the framework of linear elasticity, one may inject the relations (2.10) into (6.11) to write

$$\begin{aligned} &\int_{\Omega} \varepsilon_w : \mathbb{D} : \varepsilon \, d\mathbf{x} + \int_{\Gamma_{\mathrm{S}}} \varepsilon_w^{\mathrm{S}} : \mathbb{S} : \varepsilon_{\mathrm{S}} \, d\mathbf{x} + \int_{\Omega} w^{\top} \rho \frac{\partial^2 u}{\partial t^2} \, d\mathbf{x} \\ &= \int_{\Omega} w^{\top} \rho \mathbf{g} \, d\mathbf{x} + \int_{\Gamma_{\mathrm{T}}} w^{\top} \mathbf{t} \, d\mathbf{x} + \int_{\varphi} w_{\mathrm{S}}^{\top} \mathbf{f} \, d\mathbf{x} - \int_{\Gamma_{\mathrm{S}}} \varepsilon_w^{\mathrm{S}} : \sigma_0 \, d\mathbf{x} \end{aligned} \tag{6.12}$$

and the weak formulation in terms of bulk strain is given by applying the back-projection (2.11) on the surface strain. It is important to note that the integration domains are not constant as this latter will change in time due to the deformation of the material, meaning that the integration must be conducted in the current domain instead of the reference domain.

$$\begin{aligned}&\int_\Omega \varepsilon_w : \mathbb{D} : \varepsilon \, d\mathbf{x} + \int_{\Gamma_\mathrm{S}} \big(\mathbf{P}\varepsilon_w\mathbf{P}\big) : \mathbb{S} : \big(\mathbf{P}\varepsilon\mathbf{P}\big)\, d\mathbf{x} + \int_\Omega w^\top \rho \frac{\partial^2 u}{\partial t^2}\, d\mathbf{x} \\ &= \int_\Omega w^\top \rho \mathbf{g}\, d\mathbf{x} + \int_{\Gamma_\mathrm{T}} w^\top \mathbf{t}\, d\mathbf{x} + \int_\varphi w^\top \mathbf{P}\mathbf{f}\, d\mathbf{x} - \int_{\Gamma_\mathrm{S}} \big(\mathbf{P}\varepsilon_w\mathbf{P}\big) : \sigma_0\, d\mathbf{x}\end{aligned} \tag{6.13}$$

6.2 FEM Formulation of SET/SST

In order to derive the finite-element formulation of the equation (6.13), one may define the partial derivative-matrix operator $\boldsymbol{\partial}$. Different conventions exist concerning the order of the components of the Voigt vectors, in this work, they are defined as follows:

$$\underline{\sigma} = \begin{bmatrix}\sigma_{11}\\ \sigma_{22}\\ \sigma_{33}\\ \sigma_{12}\\ \sigma_{23}\\ \sigma_{31}\end{bmatrix} \qquad \underline{\varepsilon} = \begin{bmatrix}\varepsilon_{11}\\ \varepsilon_{22}\\ \varepsilon_{33}\\ \gamma_{12}\\ \gamma_{23}\\ \gamma_{31}\end{bmatrix} \qquad \boldsymbol{\partial}^\top = \begin{bmatrix}\dfrac{\partial}{\partial x} & 0 & 0 & \dfrac{\partial}{\partial y} & 0 & \dfrac{\partial}{\partial z}\\ 0 & \dfrac{\partial}{\partial y} & 0 & \dfrac{\partial}{\partial x} & \dfrac{\partial}{\partial z} & 0\\ 0 & 0 & \dfrac{\partial}{\partial z} & 0 & \dfrac{\partial}{\partial y} & \dfrac{\partial}{\partial x}\end{bmatrix} \tag{6.14}$$

where $\gamma_{ij} = 2\varepsilon_{ij}$ is the shear strain, and the displacement field is noted $u = [u_1\ u_2\ u_3] = [u_x\ u_y\ u_z]$ in the three spatial dimensions (x, y, z) for readability reason. Using the Voigt notation, the relation between the stress, the strain and the displacement become

$$\begin{cases}\varepsilon = \dfrac{1}{2}\Big(\nabla u + \nabla u^\top\Big)\\ \sigma = \mathbb{D} : \varepsilon\end{cases} \quad\Leftrightarrow\quad \begin{cases}\underline{\varepsilon} = \boldsymbol{\partial} u\\ \underline{\sigma} = \mathbf{D}_\mathrm{B}\underline{\varepsilon} = \mathbf{D}_\mathrm{B}\big(\boldsymbol{\partial} u\big)\end{cases} \tag{6.15}$$

where $\mathbf{D}_\mathrm{B}$ is the second-order stiffness tensor of 36 components obtained by exploiting the different symmetries of $\mathbb{D}$. In addition, one can define the transition matrix $\mathbf{T}$ representing the mapping between the bulk and surface quantities in Voigt notation [23] such that the following relation holds:

$$\begin{aligned}&\varepsilon_\mathrm{S} : \sigma_\mathrm{S} = \big(\mathbf{P}\varepsilon\mathbf{P}\big) : \sigma_\mathrm{S} = \underline{\varepsilon}^\top\,\mathbf{T}\,\underline{\sigma}_\mathrm{S}\\ &\Leftrightarrow\quad \underline{\varepsilon}_\mathrm{S} = \mathbf{T}^\top\underline{\varepsilon}\end{aligned} \tag{6.16}$$

Injecting the new notations derived in (6.15) and (6.16) allows rewriting the weak form (6.13) in standard matrix-vector form as follows. A summary of the different matrices is given at the end of the subsection. Note that this equation is not yet discretized in space, one has

$$\begin{aligned}&\int_\Omega (\boldsymbol{\partial} w)^\top \mathbf{D}_\mathrm{B}\big(\boldsymbol{\partial} u\big)\, d\mathbf{x} + \int_{\Gamma_\mathrm{S}} (\boldsymbol{\partial} w)^\top \mathbf{T}\mathbf{D}_\mathrm{S}\mathbf{T}^\top\big(\boldsymbol{\partial} u\big)\, d\mathbf{x} + \int_\Omega w^\top \rho \frac{\partial^2 u}{\partial t^2}\, d\mathbf{x} \\ &= \int_\Omega w^\top \rho \mathbf{g}\, d\mathbf{x} + \int_{\Gamma_\mathrm{T}} w^\top \mathbf{t}\, d\mathbf{x} + \int_\varphi w^\top \mathbf{P}\mathbf{f}\, d\mathbf{x} - \int_{\Gamma_\mathrm{S}} \big(\boldsymbol{\partial} w\big)^\top \mathbf{T}\,\underline{\sigma_0}\, d\mathbf{x}\end{aligned} \tag{6.17}$$

where $\underline{\sigma_0}$ is the Voigt notation of σ_0. The integration domain Ω is now discretized into a series of finite elements limited to their respective subdomains forming the finite element mesh. In each element, the displacement field as well as the test function are approximated by a sum of nodal values, defined at the nodes of the elements, weighted by their respective shape functions over the element:

$$\begin{aligned} u(\mathbf{x},t) &= \mathbf{H}^\top(\mathbf{x})\,\mathbf{u}(t) \\ w(\mathbf{x},t) &= \mathbf{H}^\top(\mathbf{x})\,\mathbf{w}(t) \end{aligned} \tag{6.18}$$

In three dimensions, the matrix $\mathbf{H}$ is a $3\text{J} \times 3$ matrix containing the shape function vectors $\mathbf{N}$. The nodal unknowns are stored in $3\text{J} \times 1$ vectors, where J is the number of nodes in the element. According to this discretization, the strain tensor for the displacement field and the virtual strain tensor for the test function in (6.17) can be written as the following matrix-vector form

$$\underline{\varepsilon} = \boldsymbol{\partial} u = \boldsymbol{\partial}\mathbf{H}^\top\mathbf{u} = \mathbf{B}^\top\mathbf{u} \tag{6.19}$$

where the partial differential operator $\boldsymbol{\partial}$ is applied to the matrix of shape functions only, because the vector of unknown nodal displacement $\mathbf{u}$ and nodal test functions $\mathbf{w}$ are not a function of (x, y, z). Injecting this decomposition into (6.17), which will now refer to an integration over the discretized domain by assembling the different contributions of the finite elements, allows deriving the space-discretized equation of the problem. As the vector of nodal unknown are not functions of the position, they can be placed out of the integrals. Finally, this formulation is valid for any smooth test function, this latter can thus be simplified from the equation, leading to

$$\begin{aligned} &\int_\Omega \mathbf{B}\mathbf{D}_{\text{B}}\mathbf{B}^\top d\mathbf{x}\,\mathbf{u} + \int_{\Gamma_{\text{S}}} \mathbf{B}\mathbf{T}\mathbf{D}_{\text{S}}\mathbf{T}^\top\mathbf{B}^\top d\mathbf{x}\,\mathbf{u} + \int_\Omega \mathbf{H}\mathbf{H}^\top\rho\,d\mathbf{x}\,\frac{d^2\mathbf{u}}{dt^2} \\ &= \int_\Omega \mathbf{H}\rho\mathbf{g}\,d\mathbf{x} + \int_{\Gamma_{\text{T}}} \mathbf{H}\mathbf{t}\,d\mathbf{x} + \int_\varphi \mathbf{H}\mathbf{P}\mathbf{f}\,d\mathbf{x} - \int_{\Gamma_{\text{S}}} \mathbf{B}\mathbf{T}\underline{\sigma}_0\,d\mathbf{x} \end{aligned} \tag{6.20}$$

Note that the shape functions in $\mathbf{B}$ which are not related to the considered surface Γ are suppressed by the projection matrix $\mathbf{T}$. In order to simplify the notations, we define the bulk stiffness matrix $\mathbf{K}_{\text{B}}$ and the surface stiffness matrix $\mathbf{K}_{\text{S}}$, as well as the mass matrix $\mathbf{M}$ in the left-hand side. In the right-hand side, we define the vector of external loads $\mathbf{F}_{\text{T}}$, the vector of body forces $\mathbf{F}_{\text{B}}$, the vector of surface-boundary traction $\mathbf{F}_\varphi$ and the vector of residual surface stress $\mathbf{F}_{\text{S}}$ such that (6.20) becomes

$$\begin{aligned} &\big(\mathbf{K}_{\text{B}} + \mathbf{K}_{\text{S}}\big)\mathbf{u} + \mathbf{M}\,\frac{d^2\mathbf{u}}{dt^2} = \mathbf{F}_{\text{B}} + \mathbf{F}_{\text{T}} + \mathbf{F}_\varphi - \mathbf{F}_{\text{S}} \\ \Leftrightarrow \quad &\mathbf{K}\mathbf{u} + \mathbf{M}\,\frac{d^2\mathbf{u}}{dt^2} = \mathbf{F} \end{aligned} \tag{6.21}$$

6.3 FEM Formulation of SVK

In the total Lagrangian formulation, the stress and strain measures in the current configuration are computed with respect to the initial configuration, as well as the derivatives and integrals. However, the equation (2.23) in finite strain elasticity is nonlinear with respect to the displacement:

$$K(u, w) = f(w) \tag{6.22}$$

and cannot be directly written as $\mathbf{K}\mathbf{u} = \mathbf{b}$. The next step is then the linearization of $K(u, w)$ by performing a first-order Taylor approximation of the stiffness matrix. Introducing the incremental displacement δu as the new variable, one can follow the procedure described in [50] to derive

$$\mathcal{L}\Big[K(u, w)\Big](\delta u) = \int_{\Omega_0} \Big(\delta\mathbf{S} : \mathbf{E}_w + \mathbf{S} : \delta\mathbf{E}_w\Big)\,d\mathbf{x} \tag{6.23}$$

where $\delta\mathbf{S}$ is the stress increment and $\delta\mathbf{E}_w$ is an equivalent to the increment of strain written in terms of the test function. For a Saint-Venant-Kirchhoff material, the stress-strain relation is linear with respect to the increment of stress and one has $\delta\mathbf{S} = \mathbb{D} : \delta\mathbf{E}$. Moreover, the increment of Lagrangian strain and its equivalent test function [51] can be obtained as follows:

$$\begin{aligned}
\mathbf{E}_w &= \mathrm{sym}\Big(\nabla w^\top + \nabla w^\top \nabla u\Big) \\
\delta\mathbf{E} &= \mathrm{sym}\Big(\nabla \delta u^\top + \nabla \delta u^\top \nabla u\Big) \\
\delta\mathbf{E}_w &= \mathrm{sym}\Big(\nabla w^\top \nabla \delta u\Big)
\end{aligned} \tag{6.24}$$

where the notations $\mathrm{sym}(\mathbf{A}) = (\mathbf{A} + \mathbf{A}^\top)/2$ and $\nabla = \nabla_{\mathbf{X}}$ have been used for readability reason. Because those strain tensors as well as the second Piola-Kirchhoff stress tensor are symmetric, one can introduce the Voigt notation and write the tensors in terms of vectors:

$$\underline{S} = \mathbf{D}\underline{E} = \begin{bmatrix} S_{11} \\ S_{22} \\ S_{33} \\ S_{12} \\ S_{23} \\ S_{31} \end{bmatrix} \quad \underline{E} = \begin{bmatrix} E_{11} \\ E_{22} \\ E_{33} \\ 2E_{12} \\ 2E_{23} \\ 2E_{31} \end{bmatrix} \quad \begin{cases} \underline{E}_w = \boldsymbol{\partial}_{\mathrm{N}} w \\ \delta\underline{E} = \boldsymbol{\partial}_{\mathrm{N}}\, \delta u \\ \delta\underline{S} = \mathbf{D}\, \delta\underline{E} \end{cases} \tag{6.25}$$

Where $\boldsymbol{\partial}_{\mathrm{N}}$ is the nonlinear differential operator and function of the total displacement u which is known and taken as the solution obtained in the previous step, so at the reference configuration for the first step of the algorithm. The stiffness tensor $\mathbf{D}_{\mathrm{B}}$ is equivalent to the LE tensor, one has

$$\begin{aligned}
\delta\mathbf{S} : \mathbf{E}_w &= \underline{E}_w^\top \mathbf{D}_{\mathrm{B}}\, \delta\underline{E} = (\boldsymbol{\partial}_{\mathrm{N}} w)^\top \mathbf{D}_{\mathrm{B}}\, (\boldsymbol{\partial}_{\mathrm{N}} \delta u) \\
\mathbf{S} : \delta\mathbf{E}_w &= (\boldsymbol{\partial}_{\mathrm{L}} w)^\top \boldsymbol{\Sigma}\, (\boldsymbol{\partial}_{\mathrm{L}} \delta u)
\end{aligned} \tag{6.26}$$

Using the finite element discretization for the test function $w = \mathbf{H}^\top \mathbf{w}$ and the increment of displacement $\delta u = \mathbf{H}^\top \delta\mathbf{u}$, where $\mathbf{H}$ is the matrix of shape functions, allows the writing of the relations (6.26) into a purely vector form. For an element of the mesh, one has

$$\begin{aligned}
\delta\mathbf{S} : \mathbf{E}_w &= \mathbf{w}^\top \mathbf{B}_{\mathrm{N}} \mathbf{D}_{\mathrm{B}} \mathbf{B}_{\mathrm{N}}^\top \delta\mathbf{u} \\
\mathbf{S} : \delta\mathbf{E}_w &= \mathbf{w}^\top \mathbf{B}_{\mathrm{L}} \boldsymbol{\Sigma} \mathbf{B}_{\mathrm{L}}^\top \delta\mathbf{u}
\end{aligned} \tag{6.27}$$

where $\mathbf{B}_{\mathrm{L}}$ is a linear matrix of shape function derivatives, which is independent of the total displacement, and $\mathbf{B}_{\mathrm{N}}$ is the nonlinear matrix of shape function derivatives that involves the deformation gradient tensor at computed the previous step. These matrices are given in the equation (2.26). The linearized relation (6.23) can be written in terms of the product of the vector of nodal values of the shape functions and incremental displacements, with a so-called tangent stiffness matrix $\mathbf{K}_{\mathrm{T}}(\mathbf{u})$ representing the derivative of the nonlinear strain-displacement at $\mathbf{u}$, finally leading to

$$\begin{aligned}
\mathcal{L}\Big[K(u,w)\Big](\delta u) &= \int_{\Omega_0} \mathbf{w}^\top \mathbf{B}_{\mathrm{N}} \mathbf{D}_{\mathrm{B}} \mathbf{B}_{\mathrm{N}}^\top \delta\mathbf{u}\, d\mathbf{x} + \int_{\Omega_0} \mathbf{w}^\top \mathbf{B}_{\mathrm{L}} \boldsymbol{\Sigma} \mathbf{B}_{\mathrm{L}}^\top \delta\mathbf{u}\, d\mathbf{x} \\
&= \mathbf{w}^\top \big(\mathbf{K}_{\mathrm{N}} + \mathbf{K}_{\mathrm{L}}\big)\, \delta\mathbf{u} = \mathbf{w}^\top \mathbf{K}_{\mathrm{T}}\, \delta\mathbf{u}
\end{aligned} \tag{6.28}$$

In order to solve the system (2.23), the Newton-Raphson algorithm is used to converge to the correct solution by minimizing a residual $\mathbf{R}$ representing the out-of-equilibrium stresses. At each iteration, the residual is computed by taking the difference between the external applied forces and the internal forces at the current configuration:

$$\begin{aligned}\mathbf{w}^\top \mathbf{R} &= \int_{\Gamma_0} w^\top \mathbf{t}\, d\mathbf{x} - \int_{\Omega_0} \mathbf{S} : \mathbf{E}_w \, d\mathbf{x} \\ &= \mathbf{w}^\top \int_{\Gamma_0} \mathbf{H}\mathbf{t}\, d\mathbf{x} - \mathbf{w}^\top \int_{\Omega_0} \mathbf{B}_{\mathrm{N}} \mathbf{D}_{\mathrm{B}} \underline{E}\, d\mathbf{x} \\ &= \mathbf{w}^\top \big(\mathbf{F}_{\mathrm{T}} - \mathbf{F}_{\mathrm{X}}\big)\end{aligned} \tag{6.29}$$

The Newton Raphson algorithm is then used to find a solution for a vanishing residual stress $\mathbf{R}$. As the Newton Raphson algorithm will converge to the closest local minima, which may not be the global minima, it is important that the starting point is close enough from the correct solution. To this end, the load $\mathbf{t}$ is generally partitioned into several load increments, and the algorithm will find an equilibrium solution for each of these increments until the total load is reached.

$$\mathbf{w}^\top \mathbf{K}_{\mathrm{T}} \delta \mathbf{u} = \mathbf{w}^\top \mathbf{R} \quad \Leftrightarrow \quad \mathbf{K}_{\mathrm{T}} \delta \mathbf{u} = \mathbf{F}_{\mathrm{T}} - \mathbf{F}_{\mathrm{X}} \tag{6.30}$$

Ultimately, the second Piola Kirchhoff stress tensor can be projected into the current configuration in order to recover the Cauchy stress. It is important to note that only the displacement has an accurate and continuous value over the domain thanks to the shape functions, thus evaluating the stress at the nodes may lead to catastrophic results. Practically, the stress is only known on average and will be averaged over an element from its values computed at the Gauss nodes.

$$\sigma = \frac{1}{\det(\mathbf{F})} \mathbf{F}\mathbf{S}\mathbf{F}^\top \tag{6.31}$$

6.4 Surface Integration

In order to compute the projection tensor $\mathbf{P} = \mathbf{I} - \mathbf{n} \otimes \mathbf{n}$ to a surface of a general hexahedron element, one first need to compute the outward normal to this surface in global coordinates. Which can be obtained by defining the following mapping vectors of the Jacobian:

$$\begin{aligned}\mathbf{v}_\xi^\top &= \begin{bmatrix} \frac{\partial x}{\partial \xi} & \frac{\partial y}{\partial \xi} & \frac{\partial z}{\partial \xi} \end{bmatrix} = \mathrm{row}_1\big(\mathbf{J}\big) \\ \mathbf{v}_\eta^\top &= \begin{bmatrix} \frac{\partial x}{\partial \eta} & \frac{\partial y}{\partial \eta} & \frac{\partial z}{\partial \eta} \end{bmatrix} = \mathrm{row}_2\big(\mathbf{J}\big) \\ \mathbf{v}_\varphi^\top &= \begin{bmatrix} \frac{\partial x}{\partial \varphi} & \frac{\partial y}{\partial \varphi} & \frac{\partial z}{\partial \varphi} \end{bmatrix} = \mathrm{row}_3\big(\mathbf{J}\big)\end{aligned} \tag{6.32}$$

Then, we compute the two director vectors denoting the orientations of the surface area element in the global space, which can be expressed by the Gram-Schmidt orthogonalization [52][53]. One has first

$$\begin{aligned}\mathbf{v} &= \mathbf{v}_\varphi - \big(\mathbf{v}_\varphi \cdot \mathbf{v}_\eta\big)\mathbf{v}_\eta && \text{for face } \xi = \pm 1 \\ \mathbf{v} &= \mathbf{v}_\xi - \big(\mathbf{v}_\xi \cdot \mathbf{v}_\varphi\big)\mathbf{v}_\varphi && \text{for face } \eta = \pm 1 \\ \mathbf{v} &= \mathbf{v}_\eta - \big(\mathbf{v}_\eta \cdot \mathbf{v}_\xi\big)\mathbf{v}_\xi && \text{for face } \varphi = \pm 1\end{aligned} \tag{6.33}$$

The second director vector is taken from (6.32) depending on the face considered. The change of surface area due to the mapping $[x\ y\ z] \to [\xi\ \eta\ \varphi]$ as well as the unit outward normal are computed by

$$\begin{aligned}J &= |\mathbf{v} \times \mathbf{v}_\varphi| & \mathbf{n} &= \pm\big(\mathbf{v} \times \mathbf{v}_\varphi\big)J^{-1} & &\text{face } \xi = \pm 1 \\ J &= |\mathbf{v} \times \mathbf{v}_\xi| & \mathbf{n} &= \pm\big(\mathbf{v} \times \mathbf{v}_\xi\big)J^{-1} & &\text{face } \eta = \pm 1 \\ J &= |\mathbf{v} \times \mathbf{v}_\eta| & \mathbf{n} &= \pm\big(\mathbf{v} \times \mathbf{v}_\eta\big)J^{-1} & &\text{face } \varphi = \pm 1\end{aligned} \tag{6.34}$$

The integrals in $\mathbf{K}_\text{S}$ and $\mathbf{F}_\text{S}$ defined on the free surfaces of the element can thus be computed using the appropriate quadrature rule whose nodes are located at the surface considered with the equation (6.36). It is important to note that the external traction $\mathbf{F}_\text{T}$ is not directly linked to the 3D elements as in the case of surface effects. Thereby, one can alternatively define an independent 2D quadrangle Lagrange element of K nodes and perform the integration. The mapping $[x\ y\ z] \rightarrow [\xi\ \eta]$ between the global 3D space and the local 2D space of the new quadrangle element leads to

$$\begin{cases} \mathbf{v}_1^\top = \begin{bmatrix} \dfrac{\partial x}{\partial \xi} & \dfrac{\partial y}{\partial \xi} & \dfrac{\partial z}{\partial \xi} \end{bmatrix} \\ \mathbf{v}_2^\top = \begin{bmatrix} \dfrac{\partial x}{\partial \eta} & \dfrac{\partial y}{\partial \eta} & \dfrac{\partial z}{\partial \eta} \end{bmatrix} \end{cases} \quad \Leftrightarrow \quad \begin{cases} J = |\mathbf{v}_1 \times \mathbf{v}_2| \\ \mathbf{n} = \dfrac{\mathbf{v}_1 \times \mathbf{v}_2}{|\mathbf{v}_1 \times \mathbf{v}_2|} \end{cases} \tag{6.35}$$

where the vectors $\mathbf{v}_1$ and $\mathbf{v}_2$ are obtained similarly to (2.6) using the 2D shape functions and the corresponding K nodes of the quadrangle. Their cross product is normal to this surface and its norm gives the surface change of the transformation. Consequently, the surface integral on Γ defined in a 3D space can be computed in the local 2D space $\Gamma' = [-1, 1]^2$ as follows:

$$\int_\Gamma f(\mathbf{x})\, d\mathbf{x} = \int_{\Gamma'} f\left[\mathbf{x}(\boldsymbol{\xi})\right] J(\boldsymbol{\xi})\, d\boldsymbol{\xi} \tag{6.36}$$

6.5 Energy and Angular Distributions

In this annex, the analytical distributions obtained from SIMTRA simulations are explicitly given at the particular pressure $P = 0.67$ Pa with a polynomial expansion of order 5. Practically, it is preferable to use the full surrogate model given in matrix form by the PCE code implemented in `Python`, in order to avoid further rounding errors, or possibly increase the order of the expansion when needed, the distributions given here are thus for information purpose only. As a reminder, we use

$$E \rightarrow \varepsilon \text{ with } \varepsilon = \ln E \tag{6.37}$$

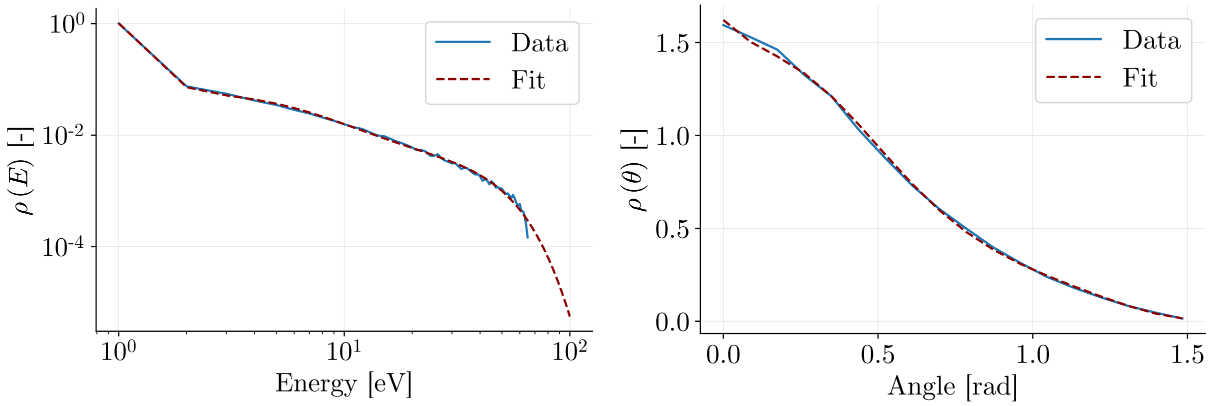

Figure 38: Comparison between the PCE surrogate model of order 5 and the simulation data obtained by SIMTRA for Cu sputtered by SC magnetron sputtering at $P = 0.67$ Pa. The corresponding expression for the energy and angular distributions are given in (6.38).

$$\boxed{\begin{aligned}\rho_{\mathrm{E}}(\varepsilon) &= \exp\left(0.01889 - 7.834\,\varepsilon + 8.434\,\varepsilon^2 - 4.507\,\varepsilon^3 + 1.086\,\varepsilon^4 - 0.0981\,\varepsilon^5\right)\\ \rho_{\mathrm{A}}(\theta) &= \exp\left(0.483 - 1.151\,\theta + 4.574\,\theta^2 - 15.104\,\theta^3 + 14.932\,\theta^4 - 5.014\,\theta^5\right)\end{aligned}} \tag{6.38}$$

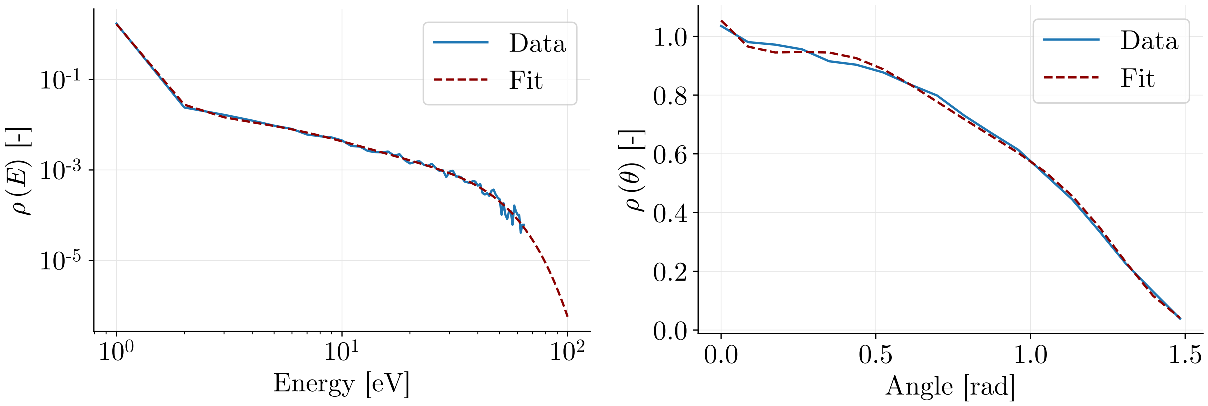

Figure 39: Comparison between the PCE surrogate model of order 5 and the simulation data obtained by SIMTRA for Cu sputtered by DC magnetron sputtering at $P = 0.67$ Pa. The corresponding expression for the energy and angular distributions are given in (6.39).

$$\boxed{\begin{aligned}\rho_{\mathrm{E}}(\varepsilon) &= \exp\left(0.5217 - 11.182\,\varepsilon + 10.6343\,\varepsilon^2 - 5.1663\,\varepsilon^3 + 1.181\,\varepsilon^4 - 0.1041\,\varepsilon^5\right)\\ \rho_{\mathrm{A}}(\theta) &= \exp\left(0.05252 - 1.61824\,\theta + 8.4999\,\theta^2 - 18.89\,\theta^3 + 17.001\,\theta^4 - 5.5983\,\theta^5\right)\end{aligned}} \tag{6.39}$$

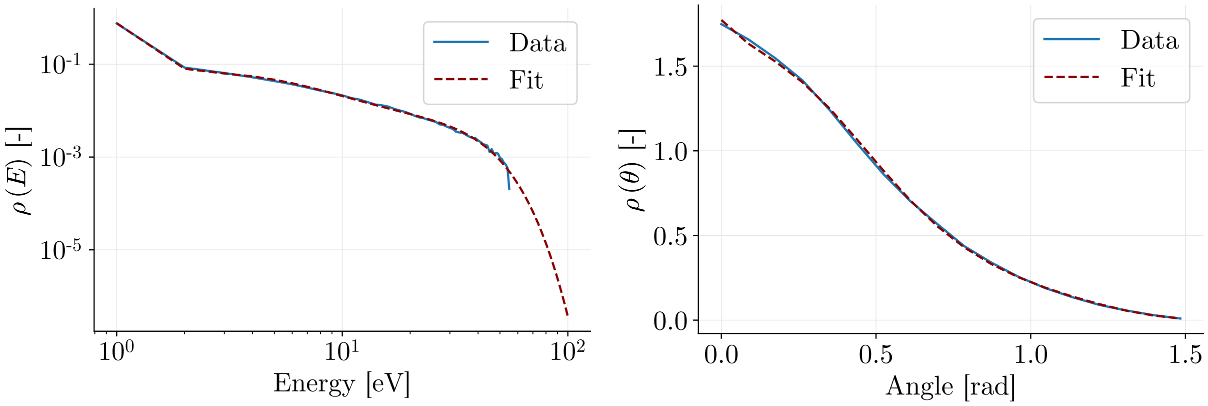

Figure 40: Comparison between the PCE surrogate model of order 5 and the simulation data obtained by SIMTRA for Zr sputtered by SC magnetron sputtering at $P = 0.67$ Pa. The corresponding expression for the energy and angular distributions are given in (6.40).

$$
\boxed{\begin{aligned}
\rho_{\mathrm{E}}(\varepsilon) &= \exp\Big(-0.2647 - 7.121\,\varepsilon + 8.3068\,\varepsilon^2 - 4.7338\,\varepsilon^3 + 1.2109\,\varepsilon^4 - 0.1159\,\varepsilon^5\Big)\\
\rho_{\mathrm{A}}(\theta) &= \exp\Big(0.5723 - 1.1874\,\theta + 4\,\theta^2 - 14.223\,\theta^3 + 14.0497\,\theta^4 - 4.709\,\theta^5\Big)
\end{aligned}} \tag{6.40}
$$

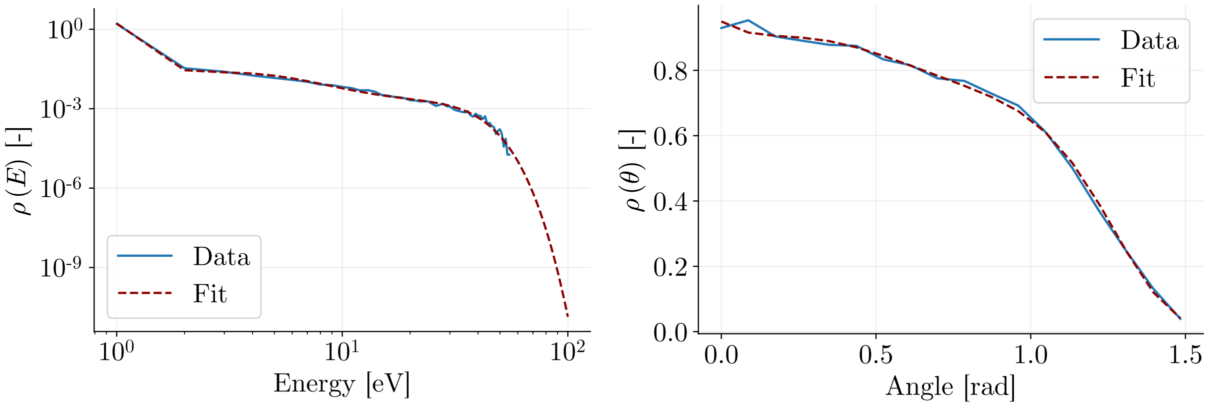

Figure 41: Comparison between the PCE surrogate model of order 5 and the simulation data obtained by SIMTRA for Zr sputtered by the DC magnetron sputtering at $P = 0.67$ Pa. The corresponding expression for the energy and angular distributions are given in (6.41).

$$
\boxed{\begin{aligned}
\rho_{\mathrm{E}}(\varepsilon) &= \exp\Big(0.5108 - 13.8933\,\varepsilon + 17.4114\,\varepsilon^2 - 10.1527\,\varepsilon^3 + 2.656\,\varepsilon^4 - 0.2577\,\varepsilon^5\Big)\\
\rho_{\mathrm{A}}(\theta) &= \exp\Big(-0.05174 - 0.668\,\theta + 3.653\,\theta^2 - 9.548\,\theta^3 + 10.008\,\theta^4 - 3.8256\,\theta^5\Big)
\end{aligned}} \tag{6.41}
$$

References

---

[1] S. Lucas and P. Moskovkin. “Simulation at High Temperature of Atomic Deposition, Islands Coalescence, Ostwaldand Inverse Ostwald Ripening with a General Simple Kinetic Monte Carlo Code”. In: *Thin Solid Films* **518** (2010), pp. 5355–5361.

[2] N.J. Dudney and B.J. Neudecker. “Solid State Thin-Film Lithium Battery Systems”. In: *Current Opinion in Solid State and Materials Science* **4** (1999), pp. 479–482.

[3] Nianduan Lu et al. “A Review for Compact Model of Thin-Film Transistors”. In: *Micromachines* **9** (2018), p. 599.

[4] M. Ramirez-del-Solar and E. Blanco. *Porous Thin Films from Sol-Gel.* Springer International Publishing, 2017.

[5] Eric K. Lin et al. “Structure and Property Characterization of Porous Low-k Dielectric Constant Thin Films using X-ray Reflectivity and Small Angle Neutron Scattering”. In: *Materials Research Society* **612** (2000), pp. D4.4.4–D4.1.8.

[6] W.D Mix. “Mechanical Properties of Thin Films”. In: *Metallurgical Transactions A* **20** (1989), p. 2217.

[7] M.C. Rao and Manoj Shekhawat. “A Brief Survey on Basic Properties of Thin Films for Device Application”. In: *International Journal of Modern Physics Conference Series* **45** (2013), pp. 576–582.

[8] Liu Bin et al. “The Atomic-Scale Finite Element Method”. In: *Computer Methods in Applied Mechanics and Engineering* **193** (2004), pp. 1849–1864.

[9] Damasceno Daniela, Mesquita Euclides, and Rajapakse Nimal. “Mechanical Behavior of Nano Structures Using Atomic-Scale Finite Element Method”. In: *Latin American Journal of Solids and Structures* **14** (2017), pp. 2046–2066.

[10] Castrenze Polizzotto. “Non Local Elasticity and Related Variational Principles”. In: *International Journal of Solids and Structures* **38** (2001), pp. 7359–7380.

[11] Kwon Young-Rok and Lee Byung-Chai. “Three Dimensional Elements with Lagrange Multipliers for the Modified Couple Stress Theory”. In: *Computational Mechanics* **62** (2018).

[12] Shang Yan, Li Chen-Feng, and Jia Kang-Yu. “8-Node Hexahedral Unsymmetric Element with Rotation Degrees of Freedom for Modified Couple Stress Elasticity”. In: *International Journal for Numerical Methods in Engineering* **121** (2020), pp. 2683–2700.

[13] Abazari Amir et al. “Size Effects on Mechanical Properties of Micro/Nano Structures”. In: *Sensors* **15** (2015), pp. 1–19.

[14] Feng Yankun and Liu Yulan. “Finite Element Analysis of Resonant Properties of Silicon Nanowires with Consideration of Surface Effects”. In: *Acta Mechanica* **217** (2011), pp. 149–155.

[15] Gao Wei, Yu Shou-Wen, and Huang Gan-Yun. “Finite Element Characterization of the Size-Dependent Mechanical Behaviour in Nanosystems”. In: *Nanotechnology* **17** (2006), pp. 1118–1122.

[16] A.A. Pisano, A. Sofi, and P. Fuschi. “Nonlocal Integral Elasticity 2D Finite Element Based Solutions”. In: *International Journal of Solids and Structures* **46** (2009), pp. 3836–3849.

[17] Vincent Manet. *Méthode des Élements Finis: Vulgarisation des Aspects Mathématiques, Illustration des Capacités de la Méthode*. Lyon, France, 2013, pp. 367–364.

[18] Martin Lacroix. “Propagation of Uncertainties in Pyrolysis Kinetic Parameters Using Polynomial Chaos Methods”. MA thesis. Belgium: University of Liège, 2020.

[19] Hachi Brahim et al. “Some Investigations on 3D Homogenization of NanoComposite/NanoPorous Materials with Surface Effect by FEM/XFEM Methods Combined with Level-Set Technique”. In: *Computer Methods in Applied Mechanics and Engineering* **371** (2020), p. 113319.

[20] Jean-Philippe Ponthot. *Finite Element Method*. Lecture notes: Aerospace and Mechanical Laboratory, University of Liège. 2016.

[21] Jean-Philippe Ponthot. *Advanced Solid Mechanics*. Lecture notes: Aerospace and Mechanical Laboratory, University of Liège. 2017.

[22] Neculai Andrei. *Nonlinear Conjugate Gradient Methods for Unconstrained Optimization*. Switzerland: Springer International Publishing, 2020.

[23] Farsad Mehdi, Vernerey Franck, and Park Harold. “An Extended Finite Element Level Set Method to Study Surface Effects on the Mechanical Behavior and Properties of Nanomaterials”. In: *International Journal for Numerical Methods in Engineering* **84** (2010), pp. 1466–1489.

[24] Ronald Miller and B. Shenoy. “Size-Dependent Elastic Properties of Nanosized Structural Elements”. In: *Nanotechnology* **11** (2000), p. 139.

[25] Weifeng Wang, Xianwei Zeng, and Jianping Ding. “Finite Element Modeling of two-dimensional Nanoscale Structures with Surface Effects”. In: *International Journal of Civil and Environmental Engineering* **4** (2010), pp. 865–870.

[26] M.R. Kired, B.E. Hachi, and D. Hachi M. Haboussi. “Effects of Nano-Voids and Nano-Cracks on the Elastic Properties of a Host Medium: XFEM Modeling with the Level-Set Function and Free Surface Energy”. In: *Acta Mechanica Sinica* **35** (2019), pp. 799–811.

[27] H.L. Duan et al. “Nanoporous Materials can be Made Stiffer than Non-Porous Counterparts by Surface Modification”. In: *Acta Materialia* **11** (2006), pp. 2983–2990.

[28] John Jaeger, N.G. Cook, and Robert Zimmerma. *Fundamentals of Rock Mechanics*. Singapore: Blackwell, 2007.

[29] By Asim Jilani, Mohamed Shaaban Abdel-Wahab, and Ahmed Hosny Hammad. *Advance Deposition Techniques for Thin Film and Coating*. InTechOpen, 2017.

[30] Daniel Lundin, Tiberiu Minea, and Jon Tomas Gudmundsson. *High Power Impulse Magnetron Sputtering: Fundamentals, Technologies, Challenges and Applications*. Amsterdam, Netherlands: Elsevier Science Ltd, 2019.

[31] Ioana-Laura Velicu et al. “Copper Thin Films Deposited Under Different Power Delivery Modes and Magnetron Configurations: A Comparative Study”. In: *Surface and Coatings Technology* **327** (2016), pp. 1–7.

[32] W. Oliver and G. Pharr. “Measurement of Hardness and Elastic Modulus by Instrumented Indentation: Advances in Understanding and Refinements to Methodology”. In: *Journal of Materials Research* **19** (2004), pp. 3–20.

[33] Alisafaei Farid and Han Chung-Souk. "Indentation Depth Dependent Mechanical Behavior in Polymers". In: *Advances in Condensed Matter Physics* **612** (2015), pp. 1–20.

[34] Mihai Apreutesei et al. "Microstructural, Thermal and Mechanical Behavior of Co-Sputtered Binary Zr-Cu Thin Film Metallic Glasses". In: *Thin Solid Films* **561** © (2014), pp. 53–59.

[35] P. Coddet et al. "On the Elastic Modulus and Hardness of Co-Sputtered Zr-Cu-(N) Thin Metal Glass Films". In: *Surface and Coatings Technology* **206** © (2012), pp. 3567–3571.

[36] F. Zeng et al. "Elastic Modulus and Hardness of Cu–Ta Amorphous Films". In: *Journal of Alloys and Compounds* **389** (2005), pp. 75–79.

[37] Robert B. Ross. *Metallic Materials Specification Handbook.* United Kingdom: Springer, 1992.

[38] E.A. Brandes and G.B. Brook. *Smithells Metals Reference Book.* Oxford, Boston: Butterworth-Heinemann, 1998.

[39] Mohammad Abboud. "Micromechanical Characterization of Metallic Glass - Crystalline Nanocomposite Coatings". MA thesis. Turkey: Middle East Technical University, 2018.

[40] A. Rauf et al. "Binary Cu-Zr Thin Film Metallic Glasses with Tunable Nanoscale Structures and Properties". In: *Journal of Non-Crystalline Solids* **408** (2018), pp. 95–102.

[41] H.J. Pei et al. "Tension Behavior of Metallic Glass Coating on Cu Foil". In: *Materials Science and Engineering A* **528** (2011), pp. 7317–7322.

[42] P. Zeman et al. "Amorphous Zr-Cu Thin-Film Alloys with Metallic Glass Behavior". In: *Journal of Alloys and Compounds* **696** (2017), pp. 1298–1306.

[43] W.P. Leroy D. Depla. "Magnetron Sputter Deposition as Visualized by Monte Carlo Modeling". In: *Thin Solid Films* 520 (2012), pp. 6337–6354.

[44] A. Păduraru et al. "An Interatomic Potential for Studying CuZr Bulk Metallic Glasses". In: *Advanced Engineering Materials* **9** (2007), pp. 505–508.

[45] Shenoy Vijay. "Atomistic calculations of Elastic Properties of Metallic fcc Crystal Surfaces". In: *Physics Review B* **71** (2005), p. 094104.

[46] Changwen Mi et al. "Atomistic Calculations of Interface Elastic Properties in Noncoherent Metallic Bilayers". In: *Physics Review B* **77** (2008), p. 075425.

[47] Donald R. Askeland, Pradeep P. Fulay, and Wendelin J. Wright. *The Science and Engineering of Materials.* United States of America: CL-Engineering, 2010.

[48] Luc Tartar. *An Introduction to Sobolev Spaces and Interpolation Spaces.* USA: Springer-Verlag Berlin Heidelberg, 2007.

[49] Yvonnet Julien, Le Quang Hung, and Q. He. "An XFEM Level Set Approach to Modelling Surface/Interface Effects and Computing the Size-dependent Effective Properties of Nanocomposites". In: *Computational Mechanics* **42** (2008), pp. 119–131.

[50] Konstantinos Agathos Eleni Chatzi Konstantinos Tatsis. *Method of Finite Elements II.* Lecture notes: ETH Zürich. 2020.

[51] Kim Nam-Ho. *Introduction to Nonlinear Finite Element Analysis.* London: Springer, 2015.

[52] Xiao Chen, Shun Lin, and Jian Ding. "A Three-Dimensional Finite Element Method for Surface Effects". In: *Advanced Materials Research* **97** (2010), pp. 1265–1268.

[53] Xiao Chen, Quan Yang, and Kai Huang. "Characterization of Stiffness Matrix for Surface Effects". In: *Applied Mechanics and Materials* **684** (2014), pp. 53–57.

UNIVERSITÉ CATHOLIQUE DE LOUVAIN
École polytechnique de Louvain
Rue Archimède, 1 bte L6.11.01, 1348 Louvain-la-Neuve, Belgique | **www.uclouvain.be/epl**